Hydrodynamic Performance and Vortex Shedding of a Biologically Inspired Three-Dimensional Flapping Foil

by

Keith K. L. Lim

B.Eng., Naval Architecture and Ocean Engineering
University College, London, 1995

SUBMITTED TO THE DEPARTMENT OF OCEAN ENGINEERING IN PARTIAL FULFILLMENT OF THE REQUIREMENTS FOR THE DEGREE OF

MASTER OF SCIENCE IN NAVAL ARCHITECTURE AND MARINE ENGINEERING
AT THE
MASSACHUSETTS INSTITUTE OF TECHNOLOGY

FEBRUARY 2005

Signature of Author .....
Department of Ocean Engineering
Dec 14, 2004

Certified by .....
Alexandra H. Techet
Assistant Professor of Ocean Engineering
Thesis Supervisor

Accepted by .....
Michael S. Triantafyllou
Professor of Ocean Engineering
Chairman, Departmental Committee on Graduate Students

BARKER

Hydrodynamic Performance and Vortex Shedding of a Biologically Inspired Three-Dimensional Flapping Foil

by

Keith K. L. Lim

Submitted to the Department of Ocean Engineering
on December 14, 2004 in Partial Fulfillment of the
Requirements for the Degree of Master of Science in
Naval Architecture and Marine Engineering

ABSTRACT

The dynamics of flapping remains a subject a great theoretical and practical interest. Propulsion and maneuvering by flapping, optimized through years of evolution, is ubiquitous in nature, yet marine propulsors inspired by examples of highly maneuverable marine life or aquatic birds remain unheard of. The motivation of this research stems from the notion that better propulsive strategies could be obtained from flapping foils; presenting superior alternatives to the conventional propeller for waterborne propulsion. The propulsive properties of a NACA 0012 linearly tapered rigid foil, with a 5.5 cm average chord and 24.6 cm span performing a combined roll and pitch motion are investigated. The mean planform area thrust coefficient and efficiency are recorded over a paramtetric space that included three roll amplitudes, with induced heave (at 0.7 span) to chord ratio, $h_{0.7}/c$ = 1.0, 1.5 and 2.0; Strouhal numbers ranging from 0.2 to 0.6 and maximum angle of attack varying from 15 to 45 degrees. Results show that a maximum planform area thrust coefficient of 2.09 is achieved at $h_{0.7}/c$ = 1.5, St = 0.6 and $\alpha_{max} = 30^0$. The thrust and efficiency data also reveal a useful performance trend where at low α_{max}, high thrust and efficiency can be gained at sufficiently high Strouhal numbers.

DPIV is next used to study the vortical signature created by the flapping foil. Two planes of view, at mid- and 0.8 span were recorded over regimes of low and high thrust. Results show that the vortex patterns are heavily influenced by the foil geometry and kinematics. Three distinct patterns were observed. In particular, the interaction from the shedding of a mixed vortex pair in the wake unveils evidence of strong thrust production. Vorticity control through the replication of this wake vortex pattern can potentially offer optimal solutions for flapping foil propulsion.

Thesis Supervisor : Alexandra H. Techet
Title : Assistant Professor of Ocean Engineering

Acknowledgements

This academic opportunity would not have been possible if not for the financial support by the Republic of Singapore Navy, under the Naval Postgraduate Award, for this I am grateful. First and foremost, I would like to especially thank my advisor, Professor Alexandra H. Techet for her support and guidance throughout, for allowing me flexibility in choosing the research topic of interest, and for accommodating the short timeframe that I had in attempting to complete this research. My heartfelt thanks to Dr Franz Hover for his insights and time taken to discuss the numerous problems and issues that hounded me. I would also like to thank Dr Richard Kimball for bringing me up to speed on propeller theory and for orientating me to the water tunnel facility. My appreciation also to Karl, Steve and Jason for their invaluable advice on experimentation

Special thanks to many others who have made my stay in MIT such a memorable one : Tadd for the warm friendship, I'll never forget thanksgiving dinner at your place; Alex Hornstein, for sharing his tremendous talent in making all things electronic work, immense patience with Galil and directorship in the making of 'Marine Man'; Malima and Chris, for helping out with the fairing design.

Finally I would like to thank the most important person in my life, my wife Jennie for standing by me, taking care of the kids Daniel and Nicole while I dwell in the tunnel, and especially for bringing into this world, the fifth member of the Lim family, little Dominic. Her sacrifice, support and understanding were key to my success at MIT.

I dedicate this effort to my dad, who passed on so suddenly in January this year. It was your wish that I complete this academic pursuit, for this I cross the finish line with loving memories of you close to my heart.

Contents

List of Figures

List of Tables

Chapter 1

Introduction

Nature offers many examples of highly effective and efficient designs. Time has distilled, through millions of years of evolution, a wide diversity of flora and fauna that are well-adept to the environment. The best design guarantees the success and survival of a species. In the quest for better designs in vehicle maneuvering and propulsion, the study on utilization of flapping appendages by birds, fishes and insects lends great insight towards developing superior alternatives to the age-old propeller and rudder design. The fact that these animals can generate significant thrust and maneuverability by employing their wings or fins makes flapping foil propulsion a viable area of research.

Experiments done at MIT have ranged from two-dimensional foil performing heave and pitch motion to tapering three-dimensional foils with oscillatory motions mimicking a simple figure-of-eight pattern observed in some species of fish and marine birds. Of particular interest is the reproduction and investigation of lift-based oscillatory motions produced by sea turtle and penguin fins. Penguins display one of the most remarkable maneuvering capabilities despite its large and rigid bluff-body like physique. Maneuvering forces are largely generated by the flapping of its wings, powering the aquatic bird through water. This impressive display sets the motivation for this thesis to investigate flapping foil actuation, that knowledge gained in this field could lead to a viable mechanical maneuvering system based on flapping fins for water transport. A flapping finned AUV demonstrator built by MIT, as seen in Figure 1-1 serves to show the viability of this proposition.

The focus of the work presented here is to examine the performance of a mechanically-actuated flapping foil in terms of thrust generation and hydrodynamic efficiency. The forces generated by three-dimensional (roll and pitch) flapping and its interactions with the surrounding fluid are studied and presented in the subsequent sections of this thesis.

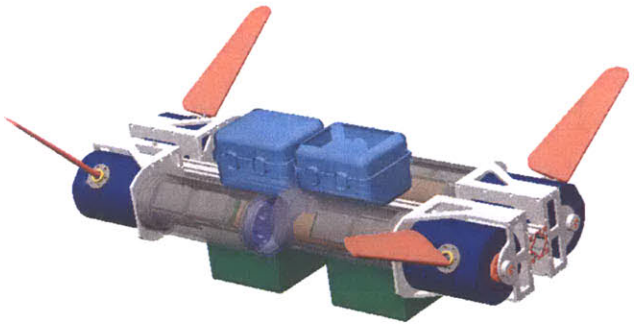

Figure 1-1 : AUV in a sea turtle configuration, Polidoro [20].

1.1 Thesis Objective

The objective of this thesis is to investigate the unsteady forces of a flapping foil in a rolling and pitching motion, as well as to relate its propulsive performance to the vortex structure evolution over the foil and in the near wake. Four main goals are set for this study, to :

- Rebuild and implement a mechanical actuator for three-dimensional flapping in the Marine Hydrodynamics Laboratory (MHL) water tunnel facility.
- Measure the propulsive performance of a linearly-tapered foil based on the NACA 0012 sectional profile.
- Verify the accuracy of the new MC1 multi-axes sensor against other load sensors and with past measurements.
- Measure the wake structure through the use of Digital Particle Imaging Velocimetry (DPIV).

The first goal sets out to reconfigure a flapping foil actuator for the water-tunnel facility. The new actuator would take advantage of the new second generation, two-housing design that features better sealing and compactness to fit the tight space constraints within the tunnel. It will also have sensors for accurate foil positioning and rotational velocity measurements, vital data required for computing efficiency. The dedicated actuator makes possible for different foil configurations to be studied in the tunnel setting, in future.

With the addition of the position sensors for roll and pitch, the tracking of foil position over time can be accurately obtained and mapped against the forces measured. This way, efficiency of the foil at different parameters can be established. The mapping of the foil performance over the range of parameters allow for optimal design points to be identified for flapping foil dynamics.

The implementation of the new six-axes sensor on the foil shaft allows for direct measurements of forces and moments. In conjunction with the position sensors, hydrodynamic efficiencies can now be measured for the first time in the tunnel. The sensor's output can also be verified at the same time by comparing it with the tunnel's main dynamometer.

With DPIV, the wake structure behind a three-dimensional flapping foil can now be recorded. Such visualization would help in understanding how the vortex shedding patterns are related to thrust generation. The wake characteristics, in conjunction with thee force measurements, provides a stepping stone towards transitioning three-dimensional flapping from theory to ocean-going applications.

1.2 Literature Review

The generation of lift or thrust by an oscillating foil lies in the vortex shedding patterns produced within a uniform flow. As observed in aerodynamic flutter, vortex shedding behind a bluff body can cause it to vibrate in a flow [14]. Conversely, a body in motion can impart forces on the fluid due to pressure variations and circulation at the body surface. A flapping foil possesses a varying net angle of attack, caused by the variation in pitch and heave of the foil against the incoming fluid velocity over time. As a result of the Kutta condition, the harmonic motion of the foil causes vortex shedding from the trailing edge. In some instances, the formation of leading-edge vortices is observed. The development of thrust is associated with the formation of a staggered pattern of trailing vortices, producing a reverse Kármán vortex street. Here the average thrust force produced is higher than the average drag and the velocity profile behind the foil is jet-like ([5], [25]).

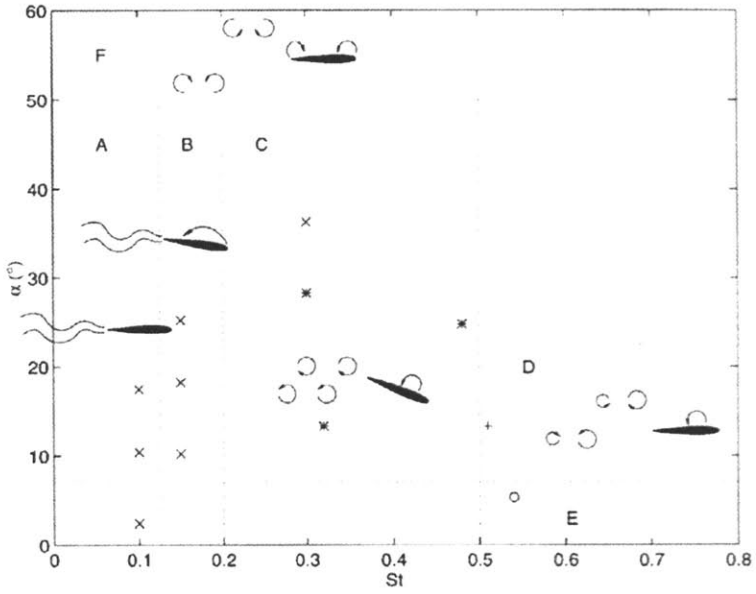

Figure 1-2 : Wake patterns behind a heaving and pitching foil, Anderson [2].

Owing to the high propulsive efficiencies measured on flapping foil experiments ([2], [23], [12]), past investigations were mostly limited to measuring thrust production and efficiencies of both two- and three-dimensional flapping foils . To understand the mechanics of thrust production, some attempts to understand the flow structures behind flapping foils have been made. While flow patterns of two-dimensional flapping foils have been investigated by Anderson [2] and other authors ([14], [5], [6], [11], [17], [18], [19]) the flow structure of three-dimensional flapping foils remains to be successfully analyzed. Some initial attempts were made by Freymuth [6] and Koochesfahani [11], and more recently by von Ellenrieder, Parker & Soria [27] to investigate the complex wake vortex structure.

Observations from most two-dimensional flapping experiments have shown that the structure of the wake and the number of vortices being shed per cycle can thus be substantially modified by the amplitude, frequency and shape of the oscillation waveform ([3], [5]). With larger mean angles of attack, strong leading edge separation tends to weaken the production of the thrust vortex. Frequency of oscillation also affects the vortex wake, where reducing the frequency at high angles of attack results in a reduction of the separation distance between vortices. At a low enough frequency, the drag producing vortex pattern is observed. The asymmetry in the vortex wake also suggests a mean lift as would be expected for any non-zero angle of attacks. The jet-like velocity profile is produced at an angle to the incoming flow, inducing a transverse acceleration of mass and thereby, generating a mean lift force [5].

A staggered vortex street exhibiting a jet-like velocity profile in the wake of the foil was observed by Freymuth [5] where he used a NACA 0015 profile airfoil undergoing separate pitching and heaving modes (at foil-chord Reynolds numbers ranging from 5200 – 12,000). He labeled the vortex street as the 'propulsive vortical signature'. For the case of a pure plunging motion with a mean angle of attack of 5 degrees, flow visualizations showed two strong trailing vortices being shed per cycle. Weak leading edge separation was observed which merged with and reinforced the trailing edge vortices. The 'propulsive signature' was also observed for the pure pitching case with pitch amplitude of 20 degrees and mean angle of attack 5 degrees. Koochesfahani [11] studied the dependency of vortex wake patterns on oscillation frequency. He observed that when all vortices were in line downstream, a zero thrust/drag condition occurred. Any staggering of the vortices would result in a non-zero thrust or drag, the sign being determined by the direction of rotation of the staggered vortices.

Flapping foils have also been closely modeled using theoretical and numerical techniques ([8], [9], [12], [16], [21], [26]). Using computational fluid dynamic analysis, the propulsive performance and vortex shedding of a foil in pitching and plunging motion was investigated by Lu, Yang and Yin [12]. They found that three types of leading-edge vortex shedding had an effective influence on the vortex structures of the oscillating foil wake. For a leading edge vortex development behaving as mode-1 or mode-2 (as shown in Figure 1-4), a reverse Karman vortex street is formed in the wake of the foil due to interaction of the leading edge vortex with the trailing edge shedding vortex. In mode-3, a classic Karman vortex wake is generated.

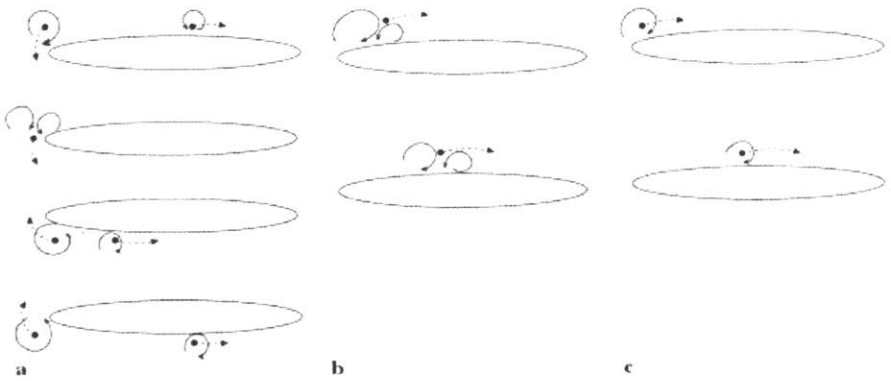

Figure 1-3 : Three different modes of leading edge vortex shedding influencing wake vortex development, Lu X.Y., Yang J.M., & Yin X.Z. : **a** Mode-1; **b** Mode-2; **c** Mode-3. [12].

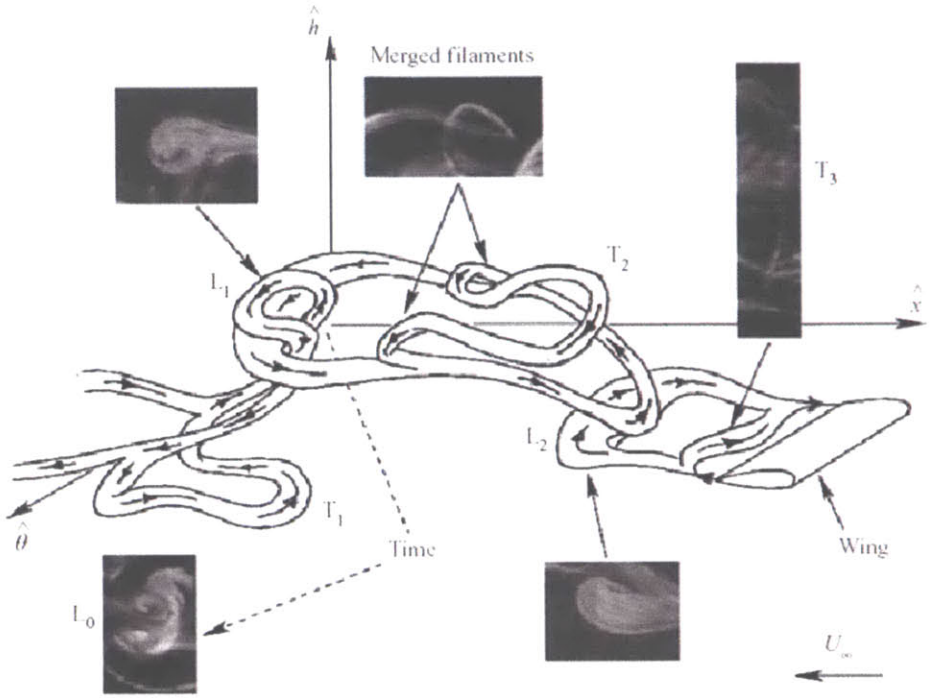

Figure 1-4 : Suggested three-dimensional model of vortex structure behind a heaving and pitching finite-span wing, von Ellenrieder K.D., Parker K., & Soria J. [27].

An attempt to capture the complex three-dimensional structure of the flow behind a heaving and pitching finite-span using dye visualization was pursued by von Ellenrieder, Parker & Soria [27]. The experiments were conducted at a low Reynolds number of 164. The evolution of the flow over one heave/pitch cycle showed vortex structures being shed from both the leading and trailing edges in a distinct pattern. Vortices are shed in an alternating order with trailing edge vortices developing near the extrema of the heaving motion and leading edge vortices forming near the mean heave position. It is postulated that as the vortices convect downstream, the leading edge vortex is stretched, forming a ring-like structure with a bulbous head. Two filamentary arms extend upstream to merge with the successive trailing-edge vortex. These merged filaments drifts toward the mid-span as the cycle continues and wraps around, joining the head of the following leading edge vortex.

Increasing thee pitch amplitude had an effect of causing the filament arms of the leading edge vortices to be less circular in shape. Also, the streamwise spacing of the vortices decreases. It was observed that as the Strouhal number is increased, the spanwise size of the vortex structure also increases, while the streamwise wavelength of the wake decreases. Phase angle variation had the most effect on the timing of the vortex shedding. At a phase angle of 60 deg, the first trailing edge vortex sheds slowly from the wing, allowing the first leading edge vortex to overtake it. In most flow cases, the shedding sequence observed shows first the formation of a trailing edge vortex followed by leading edge vortex. A pair of these occurs over one cycle.

A phase angle of 90 deg between heaving and pitching harmonic motions was observed by Read [22] as most suited for thrust generation. Read performed experiments on a harmonically heaving and pitching NACA 0012 foil with 10 cm chord and 60 cm span where he investigated the aspects of harmonic propulsion, non-harmonic propulsion, harmonic maneuvering and starting maneuvers. The highest propulsive efficiency recorded was 71.5% at 15 deg maximum angle of attack, with a corresponding planform area thrust coefficient of 0.18. Two high planform area thrust coefficients of over 2.4 were achieved at 100 deg phase angle and Strouhal number of 0.60. In his experiments the foil efficiencies reached 50 to 60% in some regions. Read noted that beyond a phase angle of 90 deg, the higher phase angles were more susceptible to corrupted angle of attack profiles.

Non-harmonic propulsion experiments showed that the deteriorating angle of attack profile could be negated by modulating the heave velocity so that a near sinusoidal profile is produced. Read also showed that a non-zero mean pitch bias can result in high mean lift coefficients. Mean lift coefficients of above 4 were achieved. He produced radial vector plots based on the measured thrust and lift coefficients. These vectors were important in that they showed useful 'vectoring capability' of flapping foils that could be potentially applied vehicle maneuvering.

Flores [4] performed similar experiments on a three-dimensional NACA 0015 foil with 5.5 cm average chord and 24.3 cm span on a combined roll and pitch motion where she recorded a maximum planform area thrust coefficient of 2.07 at 40 deg maximum angle of attack and $h_{0.7} / c =$ 1.50. Similar to Read, experiments with a static bias to the foil pitch achieved mean lift coefficients of near 4. Flores also conducted several visualization experiments using Laser Doppler Velocimetry (LDV) and Digital Particle Imaging Velocimetry (DPIV). The wake width measured was found to be equivalent to the excursion of the foil at the 70% span as previously assumed. By measuring the mean flow across the wake, a velocity jet nearly 1.5 times greater than the steady inflow was recorded. This highest velocity in the wake was found to occur behind the foil's mid-span.

McLetchie [15] made further attempts to measure the hydrodynamic efficiency of a three-dimensional flapping foil. A small, six-axis dynamometer was mounted directly onto the foil shaft and the module used two computer controlled servo motors to actuate a foil in a sinusoidal pitch and roll motion, similar to the motion of a penguin's wing. He noted that the measured thrust coefficients compared well to previous experimental results at MIT. The measured efficiency peaked at a maximum of 30 deg angle of attack and at low Strouhal numbers. McLetchie also attempted to establish the center of force for the foil. This was found to be between 47% to 69% of the foil, which is higher than the assumed location at 70% span.

He concluded that the AMTI dynamometer, mounted directly on the foil shaft, was ideal for investigating the performance of three-dimensional flapping foils. Efficiency measurements were reliable in high thrust cases. However, significant errors exist in the measurement in the low thrust regimes. For reliable measurements, the dynamometer had to be mounted as close to the foil as possible to reduce power losses. McLetchie also suggested that the motor efficiency can be improved with the use of rotational springs in the design. Such springs store and return the energy of oscillating motions with very high efficiency. Further optimization of flapping foil actuator design is also possible by adjusting foil geometry, foil rigidity and angle of attack profiles

1.3 Foil Kinematics and Sign Conventions

Two primary rotational motions are prescribed for the flapping foil. Here, the large flapping action is referred to as the roll motion, while twisting of the foil to vary angle of attack is the pitch motion.

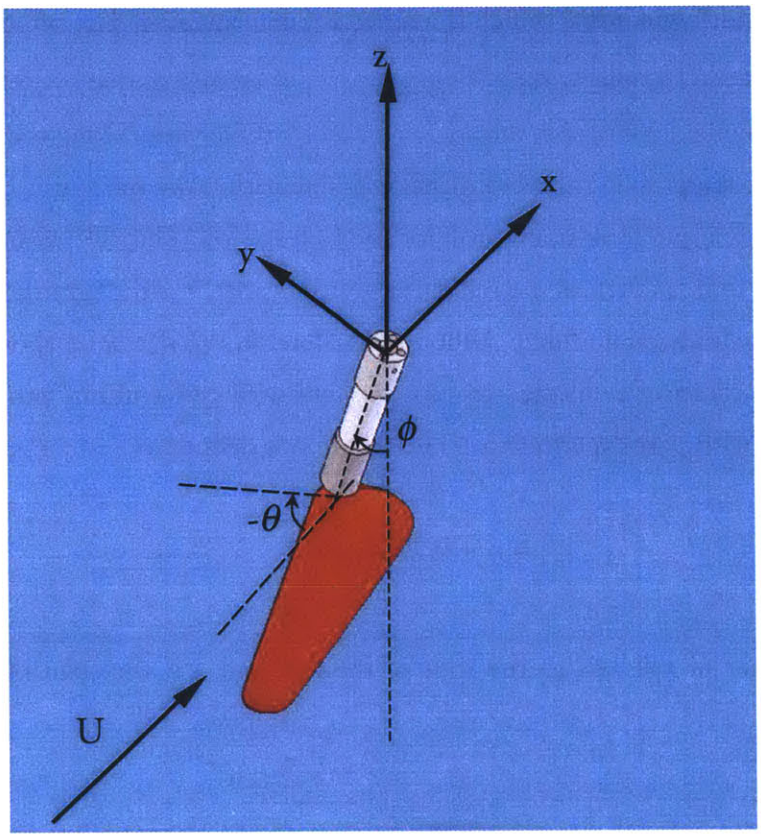

Figure 1-5 : Sign Conventions for a three-dimensional flapping foil in the roll reference frame

1.3.1 Equations of Motions

The experiments were conducted with simple sinusoidal harmonics being applied for both roll and pitch motions. The roll motion of the foil is defined as,

$$\phi(t) = \phi_0 \sin(\omega t) \tag{1.1}$$

where ϕ_0 is the roll amplitude in radians and ω is the frequency of the roll motion in radians per second.

The pitch motion of the foil is then defined as,

$$\theta(t) = \theta_0 \sin(\omega t + \psi) + \theta_{bias} \tag{1.2}$$

where θ_0 is the pitch amplitude in radians and ψ is the phase angle between pitch and roll in radians. θ_{bias} is the static pitch bias which is applied for maneuvering. The pitch bias is normally set to zero, unless specified. The phase angle is set to $\pi / 2$, as recommended by Read [22].

In three-dimensional kinematics, the angle of attack profile varies along the span of the foil as it rolls and pitches. To simplify the three-dimensional kinematics, the motion is decomposed to two-dimensional heaving and pitching at any span location on the foil. The 70% span location (measured from the root of the foil) is taken as the reference position since it is thought that this is close to the effective center of hydrodynamic force. Although McLetchie's [15] results show varying centers of force, the 70% span location is selected to be consistent with conventional propeller notations and for easy comparison with past experiments. This location is defined as,

$$r_{0.7} = r_0 + 0.7s \tag{1.3}$$

where r_0 is the center of roll axis to the root of the foil, and s is the span of the foil, as seen in Figure 1-6.

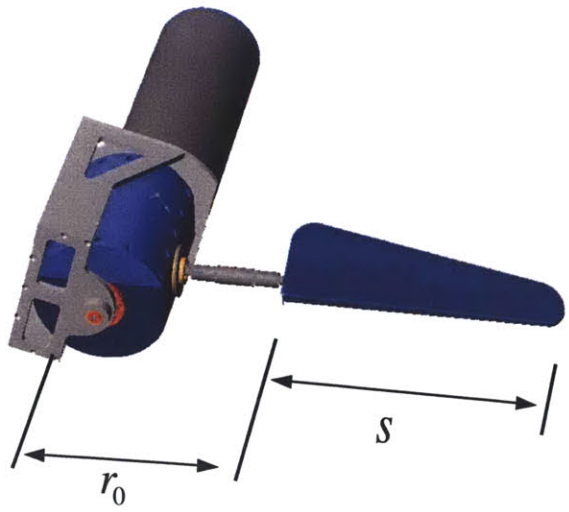

Figure 1-6 : Distance from center of roll axis to root of foil, r_0

The heave position is defined as,

$$h(t) = h_0 \sin(\omega t) \tag{1.4}$$

where h_0 is the amplitude of the heave motion at $r_{0.7}$, and is defined as,

$$h_0 = r_{0.7}\phi_0 \tag{1.5}$$

Hence the angle of attack at one span location can be found from the instantaneous pitch position of the foil and the ratio of the heave to forward velocity. Figure 1-7 shows the vector diagram of the velocity components. A foil with a positive pitch produces a smaller angle of attack and one would need to subtract the angle of attack due to pitch from that due to roll to find the resultant :

$$\alpha(t) = \arctan\left(\frac{\dot{h}(t)}{U}\right) - \theta(t) \tag{1.6}$$

where U is the forward speed of the actuator and $\dot{h}$ is the heave velocity. From equation 1.4, we can express the heave velocity as,

$$\dot{h}(t) = \omega r_{0.7}\phi_0 \cos(\omega t) \tag{1.7}$$

Substituting equation 1.7 into 1.6, we get the expression for angle of attack in three dimensional kinematics.

$$\alpha(t) = \arctan\left(\frac{\omega r_{0.7}\phi_0 \cos(\omega t)}{U}\right) - \theta_0 \cos(\omega t) - \theta_{bias} \tag{1.8}$$

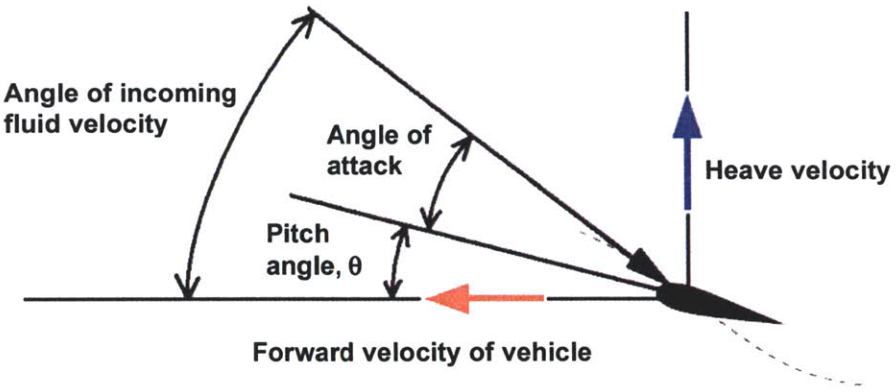

Figure 1-7 : Vector diagram for foil velocity components.

The maximum angle of attack achieved is calculated at $r_{0.7}$:

$$\alpha_{\max} = \max\left[\alpha(t)\right] \tag{1.9}$$

The application of positive pitch θ_0 to produce thrust and lift is summarized by Polidoro [20] as follows :

> Note that for positive θ_0 the pitch motion is selected to reduce the maximum angle of attack, which is the case for vast majority of the motions that produce thrust. In these cases the leading edge of the foil is rotated towards the direction of incoming flow. θ_{bias} is used to make the mean angle of attack nonzero, and therefore the mean lift force nonzero [9]. Nonzero lift forces allow for the thrust vector to be rotated out of the surge direction in order to produce maneuvering forces on the vehicle.

Fig 1-8 shows the solution for the angle of attack profile for different spanwise locations. In cases where the roll induced component is large enough, a smooth sinusoidal angle of attack profile is still retained after the pitch component, θ, is subtracted from it. To produce a lower $\alpha_{\max}$, θ is increased. When θ becomes large enough, the profile gets distorted and an inflection point occurs. The local angle of attack at the root of the foil is thus negative.

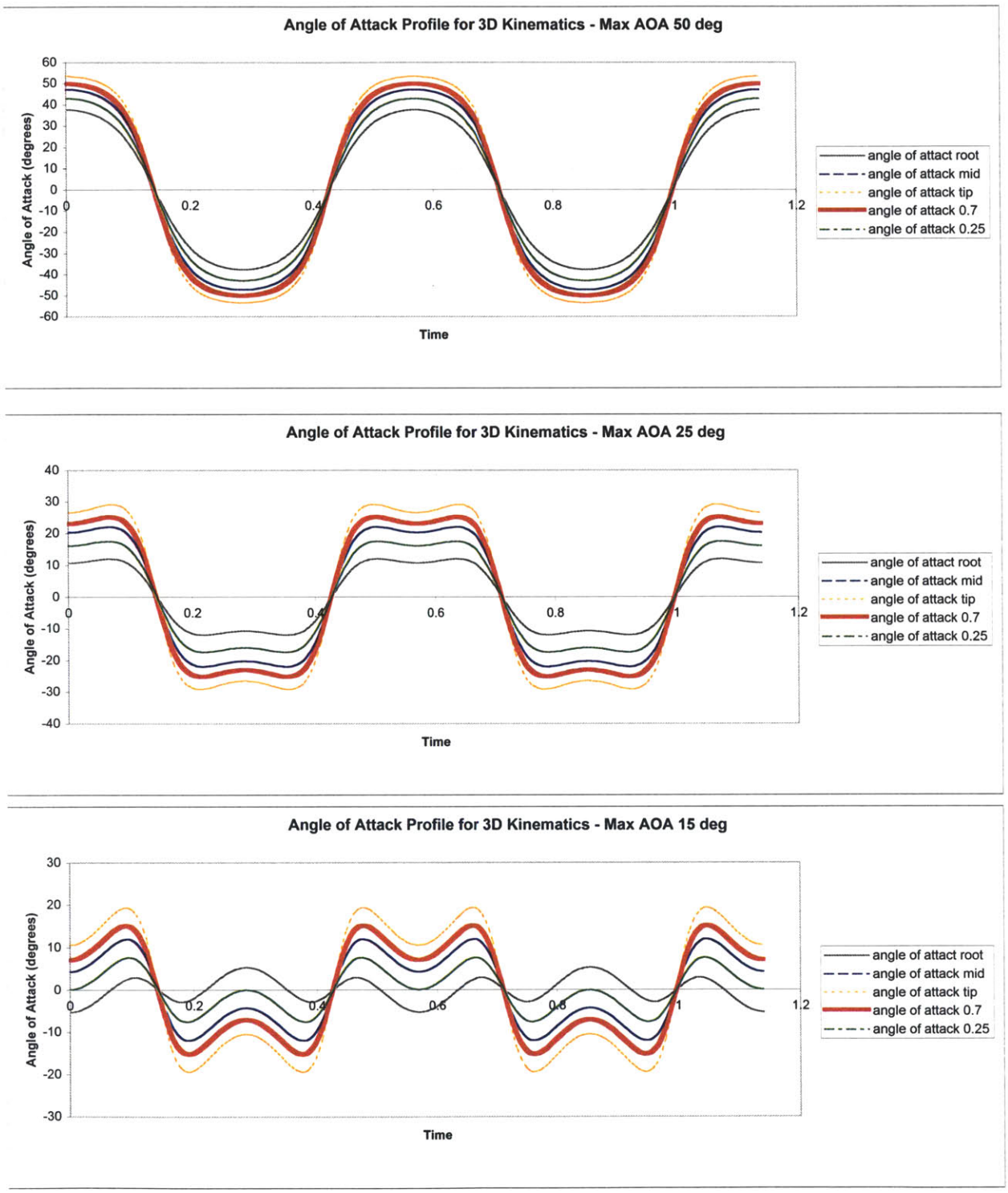

Figure 1-8 : Angle of attack distribution over span. Pitch amplitude is varied to provide a range of α_{max} . Lower values correspond to larger pitch amplitudes. At lower α_{max} values, an inflexion point starts to form. Beyond this, larger pitch motion will lead to a negative local angle of attack at the root, degrading thrust production.

1.4 Dimensionless Parameters

To generalize the results from the experiments, non-dimensional parameters are required. The same conventions are retained to non-dimensionalize important parameters for comparison with past experiments.

A key parameter is the Strouhal number, St, which is used to normalize the roll velocity. Using the same conventions assigned by Triantafyllou [25], the Strouhal number is taken as

$$St = \frac{2h_{0.7}f}{U} = \frac{2r_{0.7}\phi_0 f}{U} \tag{1.10}$$

where the heave velocity is taken at 0.7 span. $2h_{0.7}$ is taken as the estimate of the wake width produced by the flapping foil.

For the three-dimensional case, the roll amplitude is non-dimensionalized by converting this to two-dimensional heave amplitude at 0.7 span and dividing by the chord length,

$$\frac{h_{0.7}}{c} \tag{1.11}$$

The third parameter used is the maximum angle of attack, in radians, which is itself, a dimensionless parameter.

$$\alpha_{max} \tag{1.12}$$

1.5 Document Roadmap

This thesis is organized as follows. Chapter Two will provide a summary of previous research and designs of flapping foil actuators at MIT. The merits and limitations of each generation of actuators are discussed. Finally, the modifications applied to a double housing actuator for use in the MIT MHL water tunnel are presented.

Chapter Three covers in detail the experimental setup and techniques. The calibration and sensitivity of all sensors are also presented. In particular, the setup and the calibration of the AMTI MC1 six-axes sensor is discussed. Here, the treatment of channel cross-talk and derivation of the 6×6 sensitivity matrix is stepped through. Motion control and fine-tuning of the actuator is also discussed. With eleven signals being acquired, some signal conditioning measures were necessary. The approach taken towards eliminating signal noise is thus cover briefly in this chapter. It will then proceed to show the rotation matrices and offsets required to transform forces measured to the appropriate reference frames.

The results from the force and efficiency measurements are presented in Chapter Four. Comparisons with past results are made and discussed. The chapter will also show the repeatability of the results through an error analysis.

Chapter Five shows the vortex shedding patterns recorded during the three-dimensional flapping at various flow parameters. Velocity vector and vorticity plots are presented, where comparisons are made with past flow visualization experiments.

Finally, Chapter Six will summarize the findings from this thesis and will suggest improvements and potential areas for future research.

Chapter 2

Flapping Foil Actuator Design

2.1 Previous Work

A comprehensive review of previous work on robotic fish and flapping foil designs has been chronicled by Polidoro in his thesis [20]. He also pioneered the design of a double-housing design for flapping foil propulsion that introduced marked improvements to the experimental capabilities of the foil actuator in terms of modularity and water-tight integrity control. This double-housing design was also a key component of the AUV he constructed for the purpose of research in hydrodynamics and motion control, as seen in Fig 1-2.

2.1.1 Single Housing Design

Early flapping propulsion experiments consisted of two-dimensional foils mounted on vertical struts at each end of the foil and motion was provided by chain drive system. To study the effects of three-dimensional foils, it was necessary to design actuators capable of producing harmonic motions of foils in a uniform flow.

Two generations of foil actuator designs exist. In the first generation design, all components and circuitry were located in a single water-tight housing, as seen in Figure 2-1. Such an actuator was used by Flores [4] in her foil experiments.

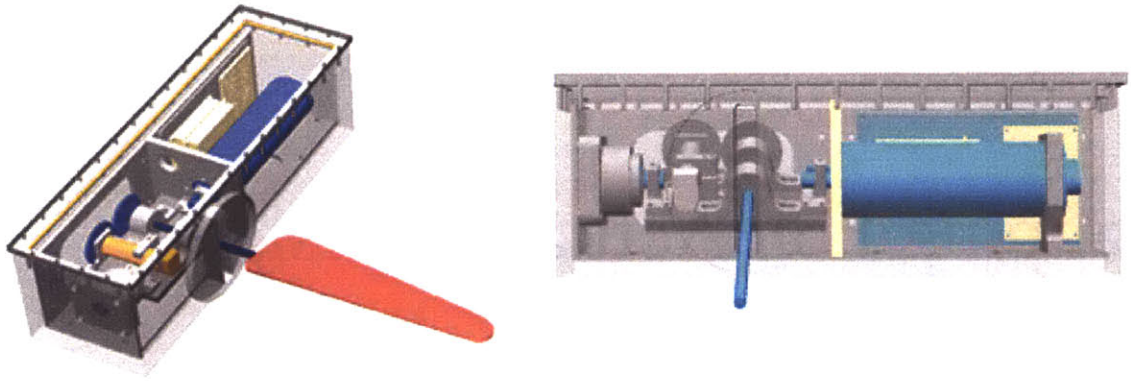

Fig 2-1 : Single housing foil actuator for tow tank and water tunnel applications [4].

A single housing design simplifies all wiring and mechanical actuation but presents complex sealing problems. The dynamic seal is provided by a flexible cone shaped bellow, as seen in Figure 2-2. The bellow-seal used in such a design limited the depth of operation, range of motion and was subject to fatigue. The external housing is made of Lexan, with an Aluminum sub-frame. The roll motor is face mounted to a bulkhead which separates the pitch actuator from the larger compartment containing the roll motor, motion control cards and PWM amplifiers. Pitch actuation is achieved by a small DC brush motor with gear reduction. It rests on a swiveling plate with pillow blocks attached. The plate is supported by the roll motor shaft on one end and double roller taper bearings on the other end. Waterproof cables and connectors provide power and communication to the module. While the pitch axis has a full 360 degree range of motion, the range on the roll axis is limited to 26 degrees due to the stiffness of the bellow.

Fig 2-2 : Cone shaped bellow seal, Polidoro [20]. The seal is made of flexible urethane with Shore A hardness of 30 and Kevlar composite. It contains a shaft seal with two buna-n o-rings and Teflon bushings. An inner retaining ring bolts to the Lexan housing while a smaller outer retaining ring compresses the bellow on the outer surface to form a face seal. The useful life of this design was measured to be about 60,000 cycles, before fatigue sets in.

2.1.2 Double-housing Design

The second generation flapping foil actuator consists mainly of two watertight pitch and roll canisters housing just the motors and chain drive. All electronic parts are migrated to outside of the flow so as to reduce the risk of damage from water shortage. The pitch canister attaches to and pivots about the shaft of the roll canister. The pitch canister is fashioned from black delrin and the roll canister is made out of standard PVC piping with Aluminum end caps. Dynamic rotary seals made out of Polyurethane, LEXAN and buna o-rings prevent water ingression through the shaft bore. Since these seals are only subject to small motions in contact with a rotating shaft, they have better fatigue life as compared to the bellow seal.

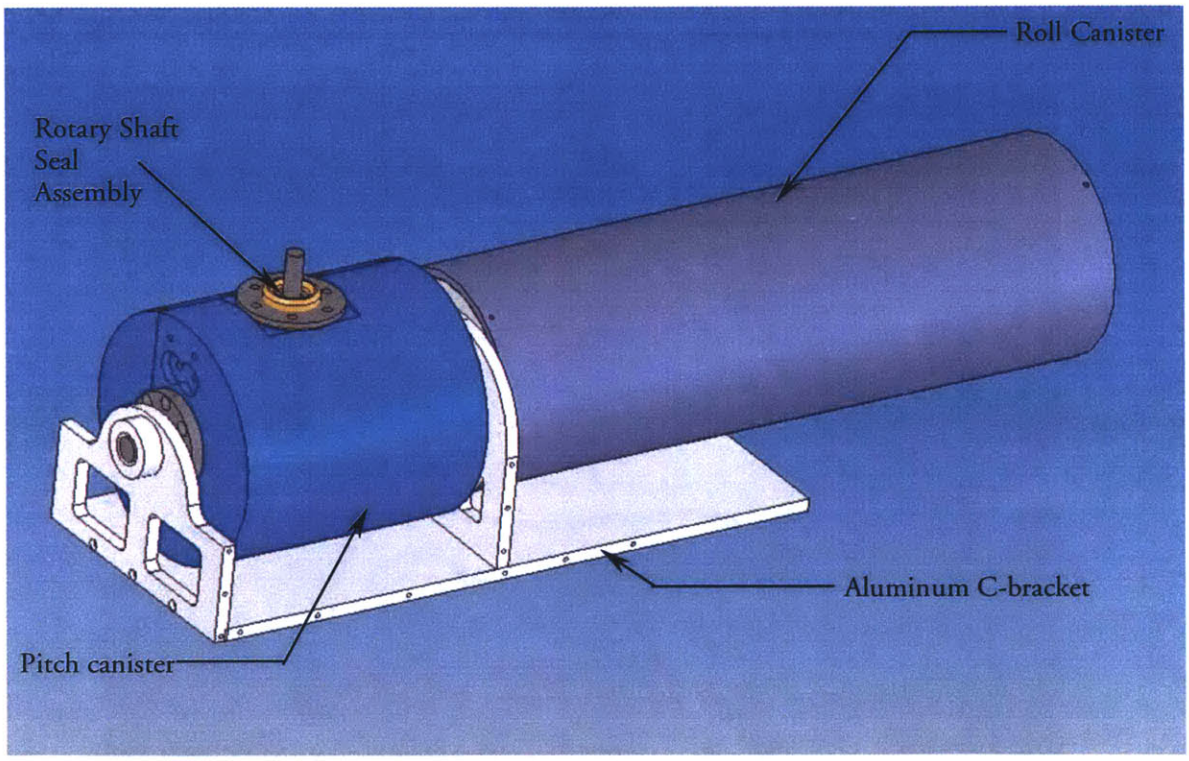

Fig 2-3 : Solidworks drawing of a double-housing foil actuator design

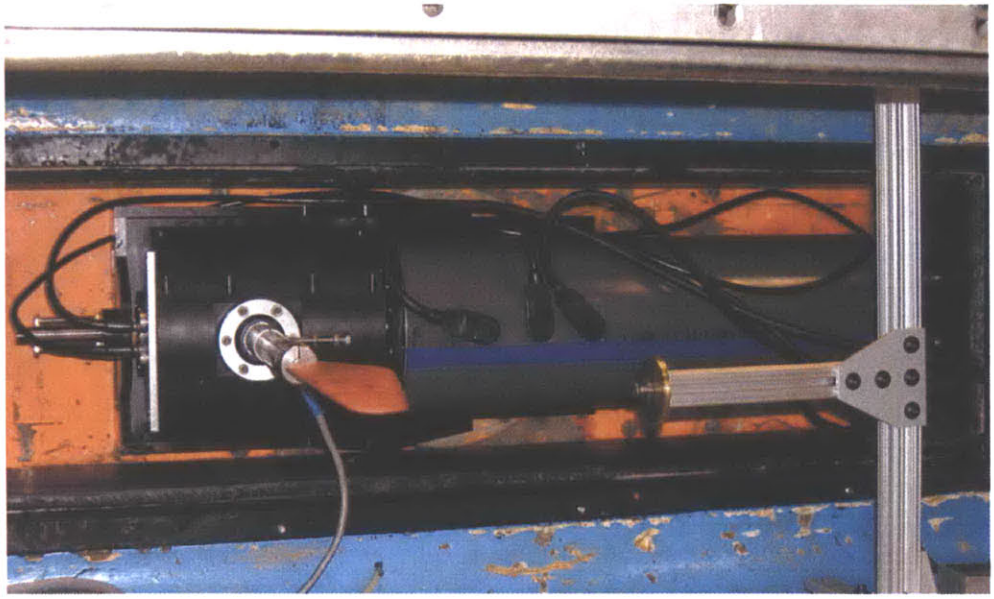

Fig 2-4 : Double-housing flapping actuator mounted sideways in the MIT water-tunnel test facility

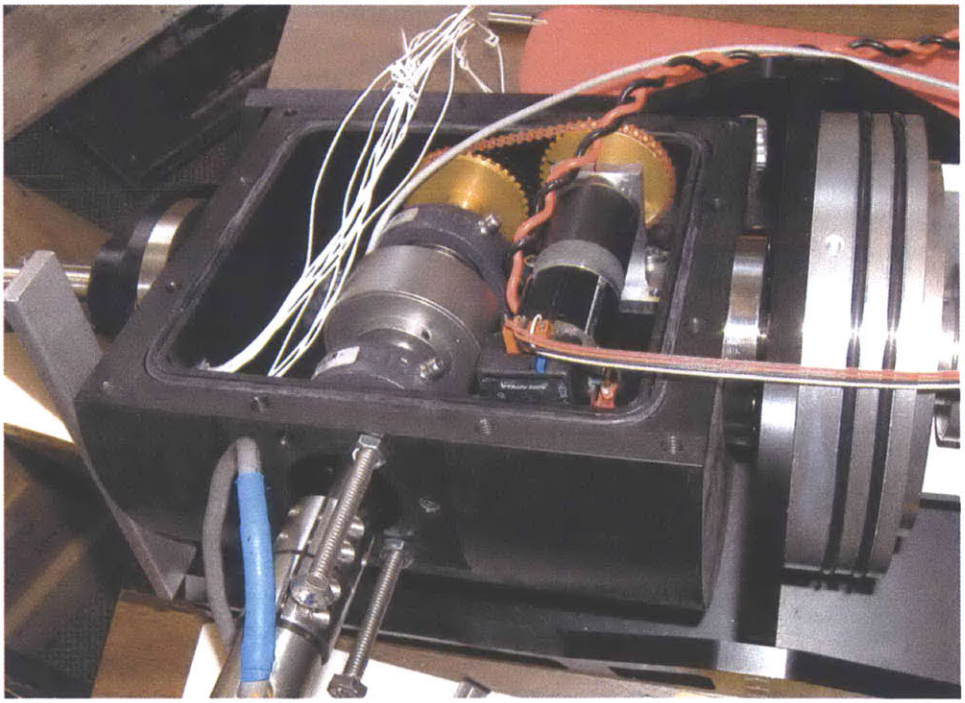

Fig 2-5 : Internal assembly of pitch canister. A block of Delrin is carved out to house the pitch motor and shaft, resting on two pillow blocks. A HEDM 5500 B13 two-channel optical encoder attaches to the end portion of the motor, while on the other end, a sprocket and chain assembly links the motor to the pitch shaft. Impulse IE55 waterproof connectors are used for signal communication. The housing is supported on one end by the roll motor shaft and by an anodized Aluminum C bracket on the other. A Rulon wet bearing is used to allow smooth rotation about the bracket.

2.2 Modifications

2.2.1 Torque and Position Measurements

To improve force measurements and efficiency calculations, some modifications to the double-housing actuator were effected. Two Inscale GL200 hollow-shaft potentiometers were added, one to each of the rotating shafts for position mapping. While the motor encoders provide some indication of pitch and roll angles, these are not reliable indications of the shaft angles over time since some backlash in the chain drive or gearhead will cause the shaft rotations to lag that of the motors. Potentiometers mounted directly on the pitch and roll shafts provide accurate feedback on the actual rotations.

In addition, an ENTRAN ELT-2 reactive torque sensor was added to the roll motor shaft to measure the power input from the motor end during actuation. This sensor has a torque capacity of 15 Nm and utilizes semi-conductor sensing elements to provide full scale outputs for torque.

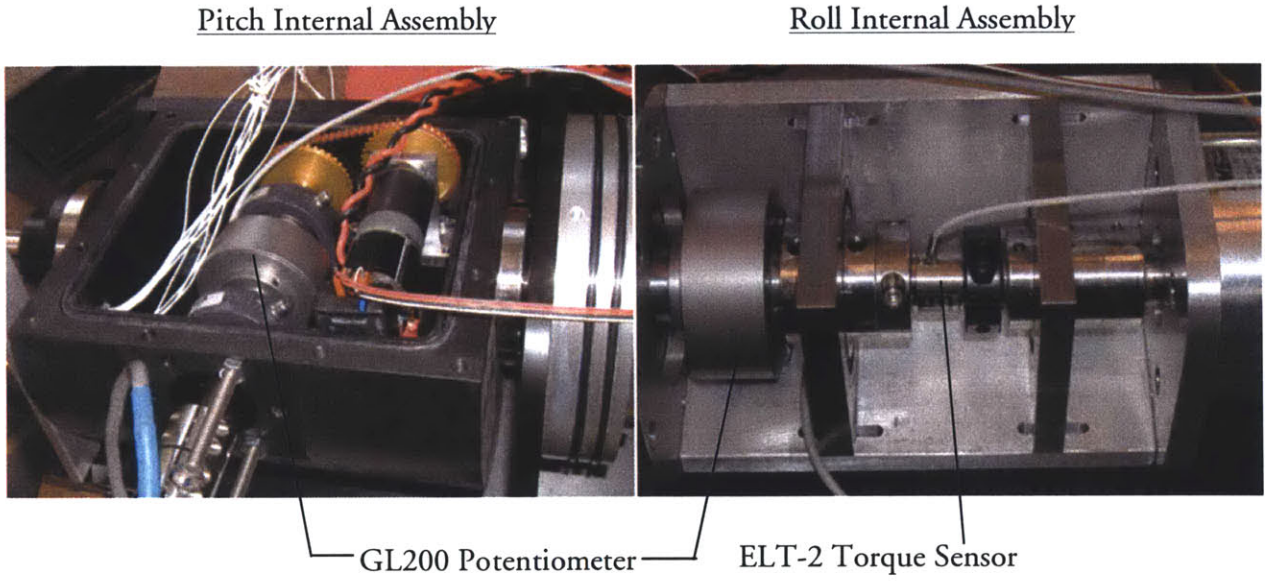

Fig 2-6 : Retrofit of potentiometers and torque sensor. The potentiometers are mounted directly to the shafts using specially-made sleeves to accommodate the metric dimensions of the bores. The housing is made of anodized Aluminum and features slotted ball bearings. In the roll assembly, a torque sensor is mounted between the shaft coupling and the roll motor. On the motor end, the shaft coupling has a keyway to match the gearhead and a square hollow on the other end to accommodate the square sockets of the torque sensor. A similar shaft coupling connects the sensor to the roll shaft. Aluminum plates with press-fitted bearings provide radial support to the shaft.

2.2.2 Shaft Seal

While the original polyurethane shaft seal assembly was effective in preventing water ingression, its fabrication was tedious. Liquid polyurethane is first poured into a mold and set to produce the seal boot. A Lexan insert is then machined and bonded to the bore of the seal boot. Buna-N o-rings are then placed inside the Lexan piece to complete the shaft seal.

To simplify its production, the flexible seal boot is now replaxed by a single-piece construction Lexan plug as shown in fig 2-7, with machined grooves to fit o-rings on the outer diameter and internal bore. Larger o-rings of 0.375in thickness were used externally (as the face seal) to accommodate some roll shaft flexure. EPDM (Ethylene Propylene) o-rings were chosen for its resistance to water and liquids.

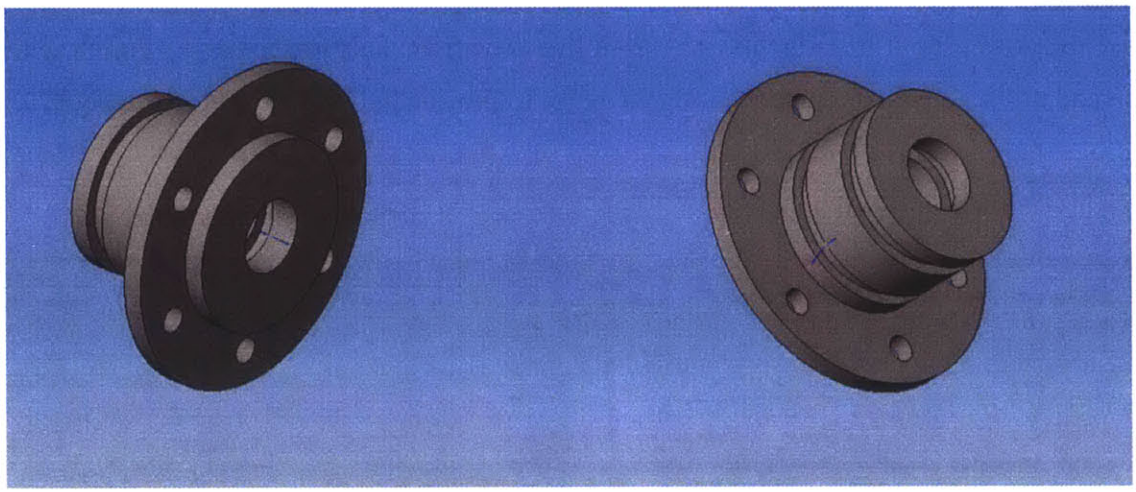

Figure 2-7 : Solidworks drawing of a single-piece construction Lexan shaft seal boot.

With the original flexible-type seal being readily available for the pitch shaft, this rigid-type prototype was applied only for the roll shaft seal. The solid construction was found to aid in aligning the shaft with the intended axis of rotation. It also provides radial support to the shaft, thereby limiting the unsupported length of the shaft subject to bending loads and flexure. In contrast, the flexible nature of the pitch seal boot assembly presented some problems. During assembly, shaft alignment with the rotational axis proved difficult since the seal boot accommodates any misalignment. Such misalignment is evident from the 'grabbing' of the seal on the shaft when the shaft changes rotational direction, resulting in a slight distortion of the pitch motion. This effect is discussed in further detail in Section 3.6. While proper lubrication alleviates this, the 'grabbing' returns after some time as the o-ring starts to wear from the repeated rotations.

2.2.3 Spring Mount

To overcome the large inertial forces faced by the roll motor in rotating the pitch canister, the foil assembly now includes an extended shaft on the end of the pitch canister for possible mounting of rotational springs. Suitable springs with natural frequencies matching the rotational frequency of the actuator can be installed to reduce the torque requirements from the roll motor. Further study of its dynamics and rotational spring design are necessary for a successful implementation of this modification. While this modification was not applied during this series of experiment runs, this project serves to introduce one possible spring assembly prototype.

This basic design has springs with equal spring constants being constrained on one end by the C-bracket and on the other by a bar attached to the pitch canister. The springs are pre-compressed to set up a neutral position at zero roll angle. It should be noted that most commercially-available springs are not linear and hence customised springs may need to be made for this application.

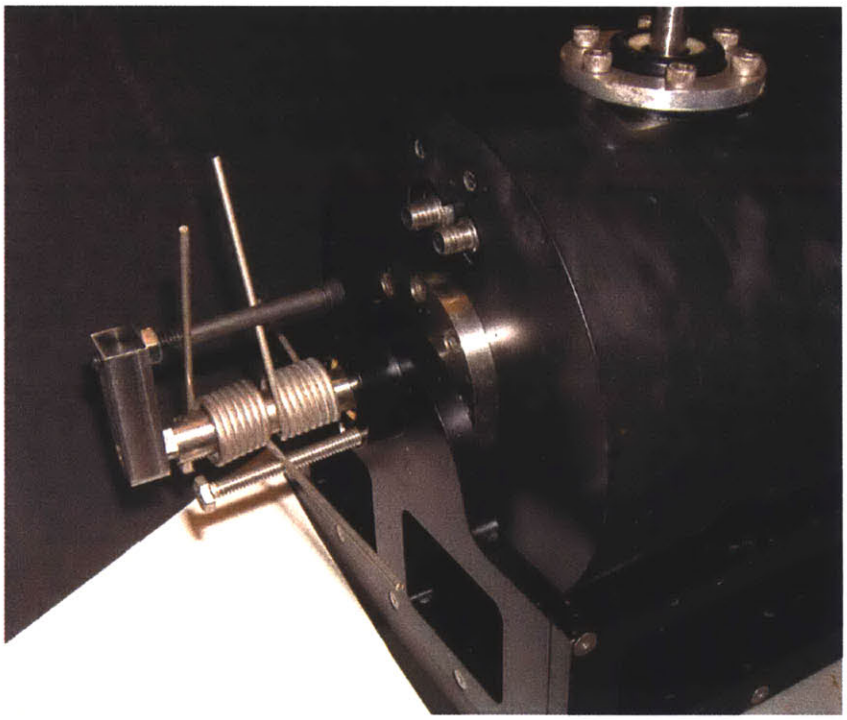

Figure 2-8 : Spring-mount assembly on pitch canister

Chapter 3

Experimental Setup and Methods

3.1 General Description

In this project, there were two sets of experiments. The first set basically comprised of force and efficiency measurements taken from the double-housing flapping foil actuator in a flow stream. The second entailed capturing the flow field generated by the actuator using Digital Particle Imaging Velocimetry (DPIV). The water tunnel in the MIT Department of Ocean Engineering Marine Hydrodynamics Laboratory (MHL) was used for both sets of experiments. Here, flow in the tunnel was controlled by a variable speed impeller and measured using Laser Doppler Velocimetry (LDV). Motion control of the actuator was achieved by a Galil two-axes PID motion control card connected to a PC system. The motion comprised of simultaneous roll and pitching at 90-deg phase lag.

Force measurements were primarily made using an AMTI six-axes sensor attached between the foil and pitch shaft. For comparison, a second dynamometer mounted on top of the water tunnel measuring drag and lift in the tunnel reference frame was also employed. A National Instruments PXI system was used for data acquisition, capturing both force and position signals. A separate PC system was also used to operate DPIV and acquisition of image pairs using a proprietary software.

3.1.1 MHL Water Tunnel Assembly

The MHL water tunnel facility is essentially a two-storey structure, with the test section and storage tank on the first level and a large DC generator and motor on the lower level to drive the tunnel impeller. The impeller speed is set using dials on a control panel at the first level, which vary the field current on the impeller. The tunnel test section has a square section of 0.5 m and is 1.5 m long. The free stream turbulence intensity in the tunnel is rated at 1%.

Surrounding the test section are four removable windows that allow flexibility in the setup of test equipment. In this project, the foil actuator was mounted on the top portion of the tunnel. A three-piece Aluminum housing encloses the actuator, on top of which, sits the tunnel dynamometer. The actuator is isolated from the tunnel wall and housing and only connects to the dynamometer directly for force measurements. A brass collar on the dynamometer clamps a flanged shaft that is attached to the C-bracket of the actuator. The foil extends downwards to the test section and has a separation distance of 0.5 span from the tip of the foil to the bottom window of the tunnel. Figure 3-1 shows the completed assembly installed in the tunnel.

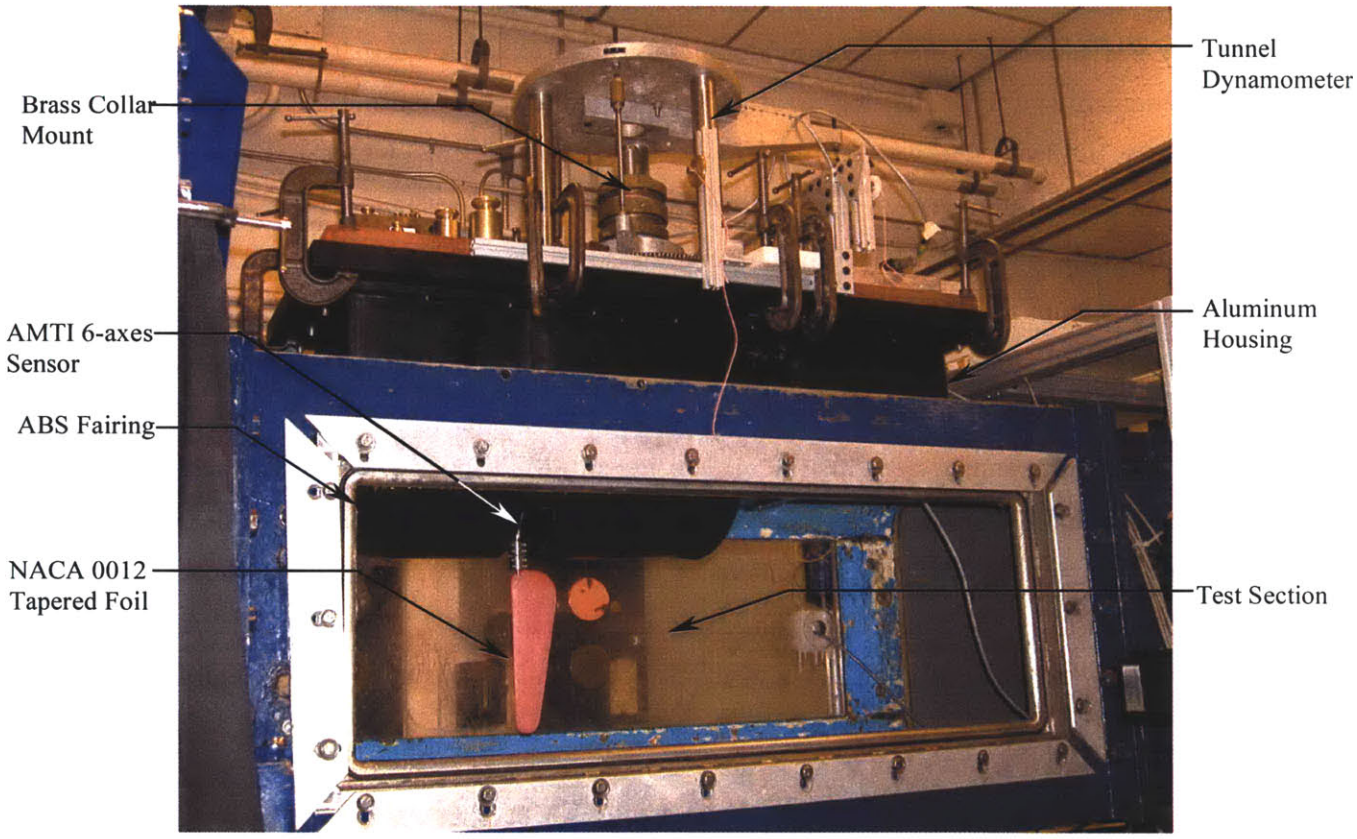

Figure 3-1 : MHL water tunnel facility. The foil actuator is housed within an anodized Aluminum housing on top of which, sits the tunnel dynamometer. The actuator is held in place by a shaft from the C-bracket to the collar of the dynamometer. When assembled, there is a separation distance of about 1cm between the bracket and the dynamometer window. C-clamps are then used to attach the dynamometer window to the housing.

A special fairing was constructed to minimize any disturbance caused by the actuator motion within the housing with that of the free stream over the foil. As part of the pitch canister and six-axes sensor protruded into the test section, this fairing was necessary to provide at best, an undisturbed free stream over the foil span. This fairing is made from a 1/8 in thick ABS plastic sheet shaped by a thermoforming process to produce a half-cylindrical shell with a domed end. A 1.5 in wide clearance slot was then machined cut to allow unconstrained roll motion. The corners of the slots were also rounded to reduce the stress concentrations and minimize fatigue failure at those points.

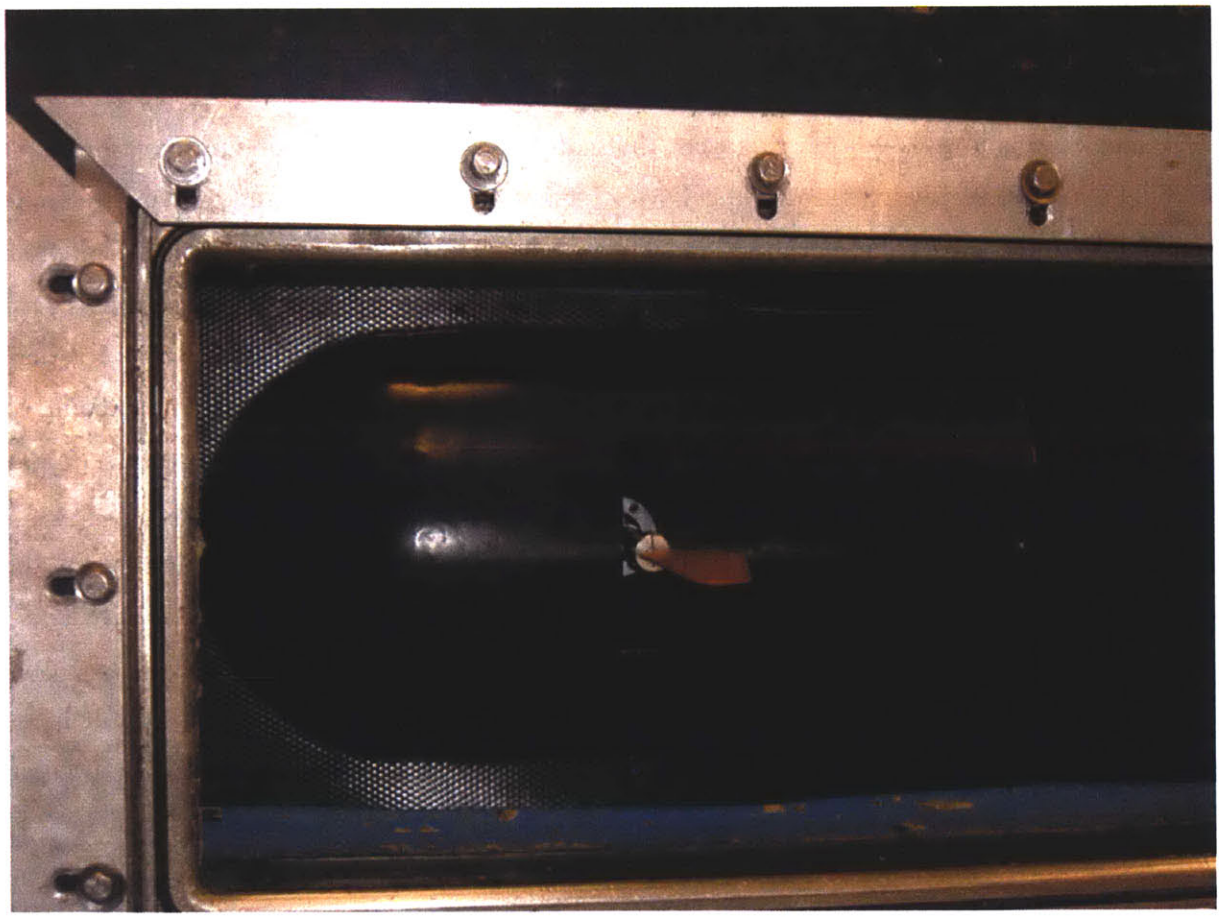

Figure 3-2 : Thermoformed ABS plastic fairing. The fairing was made using the thermo-vacuum forming machine in Pappalardo Laboratories, Department of Mechanical Engineering. Black ABS was chosen to reduce any possible laser reflection from PIV or DPIV operation. Countersink capscrews mount the flange of the fairing directly to the Aluminum housing. Support bars underneath the flange were added for rigidity and hence introduced a gap of about 0.5 in between the flange and the tunnel wall. The original wooden fairing used by Flores in her experiment was cut down and re-used as the mold for this application.

3.1.2 Actuator Electronics and Signal Communication

The motion control electronics of the flapping foil actuator comprises of a Galil dual-axes motion controller, DMC-1425 that uses PID compensation for velocity and acceleration feedforward. It communicates with the pitch and roll servo-motors through dedicated PWM servo-amplifier modules. These amplifiers controlled the current to the motors and hence its speed and direction. A standalone PC connects to the DMC-1425 through Ethernet where a proprietary Windows program, DMC Smart Terminal provides a simple editor for programming and downloading to the controller. It also acts as a communication terminal for sending two-letter commands to the controller for direct execution. The entire module is housed outside the tunnel to eliminate the risk of water shortage. The module runs on a 24V DC supply, with a DC-DC converter being used to channel power to the servo-amplifiers and motors.

A simple program was written to govern the motion of the actuator. For sinusoidal motion in the roll (X-axes) and pitch (Y-axes), the DMC-1425 vector mode was employed using circular interpolation and eclipse scaling of the X and Y axes. For a 90-deg phase lag between the pitch and roll, the program was executed at maximum roll amplitude (at which, the pitch amplitude is zero). Both the pitch and roll motors had optical encoders with different resolutions, hence each had a different encoder count per degree. The eclipse scaling was thus necessary to take into account the different encoder counts/degree ratio and also different pitch and roll amplitudes. The program takes roll and pitch amplitudes, flapping frequency, encoder error limits and number of cycles as input and determines vector speed based on amplitude and flapping frequency. It then simultaneously calculates the vector motion in the X and Y plane. It does this by specifying a 2-dimensional arc segment for each axes, with radius equaling the respective pitch or roll amplitude. The traverse is over a full 360 degrees, prescribing a continuous circular path. The result is a 3-dimensional motion since a circular path is etched out in each plane simultaneously. The precision of the coordinated motion is further discussed in section 3.6.

Waterproof cables and connectors from Impulse Enterprise transmitting power and communication signals serve to link the external electronics module and data acquisition system with the submerged actuator. Low profile multi-channel bulkheads are mounted on both the actuator and aluminum housing, with wet-pluggable neoprene cables serving as the interconnect within the tunnel test section. These cables were tied carefully within the housing to prevent them from interfering with the foil motion. Here, power lines were kept separate from the rest, which consisted of encoder signals and signals from the torque and position sensors.

3.1.3 Data Acquisition

Acquisition of force and position data was made through the National Instruments PC-based PXI system with a software control panel interface configured using Labview 7.0 graphical programming language. The hardware consist of a PXI -1011 chassis fitted with a 6031E data acquisition board for continuous high speed data logging. A shielded connector block with 24 signal-labeled BNC connectors feeds signals directly from the sources to the acquisition block. Toggle switches on the BNC inputs were set to either floating-signal source for the battery-powered potentiometers and torque sensors or ground-referenced source for force signals coming from the 6-axes sensor and tunnel dynamometer. The sampling rate was set at 500 Hz for all runs and data was saved into a text file for MATLAB post-processing.

3.1.4 Laser Doppler Velocimetry

The LDV system was used to measure the mean flow velocity in the tunnel. This consists of a Lexel model 95 Ion Laser that projects a fringe pattern upstream of the foil to detect particles in the flow. The signal is then fed to a Dantec FVA Enhanced signal conditioner and processed using the proprietary FVA flow software.

3.1.5 Digital Particle Imaging Velocimetry

The X-Y plane of the wake is captured in this setup at 2 different foil locations, at both 0.6 and 0.9 span. A New Wave Research Tempest ND:Yag laser illuminates the plane and image pairs are captured real-time by a Megaplus ES 4.0 2k X 2k CCD camera (from Redlake MASD Inc) through pulse triggering. A TTL input is sent to the LaVision Flow Master 2S 3D computer system by the Galil DMC 1425 controller card each time the foil rolls to maximum amplitude. A phase delay is then set in the LaVision software to capture the images at various stages of the flapping. A total of 15 image pairs are used for phase averaging over 6 different angles in the roll cycle. Details of the DPIV implementation and operation are discussed further in Chapter 5.

3.1.6 Foil Description

The foil used in this experiment is the same foil that McLetchie used in his tests. It features a NACA 0012 cross section, with a span of 24.6 cm and 5.5 cm average chord length. The foil has a linearly tapering trailing edge profile as shown in Figure 3-3. This foil was cast from a mold using low viscosity urethane forming a rigid wing structure. A stainless steel triangular frame was inserted to the foil for added rigidity. The skeletal frame terminates with a 3/8 in diameter rod extending from the root to allow connection to the shaft coupling.

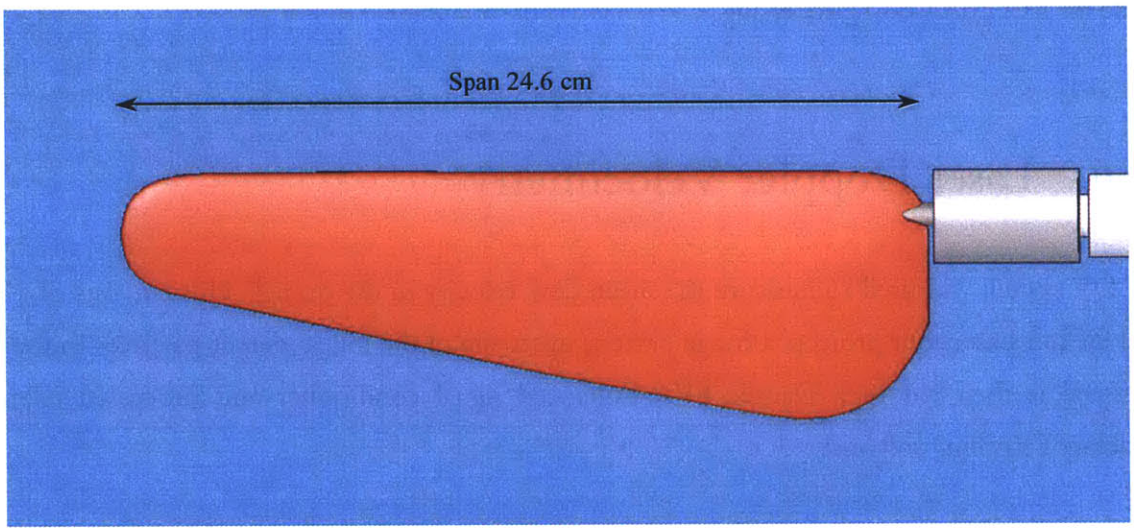

Figure 3-3 : Solidworks drawing of the NACA 0012 linearly tapered foil

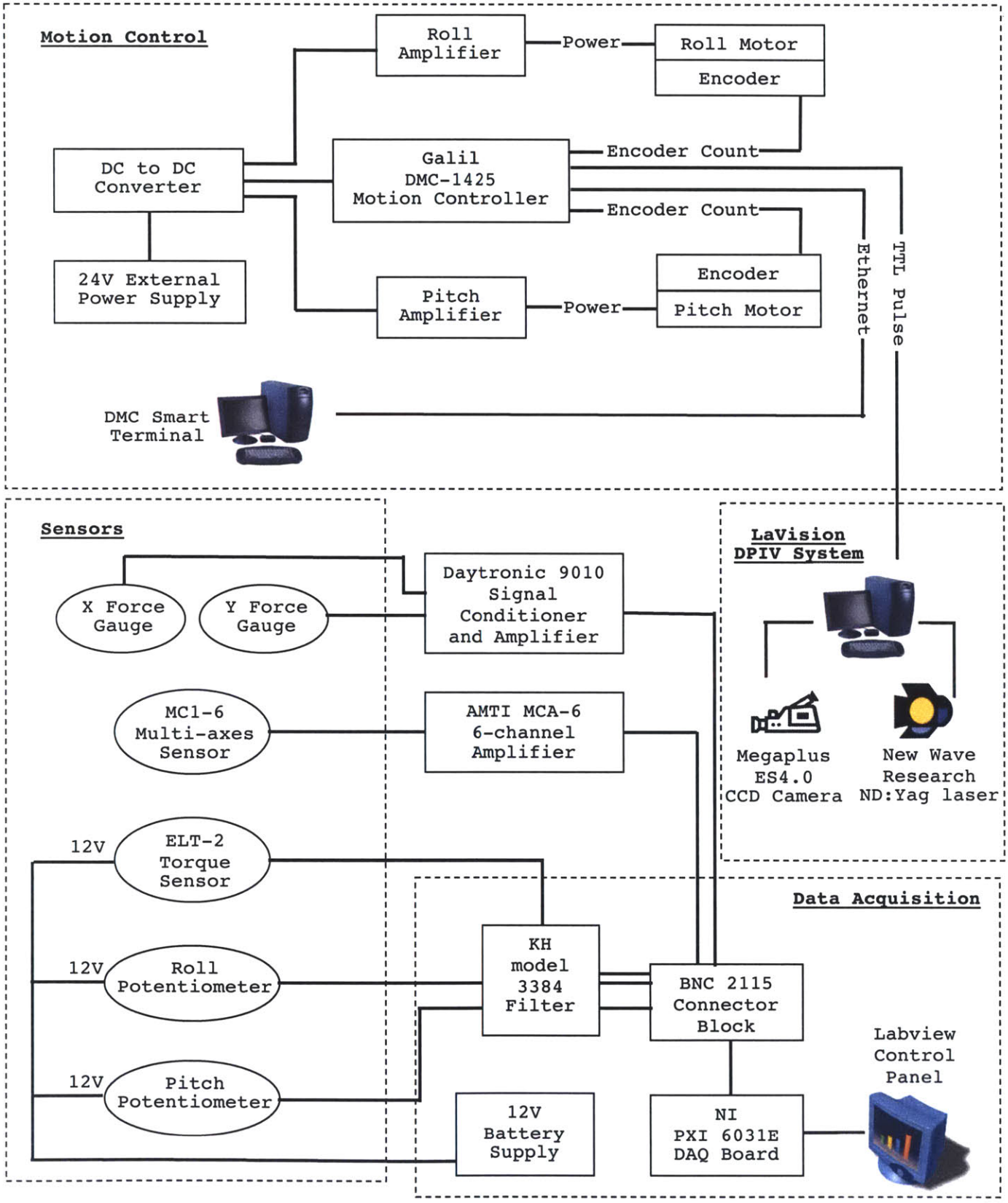

Figure 3-4 : Motion control and data acquisition schematic

3.2 Potentiometers

Roll and pitch positions are measured using GL200 hollow shaft potentiometers from Inscale Technology. The Inscale potentiometer has an electrical angles of 340^0 and torque of less than 6.0 Ncm. The linearity is rated at $\pm$ 0.25% and has a nominal resistance of 20 kΩ. An input voltage of 12V was supplied to the potentiometer in series with a 2 kΩ resistor. The voltage drop across the resistor was then measured as the signal. This arrangement was necessary as the data acquisition board records voltage differential across analog sources instead of variations in current flow.

To calibrate the potentiometer, a digital protractor was used to measure the displaced angle of rotation from the shaft. The protractor had an accuracy of $\pm 0.1^0$. Voltage readings from a range of positive and negative angles were recorded and plotted. According to Kirchoff's Law for a constant current, the voltage across the resistor is inversely proportional to the sum of the potentiometer resistance and series resistance. If V_{input} is the supply voltage, R_{pot} is the potentiometer resistance and R_{series} is the resistance in series, then

$$V_{input} = I(R_{pot} + R_{series}) \tag{3-1}$$

$$\Rightarrow \quad V_{resistor} = \frac{V_{input} \cdot R_{series}}{(R_{pot} + R_{series})} \tag{3-2}$$

A hyperbolic curve fit of the form was found from the plot. The curve fit is of the form :

$$y = \frac{a_0}{x + a_1} + a_2 \tag{3.3}$$

where y is the angle of rotation and x is the corresponding voltage. In general, the zero position was physically checked at the start of each test day and the voltage recorded. The coefficient a_2 was then adjusted so that the curve fit returned a zero degree reading. To locate the zero position for roll, the digital protractor was used to measure the inclination of the pitch shaft with the vertical. The zero position for pitch was found hydrodynamically. Here, the foil was subjected to an inflow and the pitch angle adjusted until zero lift force was measured by the tunnel dynamometer. Figure 3-5 shows the plots of the fitted curves against measured voltages for both roll and pitch.

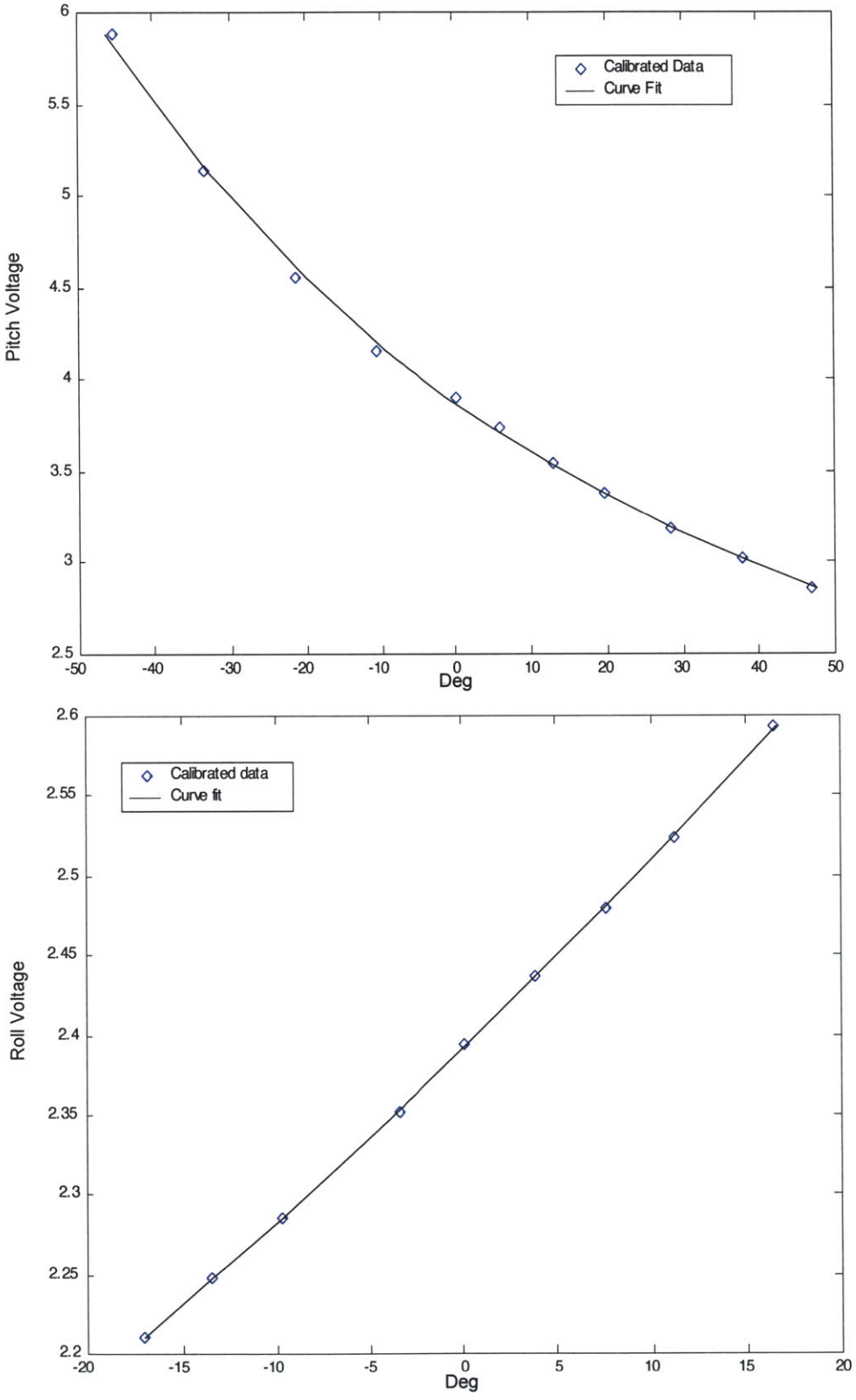

Figure 3-5 : Curve fit for pitch and roll potentiometers

3.3 Torque Sensor

An Entran ELT-2 torque sensor was used to measure the direct torque or input power generated by the roll motor during flapping. The sensor utilizes semiconductor sensing elements and measures torque in both positive and negative directions. It provides a ± 200 mV full scale output for all ranges from 0.2 Nm through 15 Nm. To set up the sensor, an excitation voltage of 12V input was provided to the sensor and the output signal was fed to a Krohn-Hite Model 3384 signal filter. The signal was filtered with a cutoff frequency of 30 Hz and amplified by 8 dB. The sensor exhibited good linearity as can be seen from its calibration as shown in Figure 3-6.

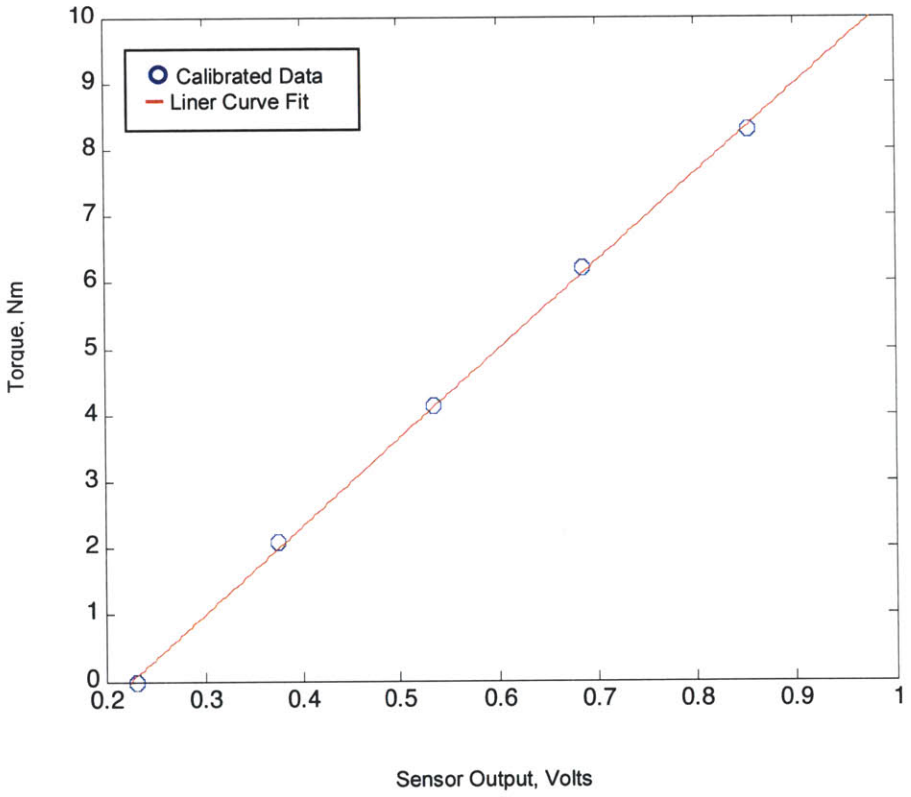

Figure 3-6 : Torque sensor sensitivity

Data from the torque sensor is available but is not presented in this thesis, since hydrodynamic efficiency was evaluated rather than overall actuator efficiency (See Chapter 4 Section 4.3).

3.4 Tunnel Load Cells

Drag/thrust and lift measurements in the tunnel reference frame were made using the dynamometer load cells from Lebow Inc. As the lift forces expected could be twice larger than the drag or thrust, a 25 lb capacity load cell was used to measure the X-force (thrust or drag) and a 50 lb load cell was used for Y-force (lift) measurements. Signals from the cells were fed to the Daytronic 9010 signal conditioner before being channeled to the data acquisition board. Special care had to be taken when mounting the load cells to the dynamometer frame as crosstalk and sensor drifts were encountered when these cells were misaligned or over-constrained in the setup.

To calibrate the sensors, a simple pulley system made from 80/20 T-slotted Aluminum was configured to apply varying loads in the appropriate directions. The weights range from 50 g to 1 kg. To check that the loads were applied correctly, the reading from the other channel was observed to see that it was not picking up a force component, since the X- and Y- forces are orthogonal. Calibration was conducted before the start of each group of tests.

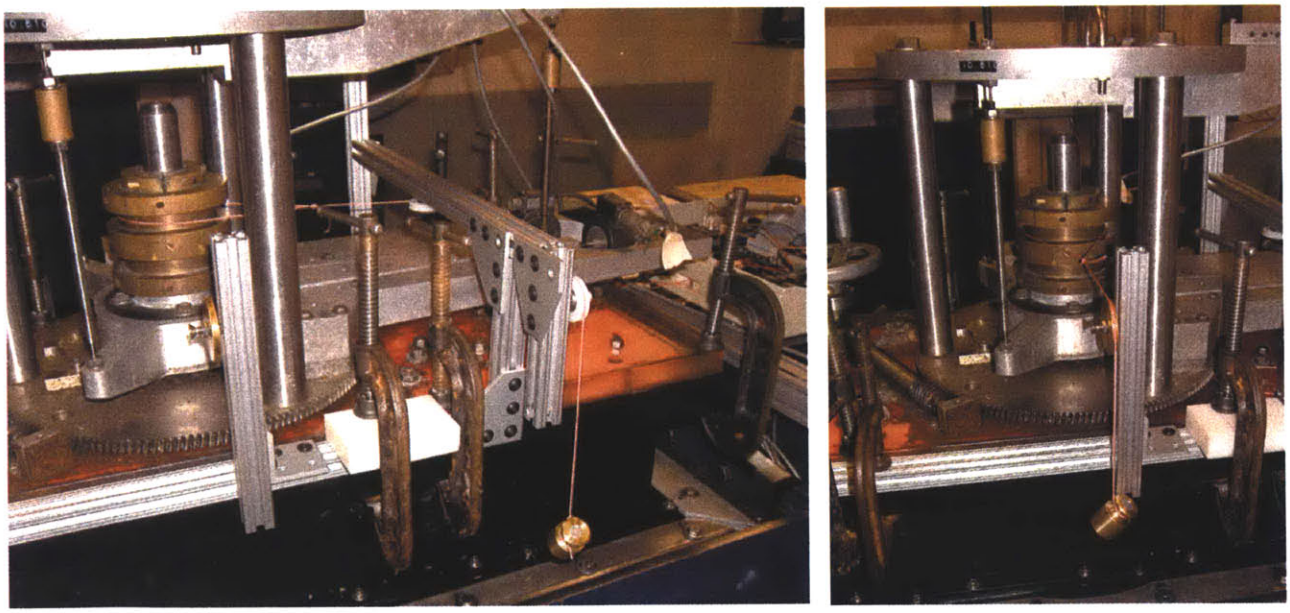

Figure 3-7 : Dynamometer calibration rig. The picture on the left shows the calibration of the X-force (drag/thrust) load cell while the picture on the right shows the calibration in the Y-direction (lift force).

Both load cells were checked for linearity and sensor drift for each group of tests. From the calibration plots, it can be seen that the load cells exhibited good linearity. Also, the sensitivity was also found to be consistent. The variation in the sensitivity calculated from each set of calibration data did not differ by more than 2%. Figure 3-8 and Figure 3-9 show the results from 1 set of calibration. Sensor drift was also observed to be minimal. Drift was found to be less than 1% at the end of each group of tests.

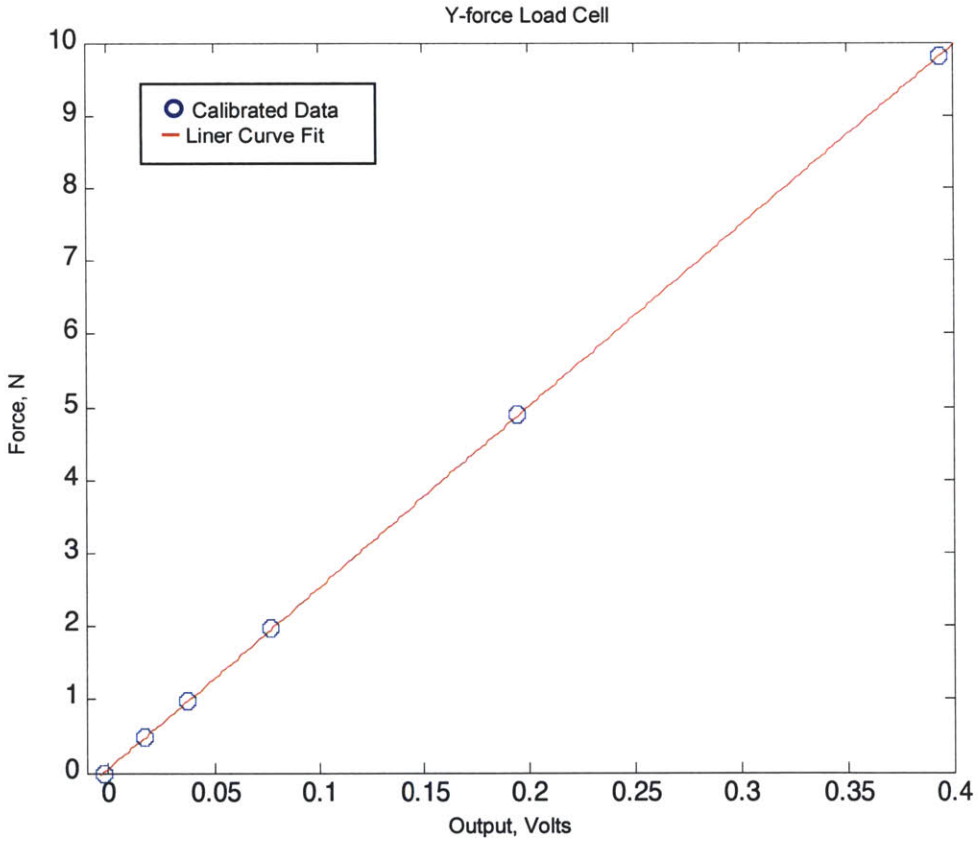

Figure 3-8 : Y-force load cell sensitivity

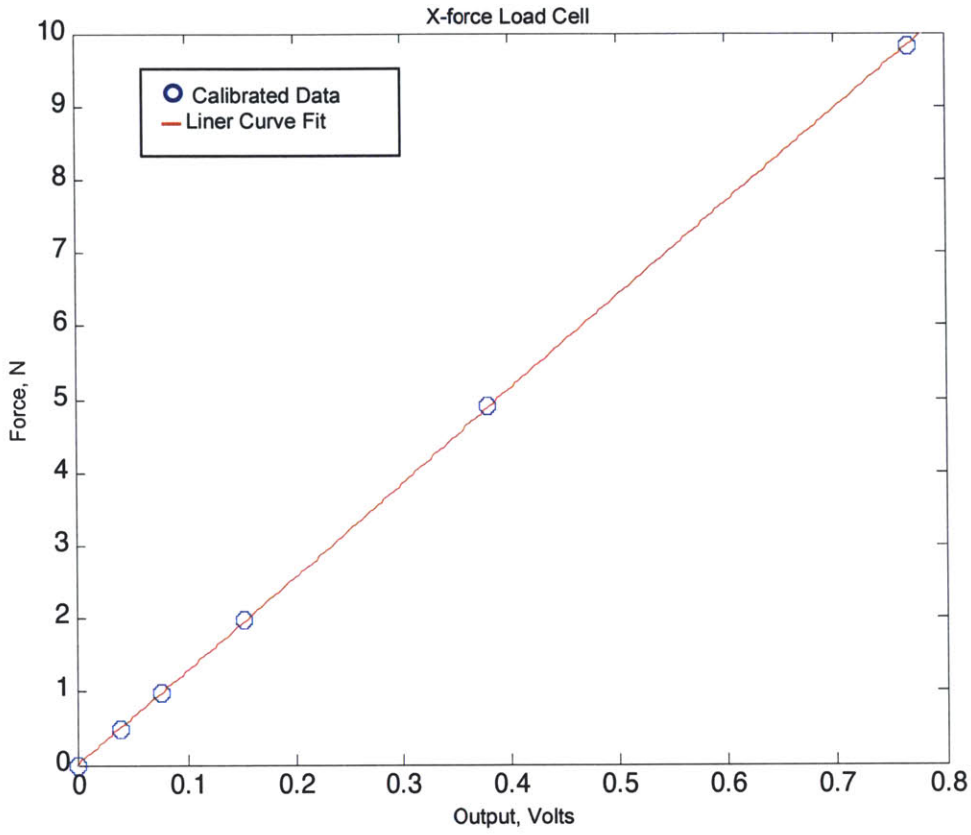

Figure 3-9 : X-force load cell sensitivity

The calibrated sensitivity for each load cell were computed daily and applied to that day's set of tests. It can be seen that the X-force sensitivity was twice that of the Y-force since the load cell had half the capacity of the Y-force load cell. It is not advisable to mount the dynamometer on the side window instead of the top window as it was found that the load of the actuator would then be acting on the Y-force load cell. This pre-compression reduced the span of the load cell such that when the load cell was mounted between the floating and rigid section of the dynamometer frame, it was out of range. While using a higher capacity load cell would eradicate the problem, the force measurements would be close to the noise range of the load cell.

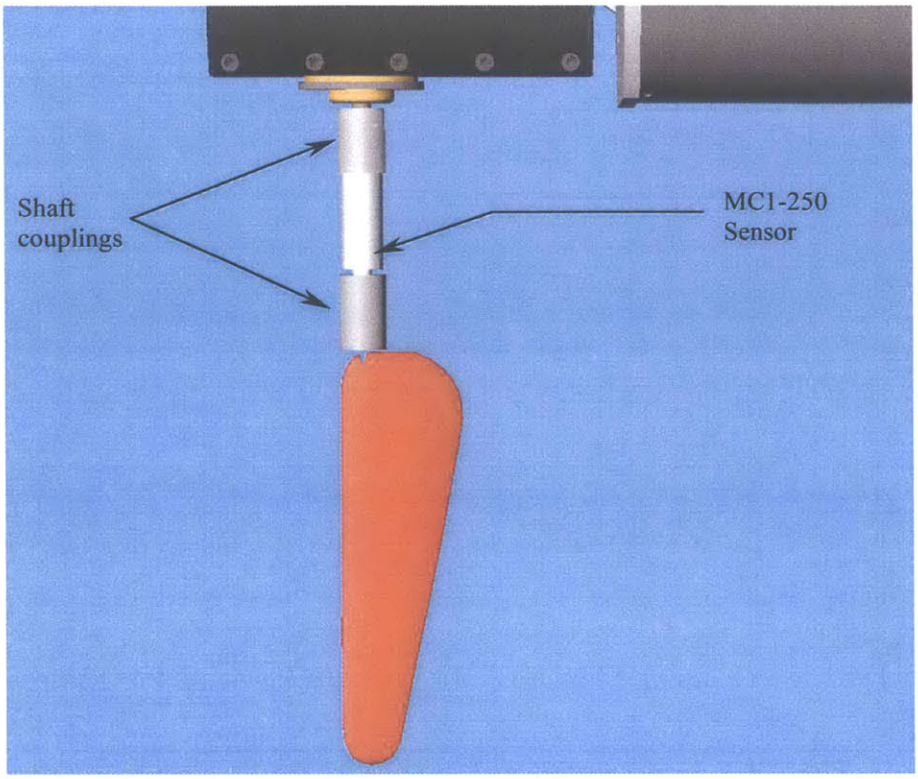

Figure 3–10 : Solidworks drawing of 6-axes sensor assembly

3.5 AMTI Six-axes Sensor

For force and torque measurements, the primary sensor used was the AMTI MC1-250 six-axes water-proof strain gauge sensor. The sensor is basically a six-component transducer, measuring 3 force components (Fx, Fy, Fz) and 3 moment components (Mx, My, Mz). Stainless steel shaft couplings are used to mount the sensor to pitch shaft and foil as shown in Figure 3-10. The construction consists of single cylindrical strain element with strain gauges placed on the outer diameter of the element and wired in four arm bridges. The outer diameter of the strain element and cable are potted with urethane and a stainless steel cover is bonded to the base of the sensor element. Pressure compensation is provided in this sensor with both ID and OD of the element being exposed to water pressure, canceling any pressure differentials across the sensor wall.

The origin of the sensor is taken as located at the geometric center of the element. This location is determined during factory calibration and is found to be 1.28 in away from the edge of the outer body. This origin is used for the moment calculations. A base piece was also designed and machined by McLetchie to sheath the sensor cable and provide a 3/8 in shaft to allow easy mating with the pitch actuator shaft using an off-the-shelf shaft coupling.

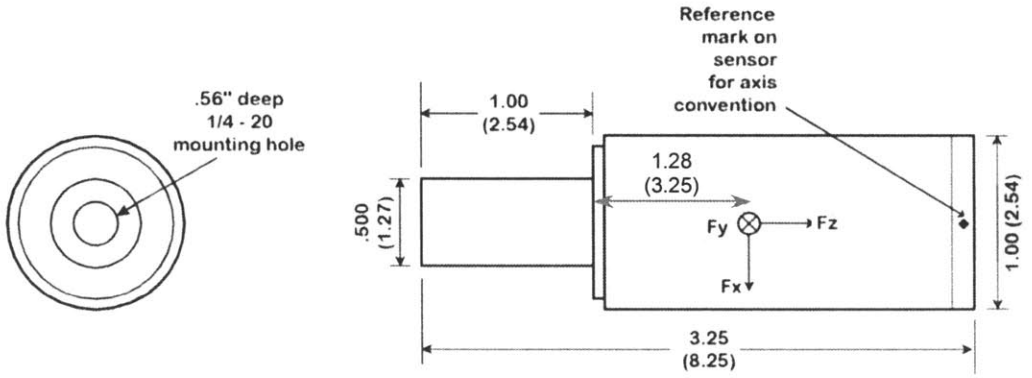

Figure 3-11 : Dimensions of MC1-250 sensor showing axis convention and origin

The signals were amplified using the AMTI MCA-6 amplifier which allows filtering and gains to be set individually for each channel. It also provides an excitation voltage which can be user specified. Here, each channel is supplied with an excitation voltage, V_0 of 10 volts which yields a corresponding output voltage for a given force or moment. Each channel has a sensitivity, S that outputs a dimensionless quantity $\mu V / V / N$ (microvolts per input volt per Newton). Theoretically, without crosstalk between each channel, the output voltage for a given input force or moment is computed using the following equation :

$$\text{Output voltage} = 10^{-6} \times S \times V_0 \times G \times input \tag{3.4}$$

where *input* is the applied force or moment and G is the amplifier gain. The following filter and gain settings were applied :

Channel	Fx	Fy	Fz	Mx	My	Mz
Filter	1050Hz	1050Hz	1050Hz	1050Hz	1050Hz	1050Hz
Gain	4000	4000	4000	1000	1000	4000

Table 3.1 : Settings for MCA-6 amplifier gains and filters

3.5.1 Sensor Cross-talk

There exist a small percentage of cross-talk between each channel of the sensor and hence must be accounted for when converting output voltage signals to forces. In the calibration analysis provided by the factory, a 6×6 sensitivity matrix, $\bar{S}$ is established to define the 'best fit' linear relationship between all 6 inputs and corresponding outputs. Hence for 6 elements of input forces and moments, denoted by $\Delta\vec{F}$, the sensitivity matrix is given by

$$\Delta\vec{V} = \bar{S} \cdot \Delta\vec{F} \tag{3.5}$$

Conversely, the measured voltage signals from any run are used as inputs to determine the forces and moments.

$$\vec{F} = \bar{S}^{-1} \cdot \Delta\vec{V} = \bar{B} \cdot \Delta\vec{V} \tag{3.6}$$

where $\bar{B}$ is the matrix inverse of the sensitivity matrix.

3.5.2 Calibration

To verify the 6×6 sensitivity matrix provided by the factory, a calibration rig was designed to measure the response from all 6 channels. An 80-20 T-slotted Aluminum frame was built round a specialized machine vice with three degrees of rotational freedom as shown in Figure 3-12. A V-block is used to hold the sensor, which is then held in place by the vice. Known weights, (500g and 1 kg) were then hung off a pulley rig in line with the force or moment of interest. The machine vice is then rotated in various configurations to allow forces or moments to be applied along any of the three sensor axes. A clamp with a 2.5in extension was also machined to allow the application of a moment arm. The voltage readings in all 6 channels were recorded for each hanging.

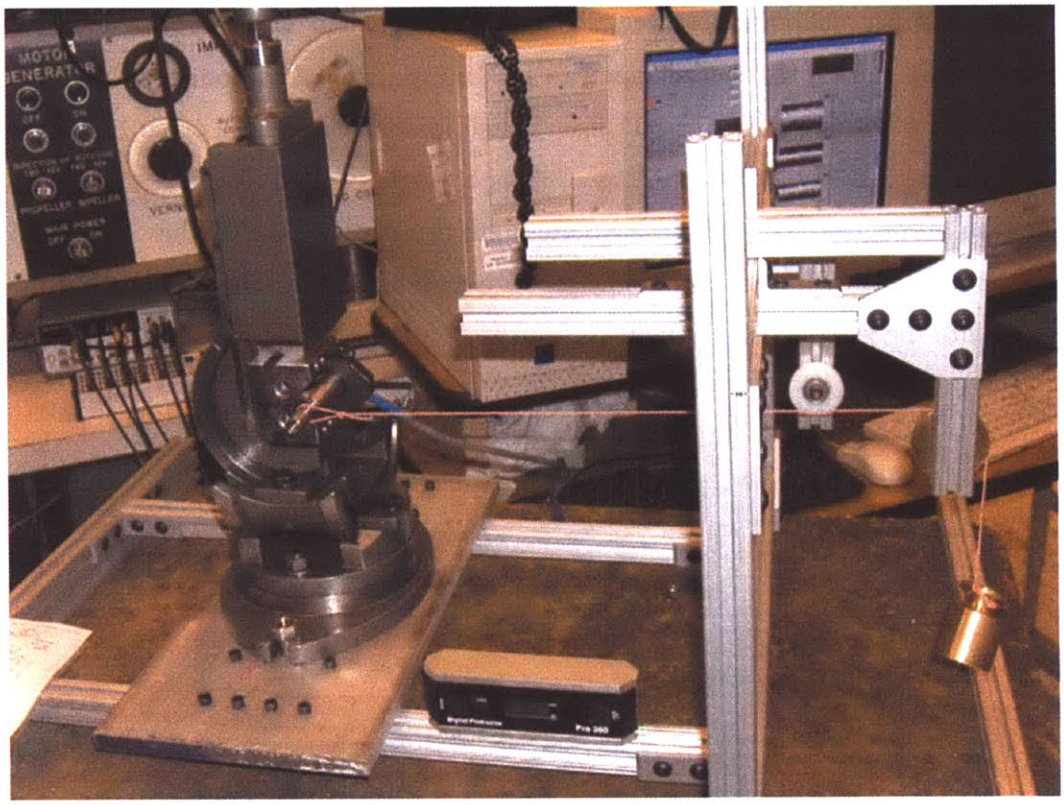

Figure 3-12 : 6-axes sensor calibration rig

A 6×6 force/moment matrix, $\overline{F}$ is then composed for inversion using Matlab. For example, if 10N was applied to the x-axes at the edge of the sensor body, then the F_x channel would register 10N and the M_y channel would pick up a moment of magnitude 0.32Nm since the center of moment was 3.25cm away from the edge. Then the first column of the force vector would be given by

$$\vec{F}_1 = \begin{bmatrix} 10 & 0 & 0 & 0.325 & 0 & 0 \end{bmatrix}^T \tag{3.7}$$

For each particular force setting, the voltage differential in each channel was determined. and assembled as a 6×6 matrix, $\overline{V}$. Hence, the sensitivity matrix, $\overline{S}$ is given by

$$\overline{S} = \overline{F}^{-1}\overline{V} \tag{3.8}$$

With two different weights applied, the matrices are now 6×12 and the pseudo-inverse function in Matlab was employed to determine the sensitivity matrix.

To ensure proper calibration, care had to be taken when applying the loads since any misalignment would cause the other channels to pick up some force component. It would then be difficult to differentiate between cross-talk from actual force components. A pin-hole on the front end of the sensor is marked by the factory as a reference mark for the axis convention. To show the true orientation of the axes, a dowel pin is inserted into this pin hole and held in place with a screw inserted to the treaded end of the sensor. The sensor is then adjusted in the V-block until the dowel pin is aligned with the vertical using a digital protractor.

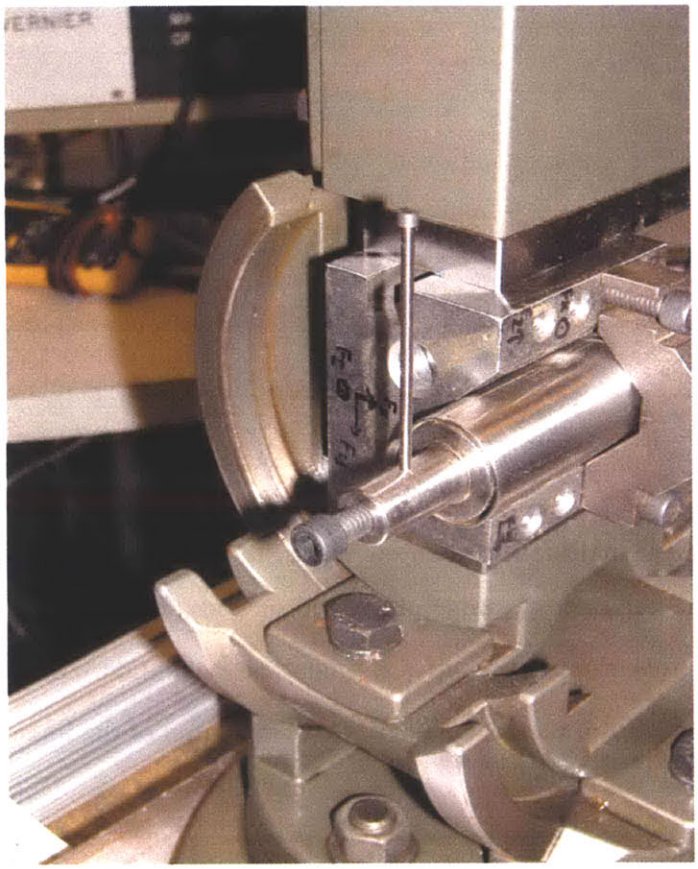

Figure 3-13 : Alignment of sensor axes using dowel pin

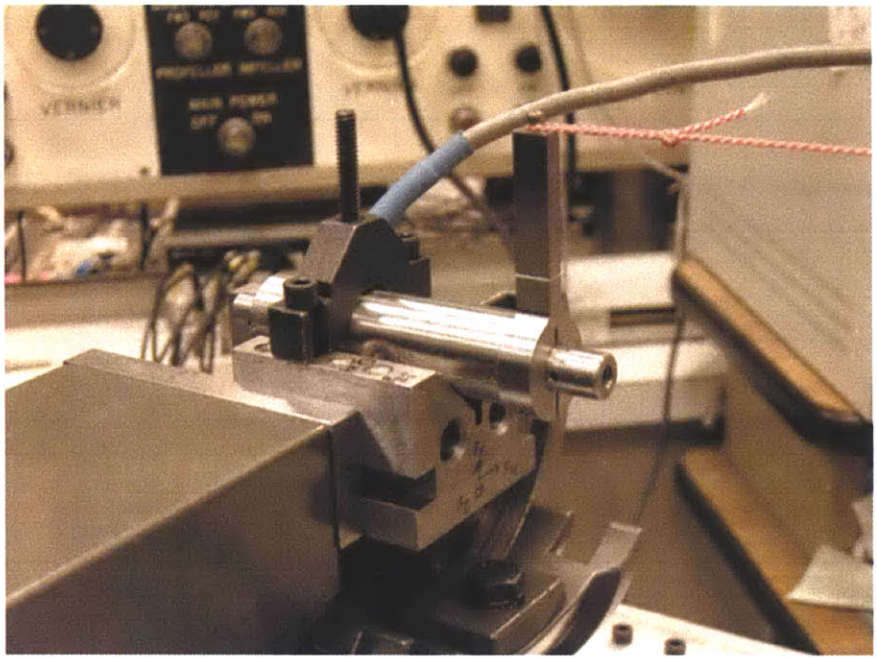

Figure 3-14 : Calibration of the M_y channel. A specially-made calibration clamp with arm allows a force to be applied at 2.5in away from the sensor origin. When a load is applied as shown, the sensor picks up a moment, M_y and force, $-F_z$.

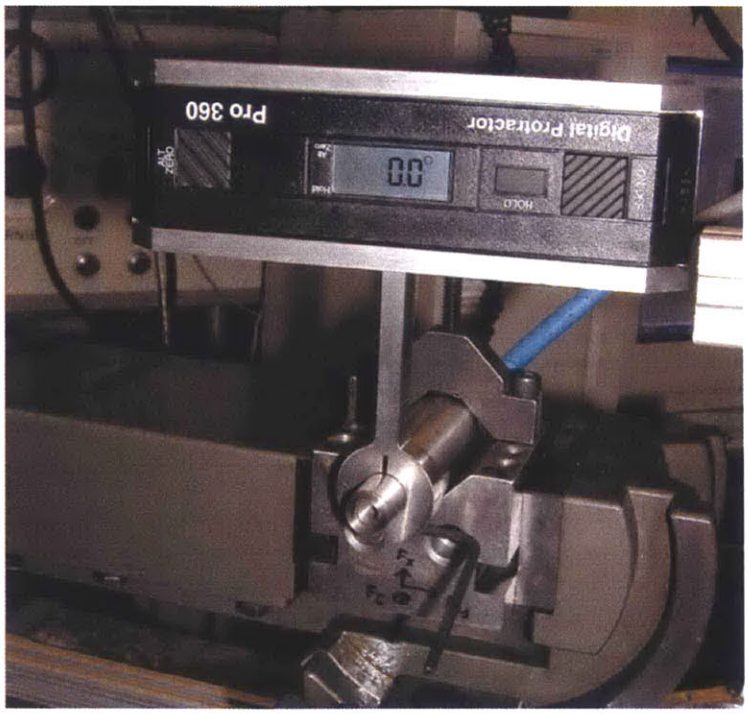

Figure 3-15 : Setting up calibration clamp using a digital protractor

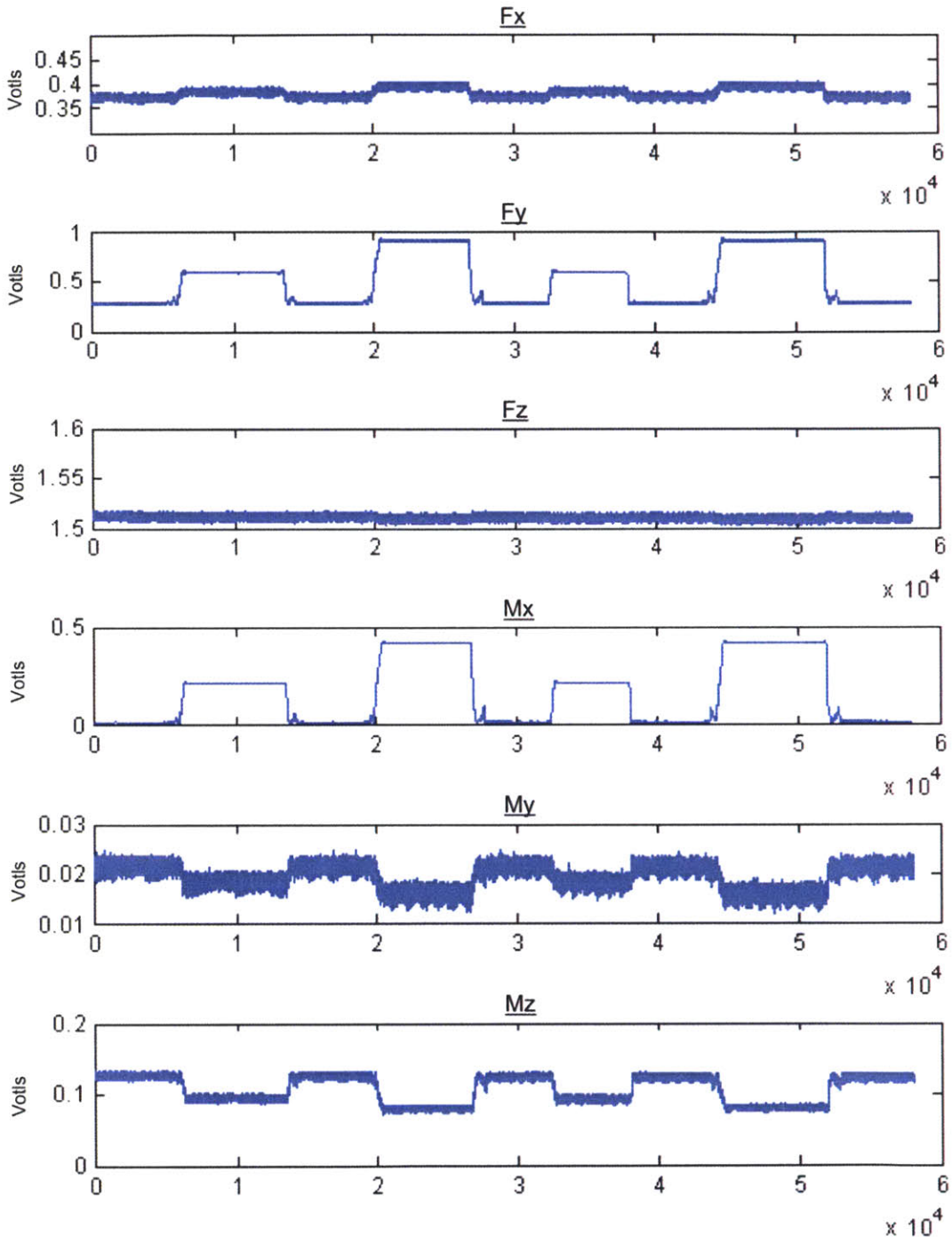

Figure 3-16 : Raw data from calibration of F_y channel. While a force is applied in the y-axes, a moment, M_x is also applied at the same time. All other channels display cross-talk. The horizontal axes show the number of data points while the vertical axes are in volts.

3.5.3 Results of Calibration

For a proper inversion, it was necessary that the matrix had a rank of 6 and that the matrix was not ill-conditioned. This meant that at least 6 different force or moment settings had to be chosen such that each channel (matrix diagonals) was sufficiently loaded. Both the sensitivity matrix, $\overline{S}$ and its inverse, $\overline{B}$ were computed and compared against the factory-supplied sensitivity matrices.

	Calibrated						Factory-supplied					
$\overline{S}$	0.0654	-0.0003	0.0003	0.0698	0.0388	0.0151	0.0638	-0.0024	-0.0000	0.0788	0.0282	0.0188
	0.0012	0.0653	0.0003	-0.0261	0.0022	-0.0079	0.0017	0.0639	0.0002	-0.0331	0.0145	-0.0141
	0.0003	-0.0004	0.0164	0.0059	-0.0198	-0.0188	-0.0006	-0.0004	0.0157	0.0092	-0.0295	-0.0214
	0.0001	0.0016	-0.0001	1.2411	-0.0130	-0.0190	0.0005	0.0001	-0.0004	1.1947	-0.0038	-0.0054
	-0.0031	-0.0013	-0.0007	0.0219	1.2134	-0.0089	0.0001	0	0.0001	0.0138	1.2098	-0.0066
	-0.0008	-0.0073	-0.0000	0.0837	-0.0455	5.0110	0.0005	0.0010	0.0001	0.0062	0.0074	4.8707
$\overline{B}$	15.2745	0.0674	-0.2987	-0.8436	-0.5042	-0.0510	15.6669	0.5839	-0.0023	-1.0121	-0.3747	-0.0604
	-0.2844	15.2993	-0.3108	0.3374	-0.0186	0.0250	-0.4285	15.6332	-0.1400	0.4643	-0.1792	0.0466
	-0.2227	0.4575	61.1897	-0.3043	1.0092	0.2312	0.6138	0.4612	63.6168	-0.5390	1.5256	0.2795
	-0.0007	-0.0194	0.0075	0.8049	0.0089	0.0031	-0.0063	-0.0012	0.0195	0.8372	0.0032	0.0010
	0.0385	0.0178	0.0327	-0.0166	0.8233	0.0014	-0.0011	-0.0001	-0.0063	-0.0095	0.8264	0.0011
	0.0022	0.0229	-0.0003	-0.0132	0.0072	0.1996	-0.0015	-0.0033	-0.0011	-0.0010	-0.0012	0.2053

Table 3.2 : Results from calibration against factory-supplied values

Comparing the diagonals in the $\overline{B}$ matrix against the values provided by AMTI, the error range from 0.38% to 3.86% as shown in Table 3.3. Since the calibrated results are close to that from AMTI, the factory sensitivity values are used in the computation of forces and moments. The factory values represent a more accurate set of calibration since they were evaluated using 10 mass points per channel which extend up to the load capacity of the respective channels.

Calibrated	Factory	% Error
15.2745	15.6669	2.50
15.2993	15.6332	2.14
61.1897	63.6168	3.82
0.8049	0.8372	3.86
0.8233	0.8264	0.38
0.1996	0.2053	2.78

Table 3.3 : Percentage error from $\overline{B}$ matrix diagonals

3.6 Accuracy of Motion Control

To achieve accurate roll and pitch motions, some tuning of the motion controller was necessary. Galil's Windows Servo Design Kit (WSDK) software was used for initial tuning and analysis of the actuator servo system. Fine-tuning was performed with the actuator immersed in water. The system compensation consist of filter parameters that need to be adjusted for fast and accurate response. The filter has three parameters: the damping, KD; the proportional gain, KP; and the integrator, KI. Initially, the KP is adjusted till the error on the pitch and roll amplitudes are minimized. KI is tuned marginally to reduce the position error. The test consists of pure sinusoidal motions of both pitch and roll at 90 deg phase lag. The actual position of each axis over time was recorded using the potentiometers and plotted against a pure sine wave. The following parameters were used :

Test Parameters	
Roll amplitude	7.85 deg
Pitch amplitude	16.5 deg
Period	1.12
Phase	90 deg

Table 3.4 : Test parameters for PID tuning

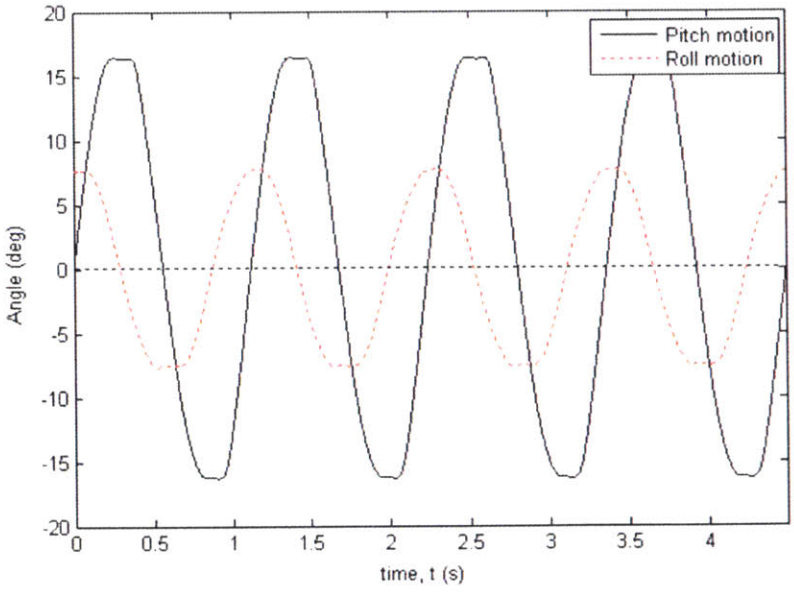

Figure 3-17 : Plot of roll versus pitch motion over time

Figure 3-17 plots the pitch and roll motions over time. It can be seen that the period of the motions and phase lag can be observed to be constant. Figures 3-18 and 3-19 show the actual versus desired motions. For most part, the motion matches the desired except at the turning points where the actual profile is flatter. This error is likely due to the backlash from the motor gear head as it changes direction, causing the motion to plateau as the motor picks up the backlash, thereby loosing precision.

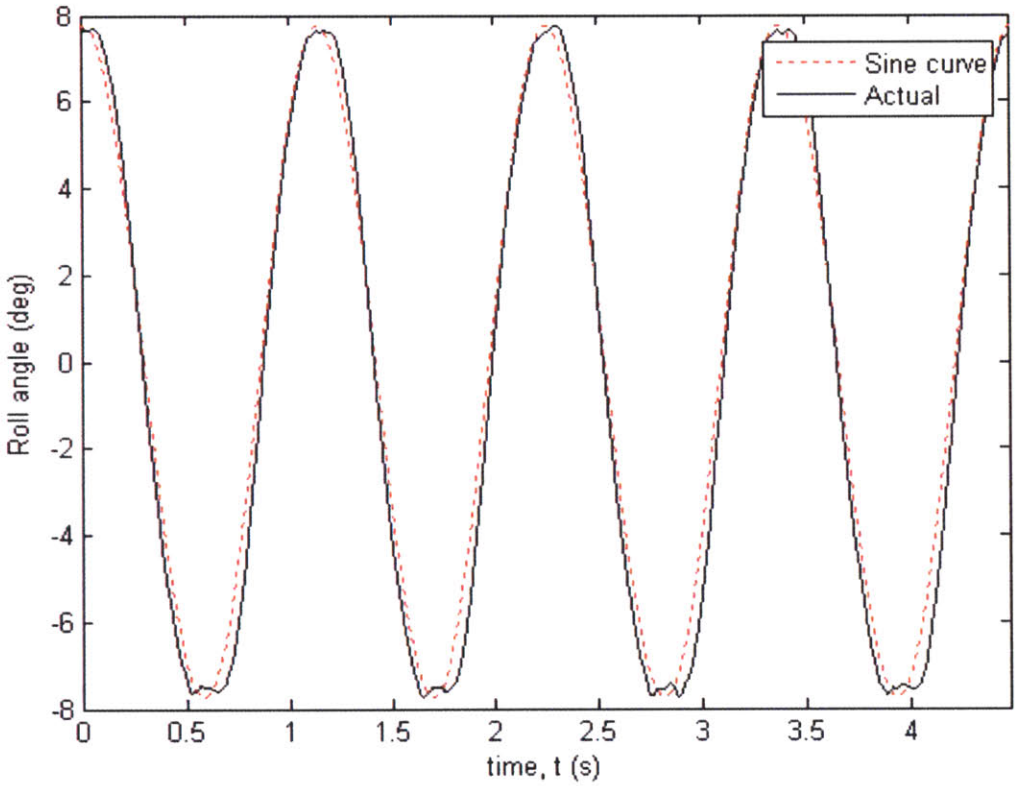

Figure 3-18 : Plot of actual roll motion against desired motion

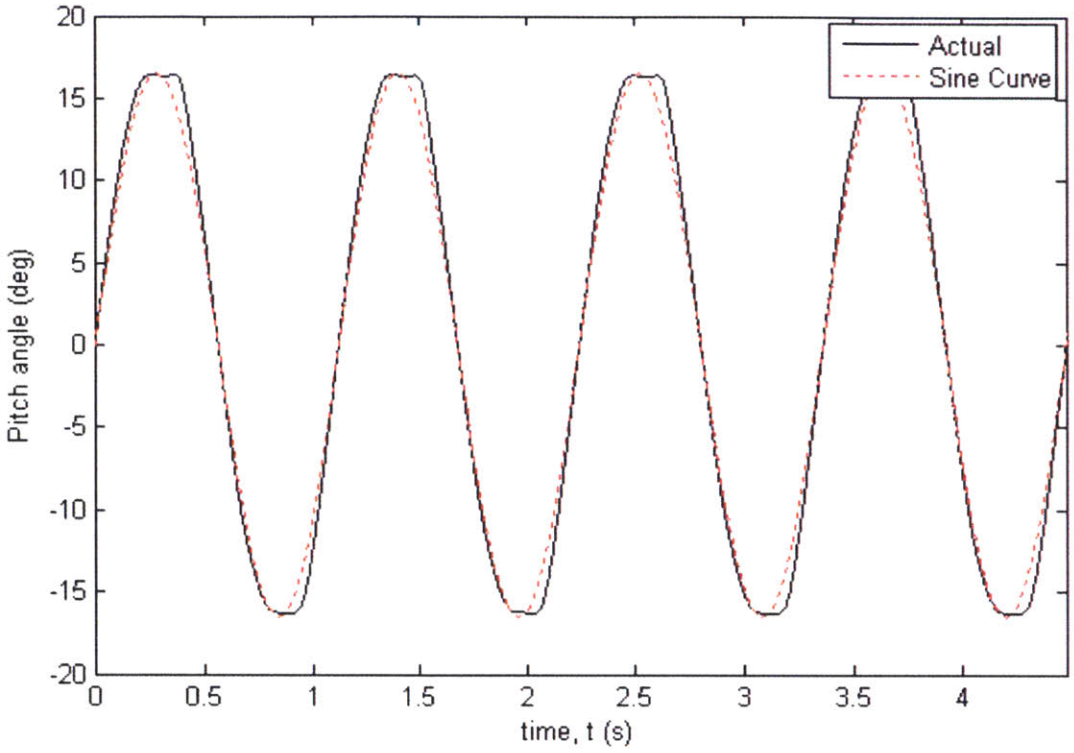

Figure 3-19 : Plot of actual pitch motion against desired motion

The pitch profile deviated slightly over the course of the test runs where a slight kink existed each time there was an upcrossing of the pitch as shown in Figure 4.6. This was most probably caused by the pinching of the pitch shaft seal o-rings on the shaft as it rotated. Owing to difficulties in aligning the pitch shaft during assembly, there is a slight skew of the pitch shaft that causes the shaft seal to be distorted. As the o-ring lubricant began to wear off, the pinch or 'grabbing' intensified as friction began to set in. Fortunately, the motion profile did not deviate drastically from the desired profile and the amplitude and periodicity remained constant.

To achieve the desired pitch amplitude, an initial offset of negative 1.5 deg had to be applied. At this offset, the motor encoder was first reset to zero position using the DP command in Galil before actuation began. This offset takes up the backlash from the pitch gear head and allows the pitch amplitude to correct itself after two cycles.

3.7 Signal Noise Considerations

With a total of 11 analog signals being acquired real-time, some signal conditioning was necessary to achieve accurate and noise-free measurements. In general, the nature of the signal source, configuration of the acquisition device and field wiring were considered to ensure integrity of the acquired data.

3.7.1 Signal Source and Acquisition System

To avoid ground loops, individual 12V batteries provided the input voltages to signal sources where possible. The use of batteries for the torque sensor, pitch and roll potentiometers enabled clean signals to be achieved. BNC cables and interconnects were used to transmit these signals since they provided good shielding from possible EMI. These floating source signals were channeled to the Krohn-Hite Model 3384 signal filter that applied a 30Hz low pass, Butterworth filter to each signal.

The tunnel dynamometer load cells had their own proprietary cables that provided power and transmitted the signals. These were laid out away from the other signal sources and were fed directly into the Daytronic 9010 strain gauge conditioner. Initially, signal drift and cross-talk were observed from both channels. This was later attributed to the improper set-up of the dynamometer floating arm constraints. Also, the mounting of the dynamometer at the side window also accounted for some drift as the actuator was weighing down on the rubber mount of the brass collar. The rubber rebounded slowly which caused the loading on the Y-force sensor to vary over time. The problem was eradicated when the actuator was shifted to the top window.

Another ground-reference signal source was the MC1 6-axes sensor which had its own strain gauge amplifier for signal conditioning. This source was most susceptible to interference noise pick up and its treatment is discussed in the next section. The BNC 2115 connector block allows for both ground-reference and floating analog signal inputs through toggle switches at each input channel. These were set appropriately to reduce errors in data acquisition. In addition, all signals were filtered during post-processing using a 10 Hz low-pass butterworth filter in Matlab. The filtfilt function was used to process the signals in both forward and reverse directions. This results in sequences that have zero-phase distortion and double the filter order.

3.7.2 Ground Loop and MC1 Sensor Noise

The MC1 sensor, when isolated from the actuator, was observed to be picking up some noise when the actuator was in motion. The noise was sinusoidal, with amplitudes of ± 0.1 V per channel. At first, the noise was thought to be caused by EMI from the actuator's interconnect cables and Galil controller. The motion of the power and communication lines during actuating tends to induce some voltage due to the changing magnetic flux in the signal circuit loop. However, even with the sensor placed far away from the actuator, the problem persisted. Nevertheless, the actuator cables were tied down within the housing and power lines were kept separate from the rest.

The likely cause of the noise was from the power supply of the Galil controller sharing a common ground loop with the sensor. The noise was attenuated when the Galil power supply was kept separate from the sensor's power supply. To this end, the MC1 was powered from an ESP Kleenline Isolator Conditioner to clear up the ground loop and reduce power line harmonic distortion. The Galil controller was powered up from a separate power outlet as connecting it to the isolator only served to accentuate the problem. Even so, this did not eradicate the problem totally as they seem to be sharing the same building system ground. However with this effort, it did reduce the noise level to within the millivolts range. Potential noise sources such as power lines and the PC monitor were kept away from the BNC cables.

The Galil power supply was also observed to toggle the base voltages of the MC1 sensor each time the power supply was turned on and off. This occurred whenever the motor encoders were reset to zero with the DP command. However, once the motors were operating, the base voltages reverted back to the initial values. As a precautionary measure, for all test runs, the data acquisition was turned on when the sensor was at zero pitch and roll positions so that the base voltages could be recorded. Once the actuator completed a set number of cycles, the actuator was returned to zero position and the base voltages recorded again before the data acquisition was turned off.

For consistency, the MC1 sensor was turned on for at least an hour in the water tunnel before measurements were taken. This allowed the sensor's temperature to stabilize in the water and avert fluctuations in strain gauge outputs as a result of temperature variations.

3.8 Voltage to Force/Moment Conversion

Even without any force or moment applied, there exist some nominal voltage from each channel of the sensor that is amplified by the MC6 amplifier system. For a given test run, this offset in voltage must be accounted for in the evaluation of forces and moments. The force/moment vector can be written as

$$\vec{F} = \overline{B} \cdot \vec{V} + \vec{\varphi} \tag{3-9}$$

To determine the offset, $\vec{\varphi}$, the hydrodynamic force on the foil in a flow stream is measured for a given inflow speed. The foil is set at zero pitch and roll position, i.e., zero angle of attack and thus experiences a drag force, D and net weight, $b - mg$ (where b is the buoyancy force and mg is the weight of the foil) . There is also a net moment where z_D is the moment arm due to the drag force. Hence the force vector, $\vec{F}_{\varphi_0}$ in such a condition is defined as

$$\vec{F}_{\varphi_0} = \begin{bmatrix} D \\ 0 \\ b - mg \\ 0 \\ -D \cdot z_D \\ 0 \end{bmatrix} \tag{3-10}$$

Setting this condition as the base condition, then the offset is derived as follows,

$$\vec{F}_{\varphi_0} = \begin{pmatrix} 0 \\ 0 \\ 0 \\ 0 \\ 0 \\ 0 \end{pmatrix} = \overline{B} \cdot \vec{V}_0 + \vec{\varphi} \qquad \text{or} \tag{3-11}$$

$$\vec{\varphi} = -\overline{B} \cdot \vec{V}_0 \tag{3-12}$$

where $\vec{V}_0$ is the sensor output consisting of six channel voltages (with its x-axis aligned with the inflow).

In general, the sensor axes could be misaligned with the flow, resulting in the other channels picking up some components of the drag force. This particular loading condition of zero angle of attack in an inflow is thus chosen as it allows the resultant forces and moment to be measured accurately. In this setting, any sensor misalignment is only contained in the x- and y-axes, with some small angle, ε with the inflow. However, since the y-channel picks up a sine component of the drag force, this is negligible for any small angle, ε.

In general, the net weight of the foil and coupling does not factor into the computation for lift and thrust, since the force vector is orthogonal to the XY plane. Hence we only need to determine the drag of the foil for each flow velocity. This is determined by the following procedure.

1. Measure the sensor voltages, $\vec{V}_1$ with sensor hanging vertically downwards in water, with foil attached at one end.

2. With an inflow, measure the sensor voltages, $\vec{V}_2$ at zero angle of attack. The drag force and moments are then computed as follows :

$$\text{Given} \qquad \vec{F}_1 = \begin{pmatrix} 0 \\ 0 \\ b-mg \\ 0 \\ 0 \\ 0 \end{pmatrix}, \qquad \vec{F}_2 = \begin{pmatrix} D \\ 0 \\ b-mg \\ 0 \\ -D \cdot z_D \\ 0 \end{pmatrix} \tag{3-13}$$

$$\text{Then} \qquad \vec{F}_2 - \vec{F}_1 = \overline{B} \cdot \left(\vec{V}_2 - \vec{V}_1 \right) \qquad \text{or} \tag{3-14}$$

$$D = B_{1j} \cdot (\vec{V}_2 - \vec{V}_1) \tag{3.15}$$

3.9 Force Rotations

The multi-axes sensor is mounted onto the foil and follows the foil trajectory as it rolls and pitch. To evaluate the lift, thrust and efficiency, it is necessary to translate the forces and moments measured to the tunnel or flow reference frame. Translated lift and drag forces can then be compared against that obtained from the tunnel dynamometer.

3.9.1 Rotation Matrices

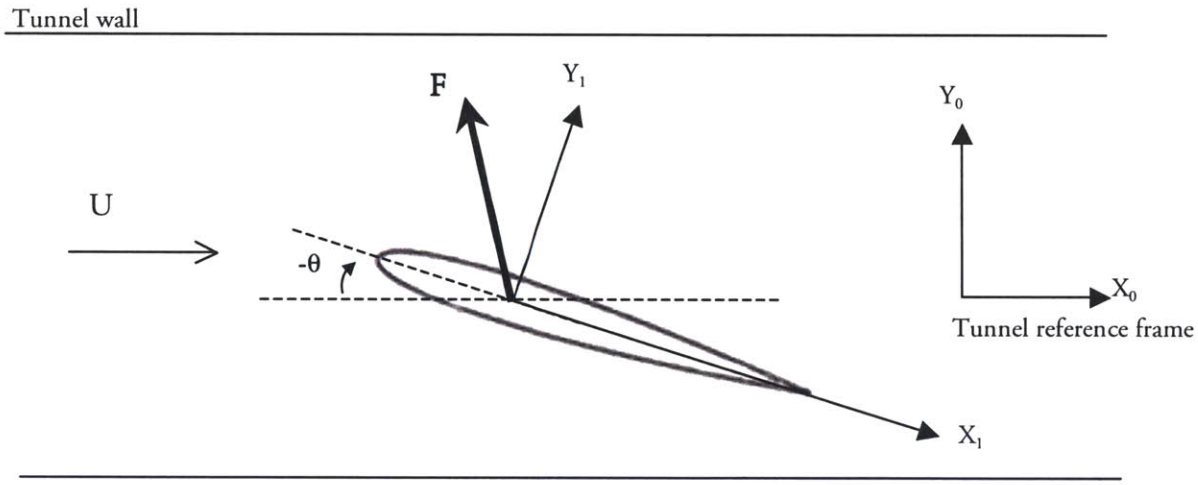

Figure 3-20 : Reference frames for foil, sensor and tunnel

Any force, F or moment, M can be resolved to its components in the foil co-ordinate system and rotated to the tunnel reference frame. A rotation matrix to resolve forces and moments to the roll reference frame is first applied:

$$\bar{\Omega}_\theta = \begin{pmatrix} \cos\theta & -\sin\theta & 0 & 0 & 0 & 0 \\ \sin\theta & \cos\theta & 0 & 0 & 0 & 0 \\ 0 & 0 & 1 & 0 & 0 & 0 \\ 0 & 0 & 0 & \cos\theta & -\sin\theta & 0 \\ 0 & 0 & 0 & \sin\theta & \cos\theta & 0 \\ 0 & 0 & 0 & 0 & 0 & 1 \end{pmatrix} \tag{3.16}$$

$$\vec{F}_{roll} = \begin{pmatrix} Fx_2 \\ Fy_2 \\ Fz_2 \\ Mx_2 \\ My_2 \\ Mz_2 \end{pmatrix} = \bar{\Omega}_\theta \vec{F}_1 = \bar{\Omega}_\theta \cdot \begin{pmatrix} Fx_1 \\ Fy_1 \\ Fz_1 \\ Mx_1 \\ My_1 \\ Mz_1 \end{pmatrix} \tag{3-17}$$

A roll rotation matrix is then applied to translate the forces and moments from the roll reference frame to the tunnel reference frame.

$$\bar{\Omega}_\phi = \begin{pmatrix} 1 & 0 & 0 & 0 & 0 & 0 \\ 0 & \cos\phi & -\sin\phi & 0 & 0 & 0 \\ 0 & \sin\phi & \cos\phi & 0 & 0 & 0 \\ 0 & 0 & 0 & 1 & 0 & 0 \\ 0 & 0 & 0 & 0 & \cos\phi & -\sin\phi \\ 0 & 0 & 0 & 0 & \sin\phi & \cos\phi \end{pmatrix} \tag{3.18}$$

$$\Rightarrow \vec{F}_0 = \bar{\Omega}_\phi \vec{F}_{roll} = \bar{\Omega}_\phi \bar{\Omega}_\theta \vec{F}_1 \tag{3.19}$$

3.9.2 Sensor Misalignment

As the multi-axes sensor is mounted on to the foil on one end and the pitch shaft on the other end using shaft couplings, there is a possibility that the sensor co-ordinates are not perfectly aligned with the foil. There exist some small angle, ε, between the foil reference frame and the sensor co-ordinate system.

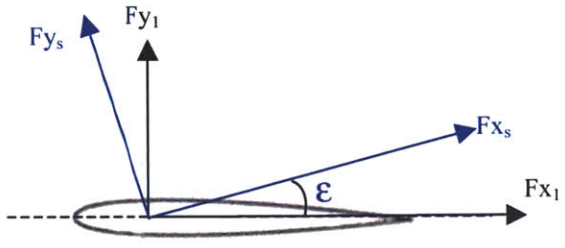

Figure 3-21 : Angular misalignment of sensor co-ordinate system

Before the force rotation matrices can be applied, it is thus necessary to determine ε and apply a rotation matrix to translate the measured sensor forces to the foil reference frame.

$$\bar{\Gamma} = \begin{pmatrix} \cos\varepsilon & -\sin\varepsilon & 0 & 0 & 0 & 0 \\ \sin\varepsilon & \cos\varepsilon & 0 & 0 & 0 & 0 \\ 0 & 0 & 1 & 0 & 0 & 0 \\ 0 & 0 & 0 & \cos\varepsilon & -\sin\varepsilon & 0 \\ 0 & 0 & 0 & \sin\varepsilon & \cos\varepsilon & 0 \\ 0 & 0 & 0 & 0 & 0 & 1 \end{pmatrix} \tag{3.20}$$

$$\bar{F}_1 = \begin{pmatrix} Fx_1 \\ Fy_1 \\ Fz_1 \\ Mx_1 \\ My_1 \\ Mz_1 \end{pmatrix} = \bar{\Gamma}\ \bar{F}_{sensor} = \bar{\Gamma} \cdot \begin{pmatrix} Fx_s \\ Fy_s \\ Fz_s \\ Mx_s \\ My_s \\ Mz_s \end{pmatrix} \tag{3.21}$$

In determining the offset, φ, the sensor's F_y channel picks up a component of the drag force given that the sensor is at some ε from the inflow. However, since ε is small, we can assume that the y-component or Fy_s is close to zero.

$$Fy_s = D\sin\varepsilon \approx 0 \tag{3.22}$$

Thus equation 3.15 remains valid for small angles of ε.

3.9.3 Determination of ε

The misalignment, ε can be found experimentally by pitching the roll at some angle θ in both positive and negative directions and measuring the hydrodynamic forces.

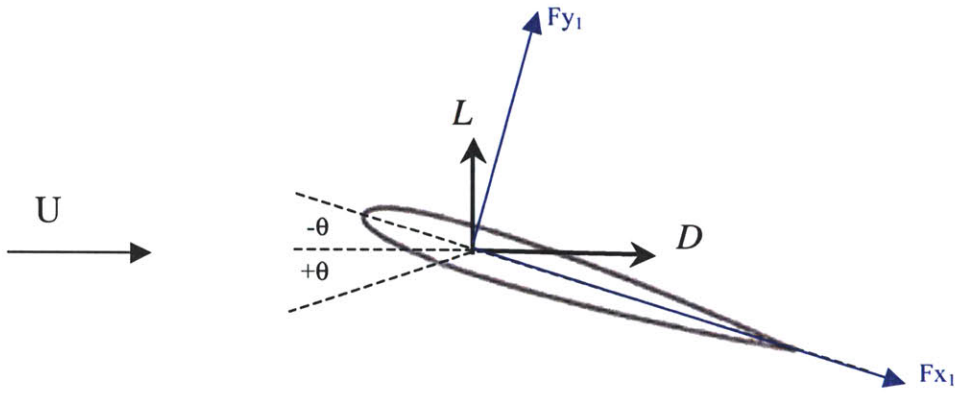

Figure 3-22 : Foil at angle of attack, θ to determine ε

At negative θ, the foil experiences both a lift force, L and drag force, D as shown in Figure 3-22. In the foil reference frame, applying a full rotation matrix,

$$\bar{\Omega} = \begin{pmatrix} \cos\theta & \sin\theta & 0 & 0 & 0 & 0 \\ -\sin\theta & \cos\theta & 0 & 0 & 0 & 0 \\ 0 & 0 & 1 & 0 & 0 & 0 \\ 0 & 0 & 0 & \cos\theta & \sin\theta & 0 \\ 0 & 0 & 0 & -\sin\theta & \cos\theta & 0 \\ 0 & 0 & 0 & 0 & 0 & 1 \end{pmatrix} \tag{3.23}$$

We derive the forces resolved in the foil reference frame as

$$F_{l,\ +\theta} = \bar{\Omega} \cdot \begin{bmatrix} D \\ L \\ 0 \\ 0 \\ 0 \\ 0 \end{bmatrix} \tag{3.24}$$

If the sensor is aligned at an angle, ε from the foil reference frame, then the sensor forces are computed as follows :

$$F_{s,\ +\theta} = \bar{\Gamma}^T \cdot F_{l,\ +\theta} = \bar{\Gamma}^T \cdot \bar{\Omega} \cdot \begin{bmatrix} D \\ L \\ 0 \\ 0 \\ 0 \\ 0 \end{bmatrix} = \bar{B}\vec{V}_{+\theta} + \varphi \tag{3.25}$$

where $\bar{\Gamma}$ is the rotation matrix as defined in equation 3.20 and $\vec{V}_{+\theta}$ is the vector of the six channel voltages measured. Similarly in the negative θ direction, we get

$$F_{s,\ -\theta} = \bar{\Gamma}^T \cdot F_{l,\ -\theta} = \bar{\Gamma}^T \cdot \bar{\Omega} \cdot \begin{bmatrix} D \\ -L \\ 0 \\ 0 \\ 0 \\ 0 \end{bmatrix} = \bar{B} \cdot \vec{V}_{-\theta} + \varphi \tag{3.26}$$

Subtracting Equation 3.26 from 3.25, we get

$$\bar{\Gamma}^T \cdot \bar{\Omega} \cdot \begin{bmatrix} 0 \\ 2L \\ 0 \\ 0 \\ 0 \\ 0 \end{bmatrix} = \bar{B} \cdot (\vec{V}_{+\theta} - \vec{V}_{-\theta}) \tag{3.27}$$

or

$$\begin{bmatrix} 0 \\ 2L \\ 0 \\ 0 \\ 0 \\ 0 \end{bmatrix} = \bar{\Omega}^{-1} \cdot \bar{\Gamma} \cdot \bar{B}(\vec{V}_{+\theta} - \vec{V}_{-\theta}) \tag{3.28}$$

The force equation as expressed in Equation 3.28 allows us to solve for ε that returns a maximum value for the second element in the LHS column vector. Neither the lift nor drag force needs to be determined explicitly. The misalignment, ε was found experimentally to be 1.47 deg.

Chapter 4

Propulsive Forces and Efficiency

4.1 General Description

Thrust, lift and efficiency were evaluated mainly using the data recorded by the MC1 six-axes sensor. The forces and moments signals from the MC1 sensor were recorded by Labview and saved as a test file for processing by Matlab. The average thrust and lift forces were found by applying the force rotation matrices and averaging the data over 10-15 cycles. The forces measured by the tunnel dynamometer were used to verify the forces measured by the MC1 sensor. Mean force data are presented in terms of the non-dimensional force coefficient based on planform area of the foil instead of the swept area as would a propeller. The hydrodynamic efficiency was then measured by comparing the power output from the product of average thrust and velocity against the sum of the power input applied to the pitch and roll axes. To show repeatability of the results, four sets of repeated runs were carried out and the standard deviation evaluated.

4.1.1 Parametric Space

The parametric space for the simple harmonic experiments is as follows :

- Heave/Chord ratio, $h_{0.7} / c$, 1.00 to 2.00 (0.5 increment)
- Strouhal number, 0.2 to 0.6 (0.1 increment)
- Maximum AOA, 15^0 to 45^0 (5^0 increment)

The boundary of parametric space represents the mechanical limits of the actuator. Heave/chord ratio is bounded by the maximum roll possible before tunnel side wall effects are significant. The actuator was operable for oscillations of up to 1.5 Hz, beyond which the actuator stalls. Further fine-tuning of the PID limits would have been necessary to achieve higher oscillation frequencies. The lower bound of the parametric space is also the point at which the angle of attack profiles start to get corrupt (drag-producing). Nevertheless, force data at higher Strouhal numbers and AOA have been well mapped out by Flores and Polidoro. McLetchie began to investigate regimes of low Strouhal numbers and AOA but experienced appreciable errors due to difficulties in estimating pitch position and velocities. The invesitation of this regime would have helped to verify some of McLetchie's results.

The experiments were conducted mainly at inflow speeds of 0.5 m/s and 1.0 m/s. The lower speed was used to achieve higher Strouhal numbers. The speed was monitored at all times by the LDV and maintained to within $\pm$ 0.01 m/s variance.

4.1.2 Test Procedure

The following procedure was adopted for each test run. Setting the foil at zero roll and pitch positions at the start and end of each run ensures that the drag of the foil and sensor is recorded at the start and end. This value is then applied in the force offset vector, $\vec{\varphi}$.

1. For a particular $h_{0.7}/c$, St and α_{max}, input desired roll and pitch amplitude, and period.
2. Run tunnel at desired flow speed.
3. Set foil to zero position for roll and pitch.
4. Start data acquisition to record zero values.
5. Jog foil to offset position to account for backlash.
6. Reset encoder position to zero.
7. Begin motion. Foil jogs to maximum roll position and hold for 5 secs before oscillating.
8. When motion stops, jog foil to zero position for roll and pitch.
9. Record zero values and end data acquisition.

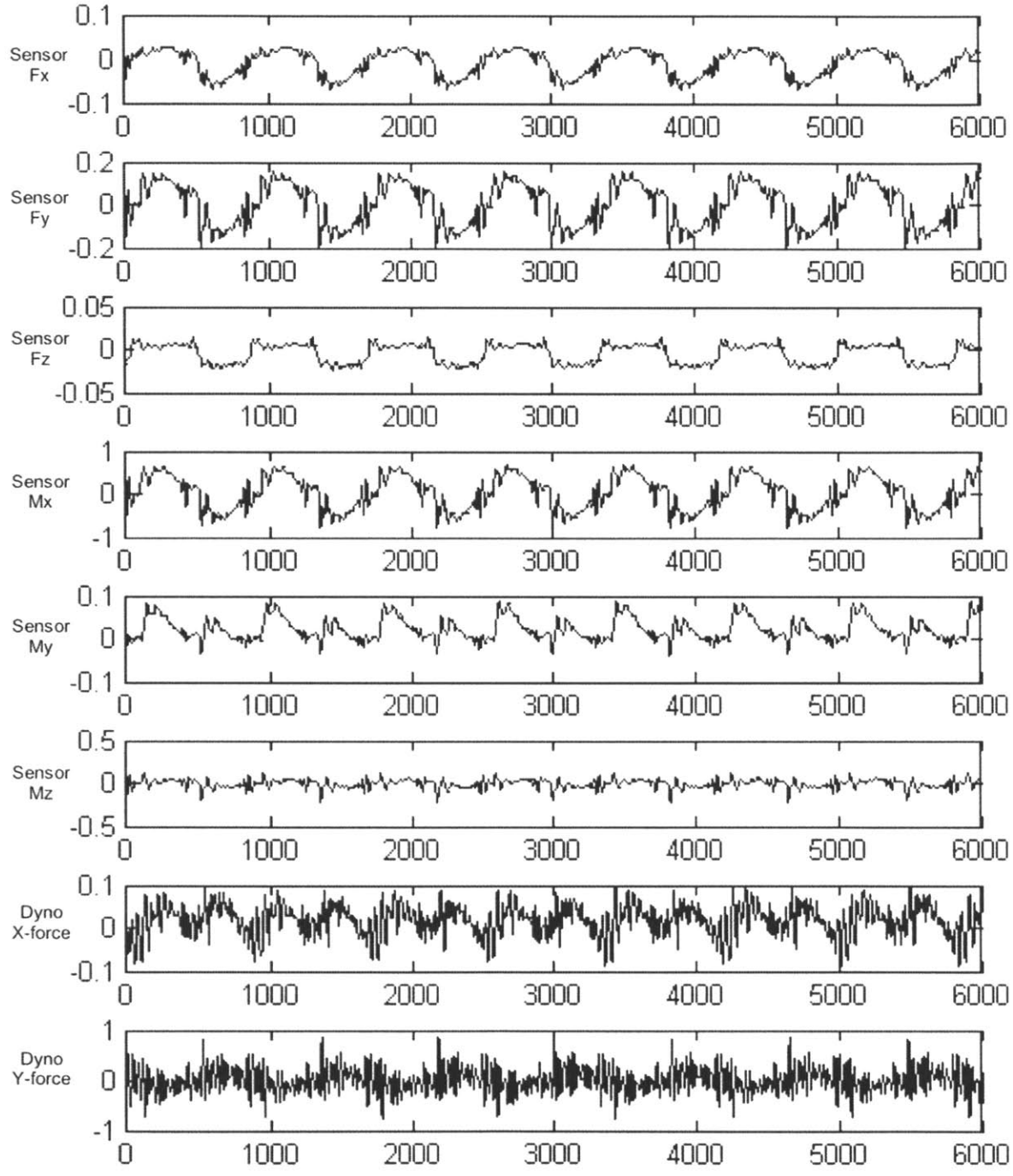

Figure 4-1 : Raw data recorded at St = 0.2 , $h_{0.7} / c$ = 1.5, St and α_{max} = 20^0. Signals are in voltages and the horizontal axis shows the sample points. Sampling rate is at 500 Hz. The first six plots show voltage signals from the MC1 sensor. The last two are from the tunnel dynamometer X- and Y- load cells.

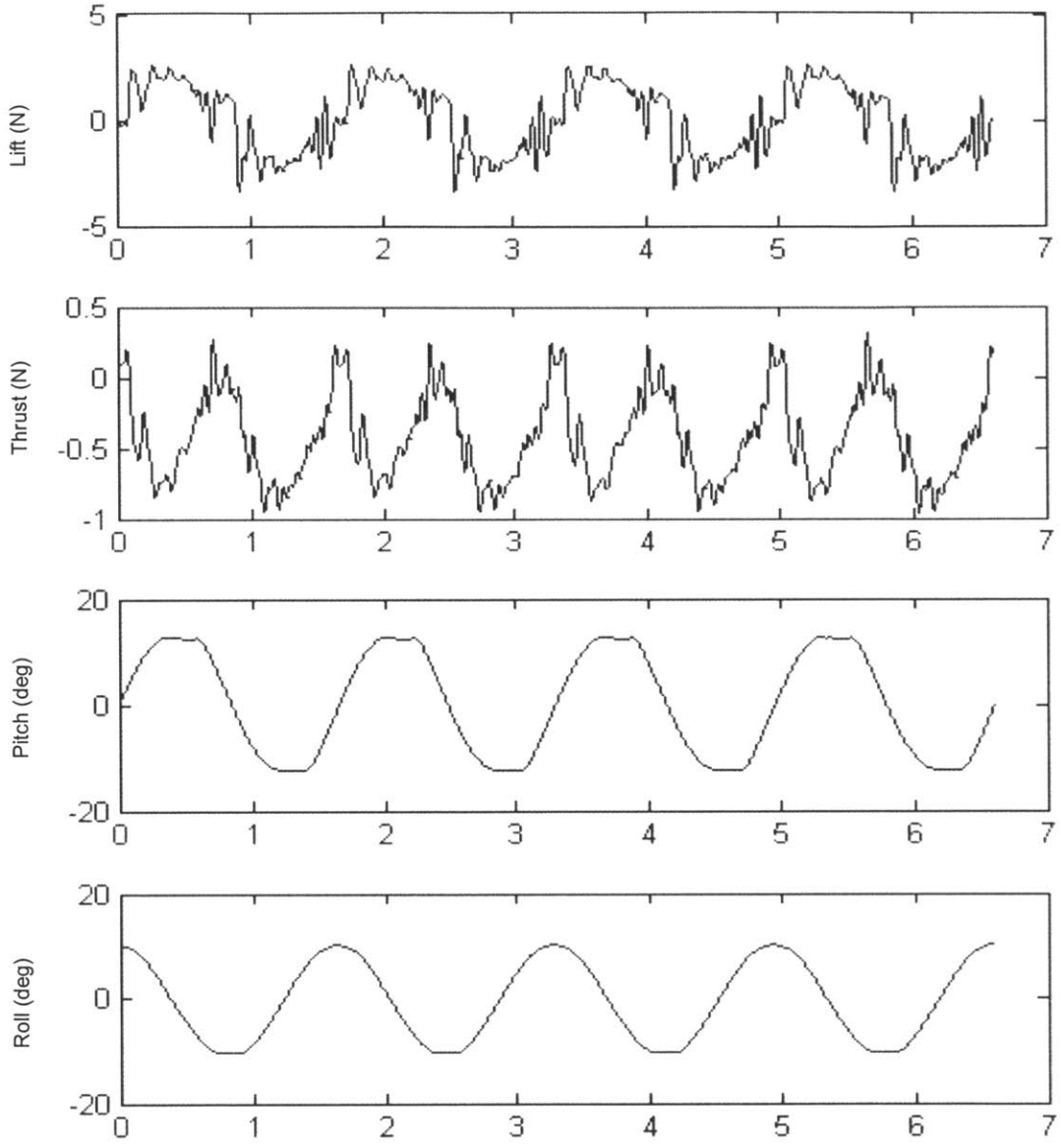

Figure 4-2 : Processed data recorded for St = 0.2 , $h_{0.7} / c$ = 1.5, St and α_{max} = 20^0. The horizontal axis is the time, in secs. The lift and thrust are in the tunnel reference frame. The forces are computed using the MC1 sensor measurements taken from the data set as shown in Figure 4-3.

4.2 Thrust Measurements

The average thrust is given by

$$\bar{F}_{x_0} = \frac{1}{T}\int_0^T F_{x_0}(t)dt \tag{4.1}$$

where $\bar{F}_{x_0}$ is the x-force translated into the reference frame of the tunnel, averaged over one flapping cycle. By axes convention, x is positive upstream. The thrust coefficient is thus defined as

$$C_T = \frac{-2\bar{F}_{x_0}}{\rho U^2 \bar{c} S} \tag{4.2}$$

where U is the flow velocity, S is the span and $\bar{c}$ is the average chord length. Tables 4-1 to 4-3 show the results for C_T for three different roll amplitudes, with induced two-dimensional heave to chord ratio, $h_{0.7}/c$ of 1.0, 1.5 and 2.0. Due to the limited number of experimental points taken, the results are presented in the form of tables instead of contour plots as done previously for Flores and Mcletchie's data set. The data marked with the asterisk (*) are taken from repeat runs (see Section 4.4). Also, the shaded cells represent experimental points where no data was collected for reasons stated earlier in Section 4.1.2.

Maximum AOA	St			
	0.2	0.3	0.4	0.5
45				1.296
40			0.434	1.374
35		0.294	0.696	1.457
30		0.399	0.736	1.533
25	0.128	0.452	0.918	1.487
20	0.195	0.436	0.974	1.397
15	0.209*	0.391	0.869	

Table 4-1 : Results of C_T, for $h_{0.7}/c$ =1.0, from St = 0.2 to 0.5 and α_{max} = 15^0 to 40^0

Maximum AOA	St				
	0.2	0.3	0.4	0.5	0.6
45				0.824	1.901
40			0.633	1.014	2.006
35		0.360	0.734	1.143	2.043
30		0.509	0.735	1.403	2.093
25	0.184	0.527	0.777	1.374	1.760
20	0.200	0.599*	0.695	1.260	1.489
15	0.241	0.444	0.552	0.720	

Table 4-2 : Results of C_T , for $h_{0.7} / c$ =1.5, from St = 0.2 to 0.6 and α_{max} = 15^0 to 45^0

Maximum AOA	St				
	0.2	0.3	0.4	0.5	0.6
45				0.895	1.457
40			0.602	1.095	1.673
35			0.719	1.220	1.747
30			0.872	1.311	1.783
25	0.226	0.385	0.866	1.312	1.660
20	0.159	0.463	0.708	1.065*	0.990
15	0.233*	0.450	0.549	0.705	

Table 4-3 : Results of C_T , for $h_{0.7} / c$ =2.0, from St = 0.2 to 0.6 and α_{max} = 15^0 to 45^0

The general trend of the results compare well with those of Read (for the 2-dimensional case), Flores and McLetchie. Quantitatively, the magnitudes are closer to those obtained by McLetchie. In general, the thrust coefficients are the lowest at lower Strouhal numbers and α_{max} values. The coefficient starts to increase with increasing values of both Strouhal number and α_{max} .

For the case of $h_{0.7} / c$ = 1.0, a peak thrust coefficient of 1.6 was recorded at St = 0.5 and α_{max} = 30^0. Also, it appears that a higher peak could be achieved at St = 0.6. McLetchie's plot for the case of $h_{0.7} / c$ = 1.0 confirms this. For the case of $h_{0.7} / c$ = 1.5, a peak of 2.09 was measured at St = 0.6 and α_{max} = 30^0, and another of 2.04 was recorded at α_{max} = 35. At $h_{0.7} / c$ = 2.0, the maximum thrust coefficients now occur at the same Strouhal numbers but have lower magnitudes of 1.78 at α_{max} = 30^0 and 1.75 at α_{max} = 35^0.

Comparisons with two-dimensional cases show similar trends. Read measured a peak of 2.17 for thrust coefficient for the two-dimensional case. The maximum thrust coefficient recorded by McLetchie was 2.2 at $h_{0.7}/c = 1.5$.

It can be seen that for a given Strouhal number, the thrust coefficient increases with the maximum angle of attack. However beyond a critical α_{max} value, the thrust coefficient will start to decrease. A similar trend is seen in terms of thrust dependency on roll amplitudes. The maximum thrust coefficient is recorded at $h_{0.7}/c$ of 1.5. At a higher roll amplitude ($h_{0.7}/c = 2.0$), the peak thrust coefficient is lower. It is possible that an optimal roll amplitude can be found (between the heave to chord ratio of 1.5 to 2.0) for which the thrust coefficient can be maximised.

The left and bottom 'borders' of the parametric space represent the boundaries for which the angle of attack profiles tend to corrupt, that is, some regions of the foil would encounter negative angles of attack, resulting in drag instead of thrust production. Here, the results at St = 0.2 show very low thrust production for all α_{max} values. This low thrust boundary represent the transition in the wake from drag to thrust producing vortices [4]. At high α_{max}, the transition to thrust does not occur until a Strouhal number of about 0.4.

It must be noted that at the experimental points for which low thrust values were measured (St $\leq$ 0.3, 15 $\leq \alpha_{max} \leq$25), there are large errors associated with the results. Hence there are some inconsistencies in the trend relating C_T to variations in α_{max}. A repeatability and error analysis is done to investigate this further in Section 4.4.

Also, the thrust coefficients here were evaluated based on planform area. A more appropriate normalization would have been to use the projected swept area, which would have produced numerically smaller results. The Strouhal numbers, maximum angle of attacks and $h_{0.7}/c$ values were computed from an Excel iterative solver based of an equivalent heave motion in 2D. These prescribed definitions were applied to allow direct comparisons with past results on both two- and three-dimensional experimental studies.

4.2.1 Thrust Measurements From Dynamometer

To verify the accuracy of the MC1 six-axes sensor, force measurements from the X-force load cell was compared directly with the thrust, F_{x_0} computed using resolved force data from the MC1 sensor. To account for sensor drift, the X-force load cell data was first zeroed by the offset recorded before the motion began, that is, at zero roll and pitch, in an inflow. The net force calculated now includes the drag contribution from the foil and actuator. To calculate the effective thrust, the drag component would have to be subtracted from the force calculations. This drag component is measured in separate experiments where the voltage readings were taken before and immediately after the actuator and foil was subjected to an inflow. This was done for all the different flow speeds used in the propulsion experiments.

Ideally the drag measurements would have been consistent. However, this was not found to be so due to a varying flow existing within the Aluminum housing and fairing. The fairing was secured to the housing using long Aluminum bars which introduced a 0.5 in gap between the fairing and housing. This allowed a small slip stream to develop and circulate within the housing, resulting in an unstable flow. Fortunately, the flow was steady for the initial set of runs and the forces measured were in good agreement. Table 4.4 shows the results from both sensors.

$h_{0.7} / c$ = 1.5				
St = 0.3				
Max AOA	**Dynamometer (N)**	**MC1 Sensor (N)**	**Absolute Error (N)**	**% Error**
20	-0.7341	-0.79021	0.05611	7.6
25	-0.7423	-0.89081	0.14851	20
30	-0.7225	-0.86051	0.13801	19.1
35	-0.5395	-0.60921	0.06971	12.9
St = 0.4				
Max AOA	**Dynamometer (N)**	**MC1 Sensor (N)**	**Absolute Error (N)**	**% Error**
15	-0.9187	-0.93421	0.01551	1.7
20	-1.1588	-1.17591	0.01711	1.5
25	-1.2999	-1.31461	0.01471	1.1
30	-1.2645	-1.24381	-0.02069	1.6
35	-1.1871	-1.24281	0.05571	4.7
40	-1.0615	-1.07051	0.00901	0.8

Table 4.4 : Thrust measurements from tunnel dynamometer and MC1 six-axes sensor

Elsewhere, where the thrust measurements are in poor agreement, the difference in values appears to be offset by some constant. It appears that the drag of the actuator and foil had shifted as a result of a changing internal flow within the housing. Nevertheless, it is observed that the increment in thrust between each rise in α_{max} is almost similar for both sensors. Overall, within the good calibrated range (St = 0.4 data set), the %error of the six-axes sensor from the dynamometer ranged from 0.8 to 4.7%. Within this limited range of force comparison, it offers some evidence that the MC1 sensor is reliable for force measurements.

4.3 Hydrodynamic Efficiency

The hydrodynamic efficiency of the foil is defined as the ratio of power output over power input :

$$\eta = \frac{P_{out}}{P_{in}} \tag{4.3}$$

where the power output is the product of the time-averaged thrust and flow velocity

$$P_{out} = TU = -\bar{F}_{x_0} U \tag{4.4}$$

Here, P_{in} is the power input to the fluid, measured by the MC1 sensor mounted to the foil shaft. While the torque sensor attached to the roll motor could measure the direct power input from the electric motor, a large amount of the power is actually used to move the inertial mass of the pitch canister. The motor power input is found to be in the order of ten greater than the power transmitted to the flow. Thus, using the power input from the motor would result in the overall efficiency of the actuator being significantly reduced. This information would then be motor-specific and is then useful only in power system design applications using similar motors. Hence, a more useful approach instead, would be to use the power input measured by the MC1 sensor to calculate hydrodynamic efficiency of the foil. This way, the hydrodynamic efficiency of the foil can then be compared directly with other foil designs in future.

The power input is made up two components, the power input to the pitch axis, P_{in_θ} and to the roll axis, P_{in_ϕ}. The former is calculated by multiplying the applied pitch axis moment with the pitch angular velocity, $\dot{\theta}$, as follows :

$$P_{in\_\theta} = M_{pitch}\dot{\theta} \tag{4.5}$$

Since the measured pitch moment is equal in magnitude but opposite in direction to the applied pitch moment,

$$M_{pitch} = -M_z \tag{4.6}$$

the pitch power component is then given by

$$P_{in\_\theta} = -M_z\dot{\theta} \tag{4.7}$$

Similarly, the product of the applied roll moment and roll angular velocity gives the power input to the roll axes. As the origin of the sensor is located 1.28 inches away from the foil root, the applied moment is then

$$M_{roll} = F_{y_2} \cdot R_0 - M_{y_1} \tag{4.8}$$

where M_{y_1} is the measured pitch moment and F_{y_2} is the lift force in the roll reference frame. R_0 is the moment arm, measured from the roll axis to the sensor origin. Hence,

$$P_{in\_\phi} = M_{roll}\dot{\phi} \tag{4.9}$$

where $\dot{\phi}$ is the roll angular velocity. Total power input is thus given by

$$P_{in} = P_{in\_\theta} + P_{in\_\phi} \tag{4.10}$$

The hydrodynamic efficiencies from the propulsion experiments are presented in Tables 4-5 to 4-7. The data marked with the asterisk (*) are taken from repeat runs (see Section 4.4).

Maximum AOA	St			
	0.2	0.3	0.4	0.5
45				0.251
40			0.136	0.295
35		0.231	0.243	0.343
30		0.351	0.288	0.424
25	0.254	0.478	0.418	0.483
20	0.493	0.565	0.535	0.54
15	0.703*	0.653	0.614	

Table 4-5 : Efficiency, η, of foil flapping at $h_{0.7} / c = 1.0$

Maximum AOA	St				
	0.2	0.3	0.4	0.5	0.6
45				0.190	0.269
40			0.246	0.251	0.315
35		0.276	0.321	0.311	0.358
30		0.426	0.361	0.427	0.463
25	0.378	0.52	0.479	0.507	0.456
20	0.513	0.828*	0.536	0.614	0.578
15	0.803	0.788	0.599	0.603	

Table 4-6 : Efficiency, η, of foil flapping at $h_{0.7} / c = 1.5$

Maximum AOA	St				
	0.2	0.3	0.4	0.5	0.6
45				0.202	0.229
40			0.238	0.27	0.279
35			0.32	0.352	0.336
30			0.448	0.429	0.402
25	0.153	0.328	0.54	0.518	0.489
20	0.361	0.473	0.553	0.604*	0.498
15	0.802*	0.593	0.647	0.658	

Table 4-7 : Efficiency, η, of foil flapping at $h_{0.7} / c = 2.0$

In a reverse fashion to the C_T results, the efficiency peaks at the lower end (at low Strouhal and α_{max} values) and then decreases with increasing St and α_{max} values. This is as expected since at the low thrust regions, little energy is lost through kinetic energy being imparted to the flow. The maximum efficiency recorded is about 0.8 at St = 0.3 and $\alpha_{max} = 20^0$ for $h_{0.7} / c = 2.0$. Its location corresponds with that from McLetchie's plot although numerically the peak values differ. It is noted that his values at this low thrust regime were susceptible to high percentage errors. Read's plot also shares the same peak location with measured efficiencies not exceeding 0.7.

Higher roll amplitudes result in greater energy expanded in moving the foil through the large oscillations. It is only at higher frequencies where greater thrust is generated such that the efficiency is seen to be improving. Following this trend, the efficiency data is compared with the corresponding C_T plots. Here, results show that for low α_{max} values, thrust generally increases with Strouhal number, without much penalty to efficiency. This would be of much interest to power systems design as an optimal point can be identified for relatively high thrust production with good efficiencies. For example, at $h_{0.7} / c$ of 1.5, we see relatively high efficiencies occurring at St = 0.5, and α_{max} of 15^0 and 20^0. This offers a good design point where efficiencies of more than 0.6 can be achieved with thrust coefficients ranging from 0.7 to 1.2.

It must be noted that at the low thrust regimes (St $\leq$ 0.3, $15 \leq \alpha_{max} \leq 25$), the percentage errors associated with the measurements remain significant. To this end, several sets of repeated runs were recorded to assess repeatability and determine the standard deviations. This is discussed in detail in the following section.

4.4 Error and Repeatability Analysis

To evaluate the repeatability of the results, four sets of five repeated runs were performed. Test cases where large experimental errors could be expected were selected. In this case, runs were done at experimental points where low thrust values were found. Also, cases where there were reasonable thrust and efficiency were repeated to verify the results. The standard deviation for each set was evaluated and the error expressed as the percentage of the standard deviation from the mean.

To have a sense for the precision of the MC1 six-axes sensor, the range was also determined. This is taken as the average of the difference between the highest and lowest sample from the mean. The results are presented in Tables 4-8 below.

Case I	$h_{0.7}$ / c = 1.0, St = 0.2, α_{max} = 15^0			
		C_T	P_{in}	η
	Mean	0.2088	0.2515	0.7031
	Std dev	0.0158	0.0101	0.0589
	% Error	7.5787	4.0280	8.3726
	Range (±)	0.0221	0.0137	0.0715
Case II	$h_{0.7}$ / c = 1.5, St = 0.3, α_{max} = 20^0			
		C_T	P_{in}	η
	Mean	0.5995	0.6122	0.8284
	Std dev	0.0216	0.0124	0.0339
	% Error	3.6041	2.0322	4.0874
	Range (±)	0.0291	0.0196	0.0940
Case III	$h_{0.7}$ / c = 2.0, St = 0.2, α_{max} = 15^0			
		C_T	P_{in}	η
	Mean	0.2333	0.2459	0.8024
	Std dev	0.0212	0.0031	0.0698
	% Error	9.0670	1.2462	8.7001
	Range (±)	0.0245	0.0047	0.0794
Case IV	$h_{0.7}$ / c = 2.0, St = 0.5, α_{max} = 20^0			
		C_T	P_{in}	η
	Mean	1.0645	1.4908	0.6040
	Std dev	0.0234	0.0435	0.0082
	% Error	2.1941	2.9204	1.3536
	Range (±)	0.0283	0.0639	0.0123

Table 4-8 : Error analysis for repeat runs

The average range of C_T is found to be in the order of ± 0.026, or ± 0.044 N in terms of absolute thrust. In other words, the sensor exhibits a precision of about ± 0.044 N. As such, the percentage error, which is taken as the fraction of standard deviation over the mean, is naturally higher at the lower thrust runs (Cases I and III). Likewise a larger percentage error for η arises for Cases I and III.

In all cases, the measured efficiency is 0.6 and above. Hence, while percentage errors appear to be tolerable (about 4~9 %, with the exception of Case IV), the absolute error range is large. This error range would be less than ideal for the low efficiency runs. Since the thrust is used directly in the computation of power output, the error gets transferred to the efficiency calculations. The error for η is thus a combination of errors from power input and thrust measurements. The data is, however, inconclusive in determining which error contribution is more dominant in influencing the efficiency results.

Cases II and IV show promising results in terms of identifying design points with combinations of relatively high thrust with good efficiencies. However, It must be noted that the high thrust coefficients are artificially high since planform area was used to normalize the forces. A more useful normalization would be to use the swept area, which in this case, is function of both the roll and pitch amplitudes, and the distance between the foil and the roll axis of rotation. To avoid complicated geometrical calculations, an approximation using just the roll amplitude, ϕ_0 is applied. Considering the foil is at 0^0 pitch at both extremes of the roll motions, the swept area is approximated by

$$SA = 2\phi_0\left[\left(R_0 + S\right)^2 - R_0^2\right] \tag{4.11}$$

where R_0 is the distance from center of rotation to the root of the foil and S is the span of the foil. Hence the thrust coefficient would be defined by

$$C_{T_{SA}} = \frac{\bar{F}_{x_0}}{\frac{1}{4}\rho\phi_0 U^2\left[\left(R_0 + S\right)^2 - R_0^2\right]} \tag{4.12}$$

By this definition, the effective thrust coefficient is significantly smaller. Table 4-9 presents the more acceptable values for C_T. As an additional check, the ideal efficiency (based on actuator disc theory, [10]) was computed using the swept area thrust coefficient. Not surprising, the measured efficiency is found to be lower than the ideal efficiency, which serves as the upper bound for propulsors.

Cases	Planform C_T	Swept Area C_T	Measured η	Ideal η
II	0.5995	0.1118	0.828	0.974
IV	1.064	0.1493	0.604	0.965

Table 4-9 : Coefficients of thrust based on swept area

Next, to show repeatability, the force and position time trace for each repeat run were plotted over each other for comparison. For clarity, only three runs for a particular test case are plotted over each other. The test case where there were large percentage errors (Case I) and another where small percentage errors were encountered (Case IV) were chosen. Figures 4-3 and 4-4 show the runs from Case I and Case IV respectively, where the lift force (roll reference frame), drag force, pitch and roll are plotted.

It can be seen that for both cases, the plots overlapped reasonably well for all measurements. The multiple runs for Case IV were in better agreement. For Case I, it would seem that there was a slight variation in the roll motion for each run, either in magnitude or in phase, which might have accounted for the variations in results. This is less obvious for Case IV due to the scaling of the plots for larger amplitudes.

Small perturbations were observed in the roll plots. Visual checks showed that the roll motion was physically stable. Instead, the roll potentiometer seemed to be picking up some intermittent electromagnetic interference. Fortunately, the noise was only present in this last stage of the tests; the quality of the earlier runs remains intact.

Overall, the drag force oscillated below the zero mean, hence producing a net thrust. At the same time, its frequency is twice that of the lift. This is because thrust is produced on both the positive and negative stroke of the roll motion.

The recorded pitch motion is fairly sinusoidal. Some backlash appears to occur at the maxima of the pitch motion, causing the peaks to plateau slightly. A kink, observed in every upcrossings of the pitch time trace, can be attributed to the 'grabbing'effect of the pitch shaft seal (as explained earlier in Section 3.6).

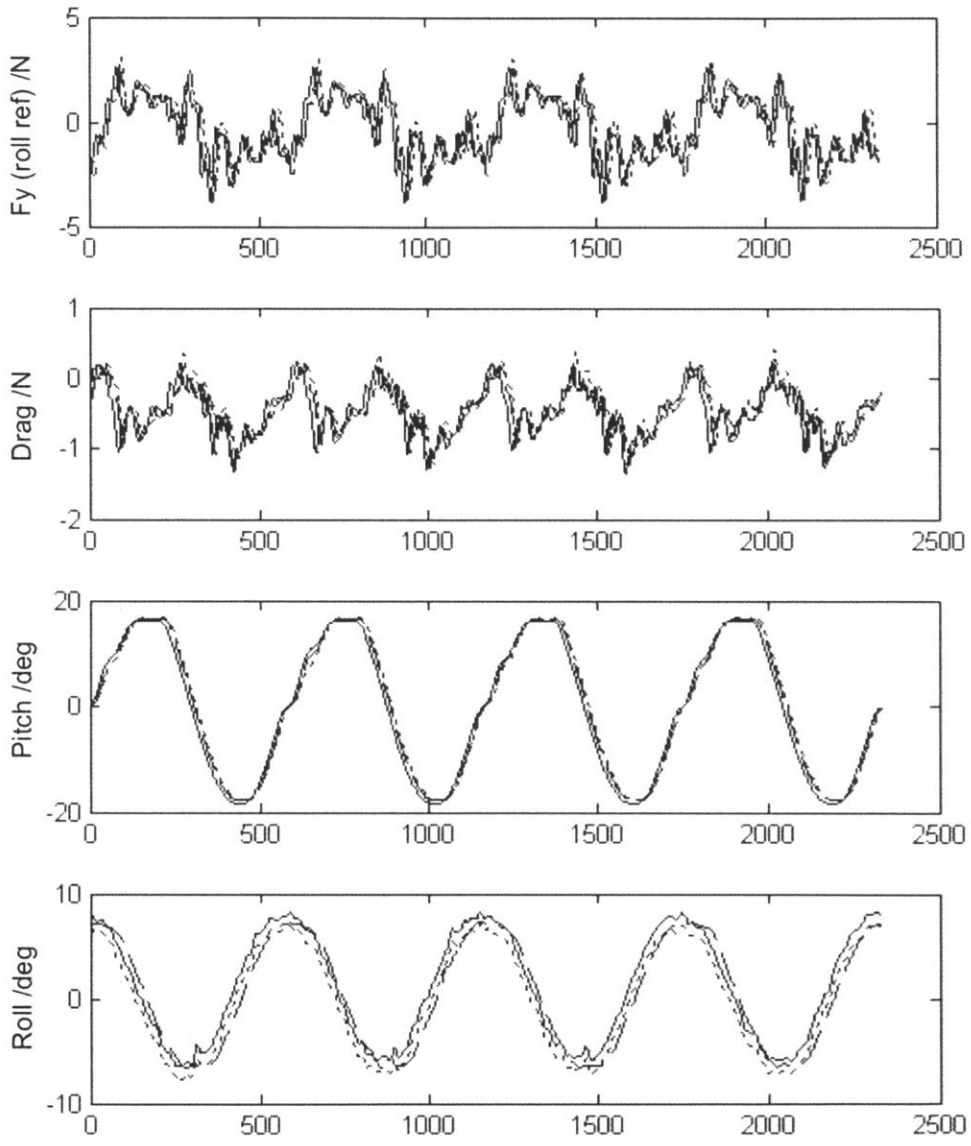

Figure 4-3 : Repeat runs for St = 0.2, $h_{0.7} / c = 1.0$, $\alpha_{max} = 15^0$

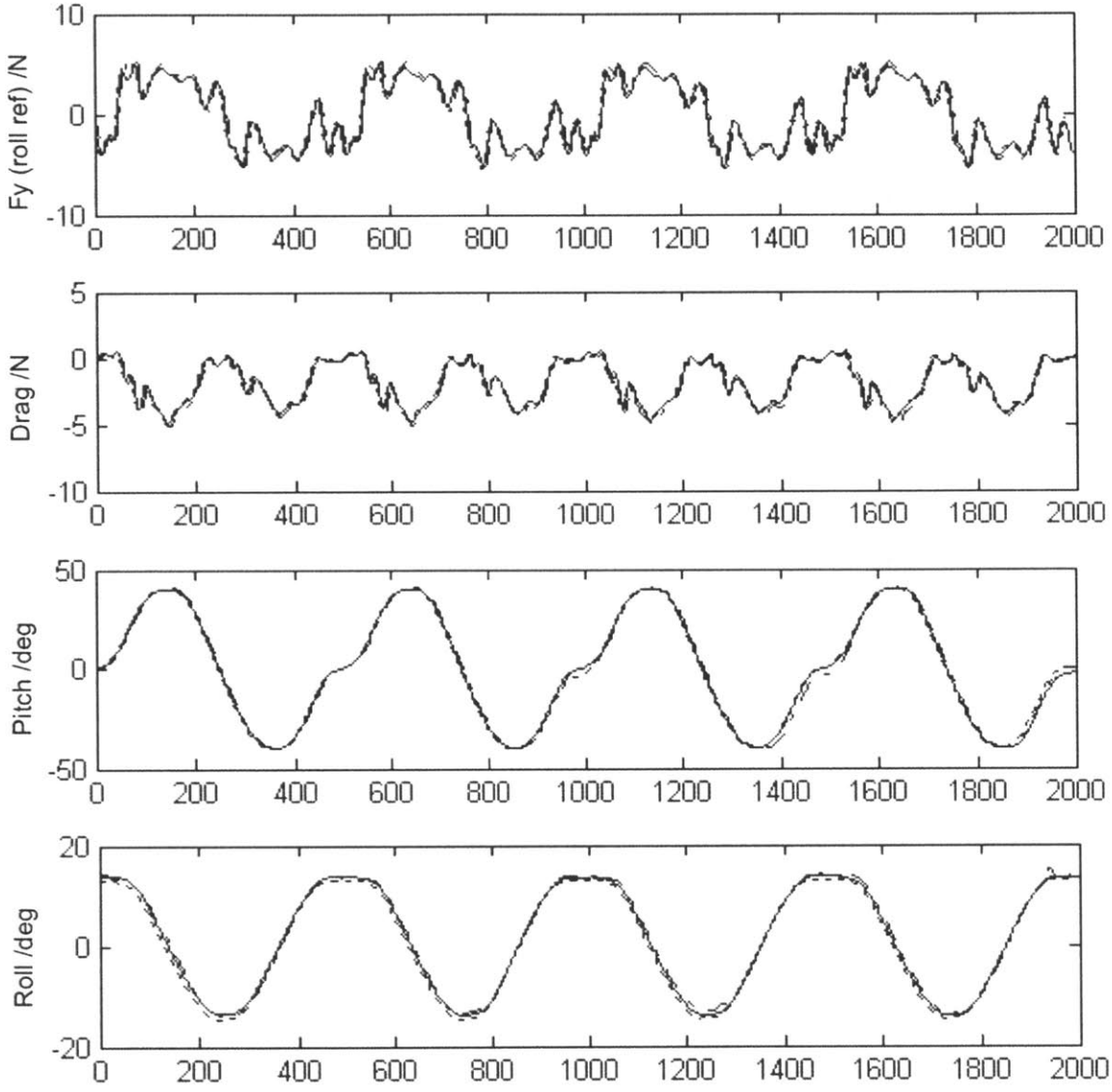

Figure 4-4 : Repeat runs for St = 0.5, $h_{0.7} / c = 2.0$, $\alpha_{max} = 20^0$

Finally, the reflection of the lift force time trace was plotted over itself to check for symmetry. Here, the negative of the lift force was found and shifted by half a period. Ideally, both plots should overlap well with each other, i.e., the lift force should have symmetry about the zero mean. From Figure 4-5, it is evident that there exists some asymmetry. While most of the peaks overlap well, there is an additional peak from the negative plot. This would mean that more negative force lift is generated during the downstroke, resulting in a net lift in the negative direction. Physically, it was observed from the roll and pitch time trace that the motions are not perfect sinusoids. Hence, the asymmetry in the lift force is likely caused by the distortions in the pitch and roll motions as described in the preceding paragraph.

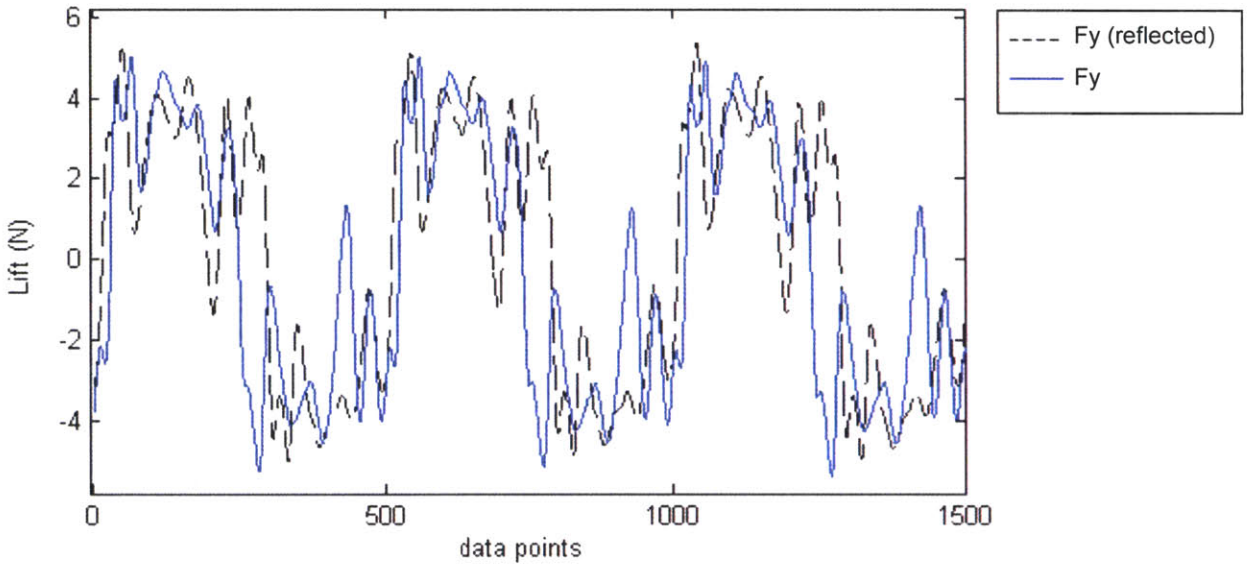

Figure 4-5 : Time trace of lift force to check symmetry

4.5 Summary

Force and efficiency measurements were conducted using the MC1 six-axes sensor for over a range of flow parameters. The sensor proved to be reliable, with force measurements in agreement with those from the tunnel dynamometer (within the useful calibrated range). The results showed a dependency of thrust and efficiency with St and α_{max} values, similar to that obtained by Read, as well as McLetchie, for the two- and three-dimensional cases respectively. For a given Strouhal number, there is a critical α_{max} value beyond which the thrust coefficient will start to decrease. A peak planform area thrust coefficient of 2.09 was measured at $h_{0.7}/c$ = 1.5, St = 0.6 and $\alpha_{max} = 30^0$. Increasing the heave to chord ratio from 1.5 to 2.0 does not appear to improve C_T values. It appears that somewhere between this range is an optimal $h_{0.7}/c$ value for which maximum thrust production can be achieved.

Hydrodynamic efficiency ranged from 0.14 to 0.8. It is noted that for low α_{max} values, thrust generally increases with Strouhal number, without much penalty to efficiency. This would be of much interest to power systems design as an optimal point can be identified for relatively high thrust production with good efficiencies.

The error and repeatability analysis was carried out with four sets of five repeated runs. From the error range, the sensor was found to be exhibiting a precision of about ± 0.044 N. The percentage error, which is taken as the fraction of standard deviation over the mean, is naturally higher at the lower thrust runs (Cases I and III). Likewise a larger percentage error for η arises for Cases I and III. Repeatability was assessed by overlaying the repeated runs over each other. Overall, the overlay plots show good repeatability, with reasonable margins of error as expected from experimental limitations. Some asymmetry in the lift force was observed which can be attributed to distortions in the pitch and roll motions. To reduce percentage errors, it would be advisable for the sensor to be operating near its capacity (550N). Nevertheless, the sensor is able to provide good resolution at the force range measured (0 ~10N), albeit percentage errors of up to 10 %.

Chapter 5

Vortical Signature of Flapping Foil

This chapter presents the results from the flow visualization study using DPIV as implemented digitally by Willert and Gharib [28] as well as Adrian [1]. Four test cases to study the flow signature over both low and high thrust regimes were conducted. The (XY) flow field was captured over two planes of view, one at 0.8 span location and the other at mid-span; providing us with a sense for the three-dimensional effects of the flow. The phased-averaged velocity and vorticity plots at six different foil positions, presented here, will give us a picture of the vortex shedding patterns over the foil and its dependency on the flow parameters. It must be noted that in previous test runs, the flow parameters have been based on the 0.7 span location. These parameters had to be re-computed to give the actual localized flow characteristics over the particular field of view.

5.1 DPIV Methodology

A plane is illuminated using a ND:YAG laser beam fanned to form a planar sheet and the flow is seeded with neutrally buoyant fluorescent particles of diameter 40~70 μm in size. The velocity field measurement then involves the tracking of groups of particles in the flow using digital FFT and cross-correlation routines. A snapshot of the flow field, basically, consists of an image pair of two successive video frames that are captured and stored in levels of grayscale. Each frame was then divided it into smaller interrogation windows at the same spatial position and examined for cross-correlation.

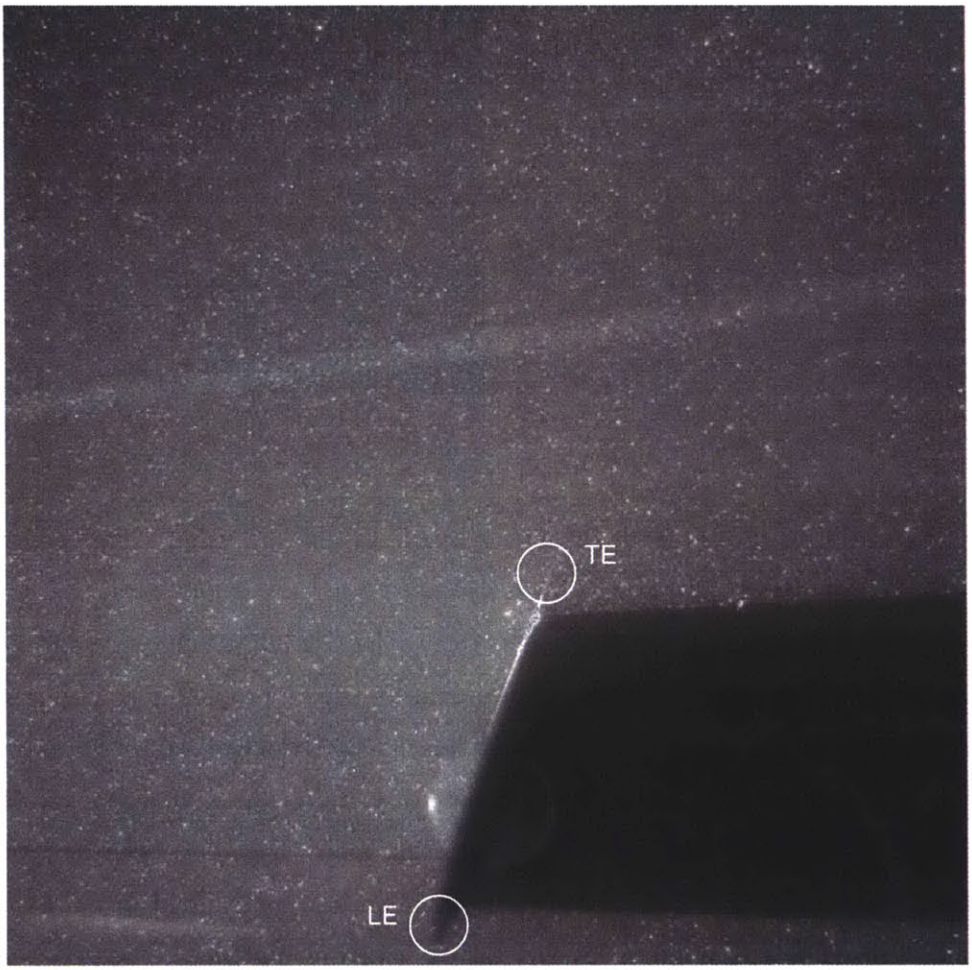

Figure 5-1 : Raw grayscale image of foil in seeded flow. The foil, seen at the bottom, middle portion of the image, is at 0^0 roll and maximum pitch, traversing to the left side of the picture. The leading and trailing edges of the foil are highlighted by the white circles. The right side of the foil is darkened since the laser sheet is blocked by the foil from illuminating that half of the flow. No flow data will be available in this darkened region.

The DPIV algorithm, presented in Figure 5-2, involves the computation of a cross-correlation function. This function, given by Equation 5.1, is calculated using the data from the interrogation windows, $f(m,n)$ and $g(m,n)$, where m, n refer to the individual pixels and N is the size of the interrogation window in pixels :

$$\Phi_{fg} = f(m,n) \circ g(m,n) = \sum_{k=-N/2}^{N/2-1} \sum_{l=-N/2}^{N/2-1} f(k,l)g(k+m,l+n) \tag{5.1}$$

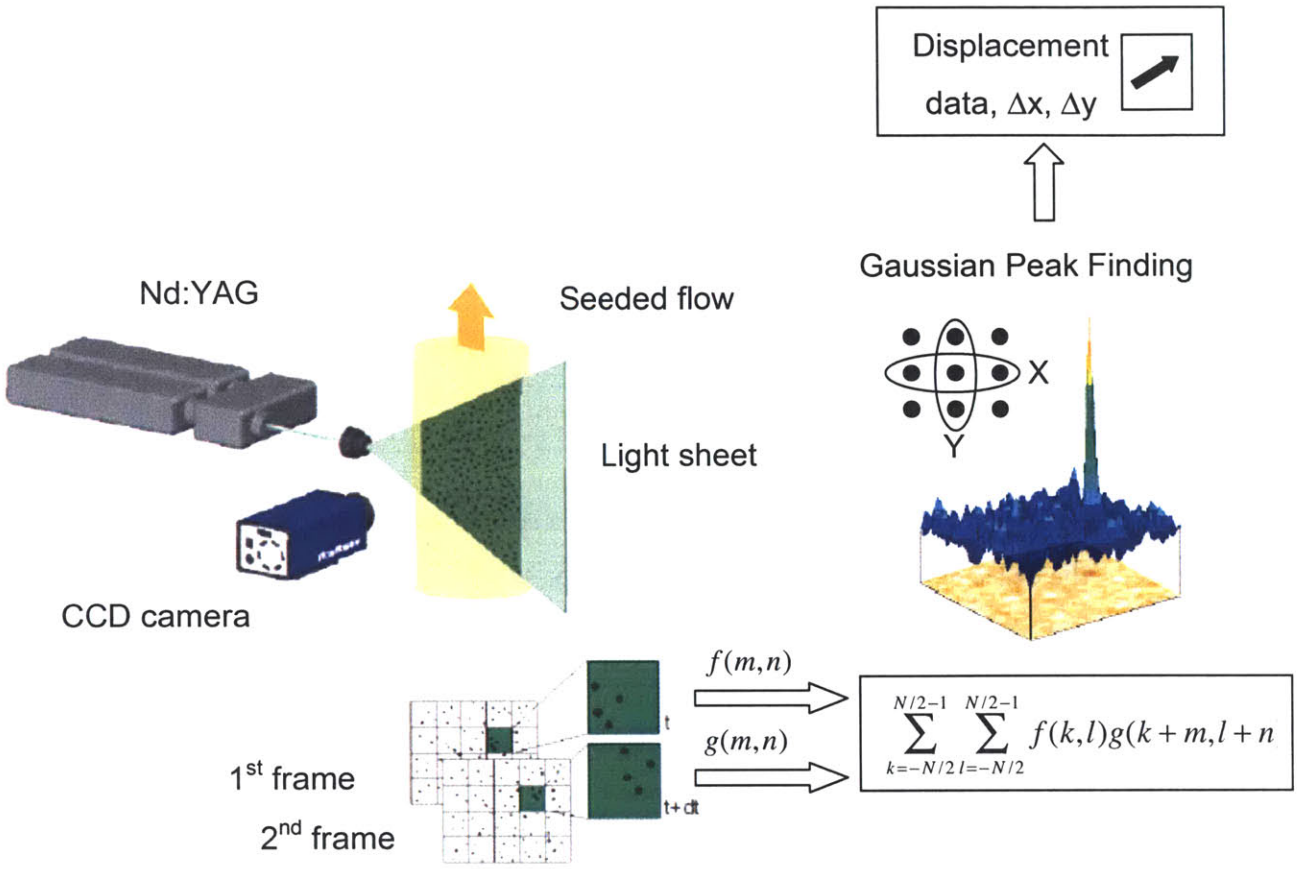

Figure 5-2 : DPIV Algorithm

The cross-correlation function measures how good the match is between the images. A correlation peak provides the average displacement of a sampled group of particles. If the function has a strong narrow peak, the second image matches well when the first image is placed over it at the peak location. This peak is located with sub-pixel accuracy in order to derive displacement data with low relative errors. Here, the algorithm used employs a Gaussian curve fit to the data around the maximum correlation value in both image directions independently.

The Gaussian curve fit takes the form

$$p(\zeta) = c_1 e^{\frac{-(\zeta - c_2)^2}{c_3}} \tag{5.2}$$

This Gaussian curve fit model takes the correlation maximum and four additional points, as indicated in Figure 5-1 by the encircled points, to evaluate the peak location. The Gaussian fit works best when the peak is broad and particle images are larger than a few pixels in size.

5.1.1 Image Processing

The effect of the DPIV windowing processing is that of a spatial low-pass filter. A 40% attenuation of features on the order of 64 pixels is observed for a 32×32 window [28]. For features nearing 160 pixels in size, the attenuation is limited to less than 10%. The objective is to choose an interrogation window size small enough to meet the seeding requirement of 10-20 particles per window and without violating the Nyquist limit – maximum average displacement anywhere in the flow must be less than half the interrogation window size. Here, images are post-processed using a two-pass interrogation with constant window sizing for each iteration. Both the first and final iteration has interrogation window sizes of 32×32; a 50% overlap of the final window is applied with grid spacing of 16 pixels to increase the spatial resolution of the data. The plots are averaged over 5 to 12 sets of image pairs.

A median filter is applied to remove outliers. Outliers are identified by comparing the displacement magnitude at a point with that from eight nearest neighboring point. If the value is more than 2 RMS of its neighbors, that point is re-interpolated using linear interpolation with the neighboring points. The corrected data are then filtered by replacing each data point with a weighted average of the data point and its neighbors. A smoothing filter is also applied to remove high frequency jitter inherent to the algorithm as well as possible without biasing the data when only a few data points are missing.

5.1.2 Velocity Vectors and Vorticity

The location of the cross correlation peak gives the displacement of the center of particle groups in an interrogation window. The velocity is then the displacement divided by the time, Δt, between exposures. Both horizontal and vertical velocity components, u and v are computed.

In two dimensions, the out of plane vorticity is given by

$$\omega_z = \frac{\partial v}{\partial x} - \frac{\partial u}{\partial y} \tag{5.3}$$

Instead of direct differentiation, Stoke's Law is applied to compute vorticity using contour integration. Circulation is given by

$$\Gamma = \oint \vec{u}(x,y) \cdot \vec{dl} \tag{5.4}$$

where $\vec{dl}$ is a segment of the closed contour. Or in discretized form

$$\Gamma_{ij} = (u_{i-1,j-1} + 2u_{i-1,j} + u_{i-1,j+1})\frac{\delta x}{2} + (v_{i-1,j+1} + 2v_{i,j+1} + v_{i+1,j+1})\frac{\delta y}{2}$$

$$-(u_{i+1,j+1} + 2u_{i+1,j} + u_{i+1,j-1})\frac{\delta x}{2} - (v_{i+1,j-1} + 2v_{i,j-1} + v_{i-1,j-1})\frac{\delta y}{2} \tag{5.5}$$

If A is the area enclosed by the contour of integration, the vorticity is then computed as

$$\omega_z = \frac{\Gamma}{A} \tag{5.6}$$

or

$$\omega_{ij} = \frac{\Gamma_{ij}}{4\delta x \delta y} \tag{5.7}$$

5.2 Test Cases

A total of four experimental points were examined with DPIV, at two different planes of view, demarcated by the foil span positions. The first view plane was captured at mid-span, with local chord length, $c_{0.5}$ = 58.7 mm. The other was at 0.8 span ($c_{0.8}$ = 43.6 mm). The experimental points were chosen to examine effects of St and α_{max} on the wake structure formation. It is also an attempt to capture the flow at different regimes of low or high thrust/efficiencies.

Test Case	Flow Parameters*	Rationale
1	St = 0.2, $h_{0.7}/c$ = 1.5, $\alpha_{max} = 15^0$	Low thrust, high efficiency regime
2	St = 0.2, $h_{0.7}/c$ = 1.5, $\alpha_{max} = 25^0$	Examine effect of increasing α_{max}
3	St = 0.5, $h_{0.7}/c$ = 1.5, $\alpha_{max} = 25^0$	Examine effect of increasing St frequency
4	St = 0.5, $h_{0.7}/c$ = 2.0, $\alpha_{max} = 20^0$	High thrust, efficiency regime

*based on 0.7 span location

Table 5-1 : DPIV test cases to examine effects of St and α_{max} on wake formation.

5.2.1 Localized Flow Parameters

To have an appreciation for the expected wake patterns from the experiments, the experimental points were mapped against the vortex pattern map (as shown in Figure 5-3) developed by Anderson [2] for the two-dimensional flapping foil case. This plot maps how the wake vortical patterns vary with the flow parameters. Since the foil used in our experiment is three-dimensional (non-uniform tapering geometry) the patterns could vary along the span. Thus the equivalent two-dimensional flow parameters at mid- and 0.8 span locations were considered. These localized parameters are presented in Table 5-2.

Case		Span Location	St	α_{max}	C_T	η	Legend
1	(a)	0.5	0.18	12.1^0	0.24 (low)	0.803 (high)	
	(b)	0.8	0.21	16.3^0			
2	(a)	0.5	0.18	22.1^0	0.18 (low)	0.378 (low)	
	(b)	0.8	0.21	26.3^0			
3	(a)	0.5	0.44	21.7^0	1.37 (medium)	0.507 (medium)	
	(b)	0.8	0.52	26.3^0			
4	(a)	0.5	0.45	16.8^0	1.18 (medium)	0.62 (high)	
	(b)	0.8	0.53	21.5^0			

Table 5-2 : Localized flow parameters at mid- and 0.8 span locations. The colored markers in the last column are used in Figure 5-3 to indicate the test regimes. C_T and η are recorded values from Chapter 4. Qualitatively, the measured values were benchmarked against the maximum and referenced as low, medium or high.

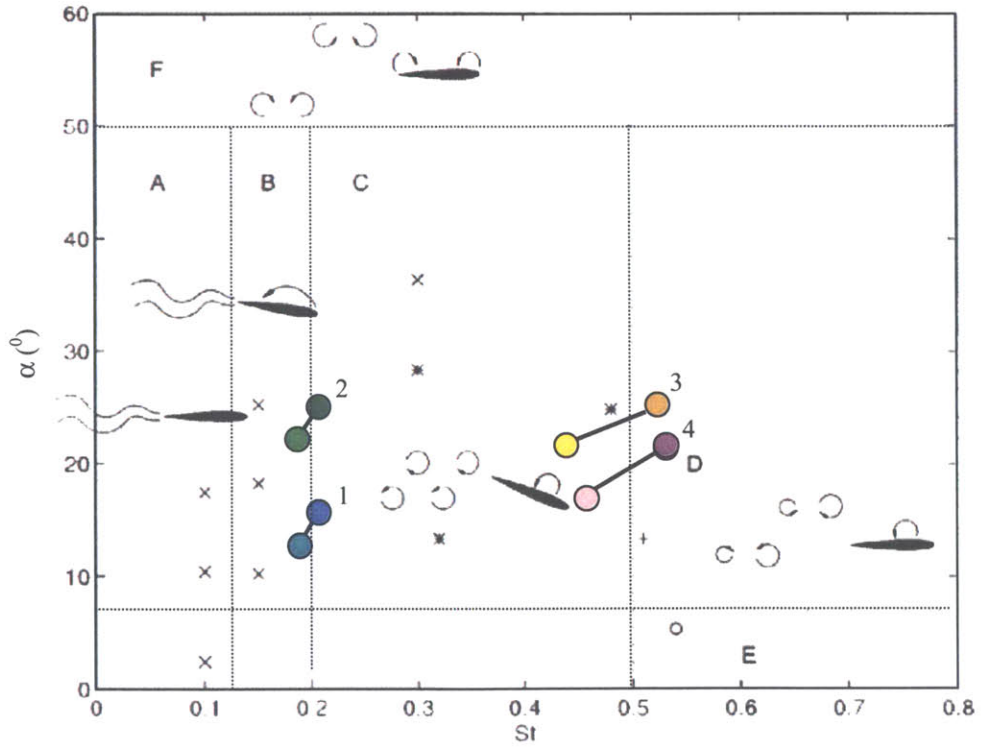

Figure 5-3 : Mapping of experimental points on 2D vortex pattern map by Anderson [2].

5.3 Anderson's Vortex Pattern Map

Anderson created a vortex pattern map depicting the patterns formed in a two-dimensional flapping foil on a plot of Strouhal number against angle of attack. She demarcated six different wake regions in this map as follows :

A. A loosely organized Karman street along the path of the trailing edge.

B. A Karman steet forms as in A, but in addition, a sluggishly organized leading edge vortex is evident, even at low angles of attack.

C. Two leading edge vortices are shed per cycle forming a jet wake.

D. Four vortices are shed per cycle, two originating from the leading edge and two from the trailing edge.

E. Four vortices are shed which all originate from the trailing edge.

F. The 'piston mode' shedding characterized by very high angle of attack. A mixed wake is produced by shedding from both edges.

Anderson concluded that the shape of the angle of attack profile significantly influenced the wake structure. This profile is generally harmonic but flattens out as Strouhal number is increased. Sinusoids and square wave profiles produced the clearest wakes. She also observed that multiple peaks in the angle of attack profile at high Strouhal number caused additional shedding that mixes the wake.

5.4 DPIV Results

Three different types of wake patterns are observed and presented in the following sections. At low Strouhal numbers and α_{max}, shear layer vortices are seen. At higher Strouhal numbers, vortices are seen being shed into the wake either singly or in pairs. The LE vortex either merges with the TE vortex and convects downstream as a single vortex or in some cases, mixed pairs of opposite sign exist to produce strong thrust.

In this thesis, the nomenclature being used by Williamson & Roshko [29] to describe vortex shedding for oscillating cylinders is adopted. They observed two distinct patterns of shedding, the '2S' and '2P' patterns. In the context of a flapping foil, the '2S' pattern consists of a single TE vortex being shed per half cycle, as shown in Figure 5-4(a). This pattern corresponds to Region C of Anderson's wake pattern map. The '2P' pattern consists of a pair of vortices with opposite signs being shed per half cycle, as seen in Region D of the wake pattern map. Each pair of vortices convects downstream and laterally outwards from the centerline of oscillation.

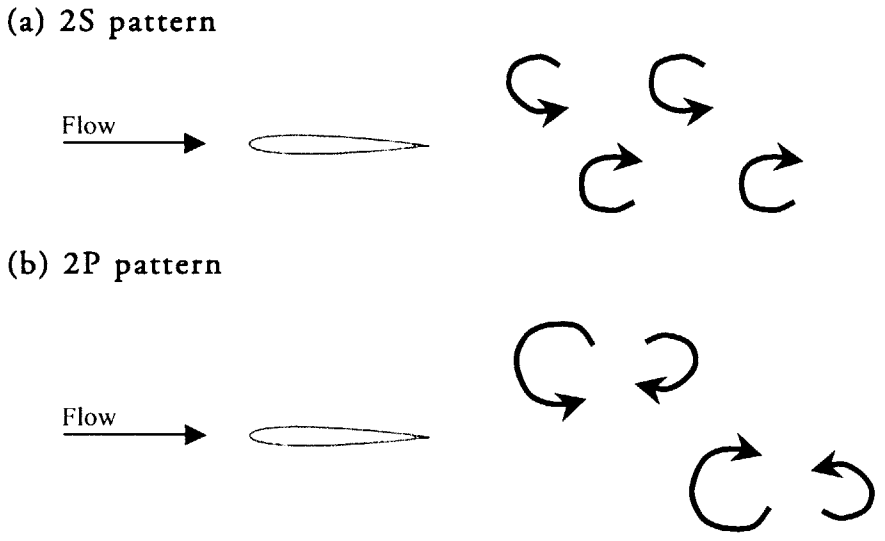

Figure 5-4 : Sketch of the two predominant shedding patterns

The DPIV results for Cases 1(a) to 4(b) are shown in Figures 5-5 to 5-12. The foil is shown at different stages of the flapping cycle. The vorticity plots show the phase average results using between 5 to 12 pairs of image data.

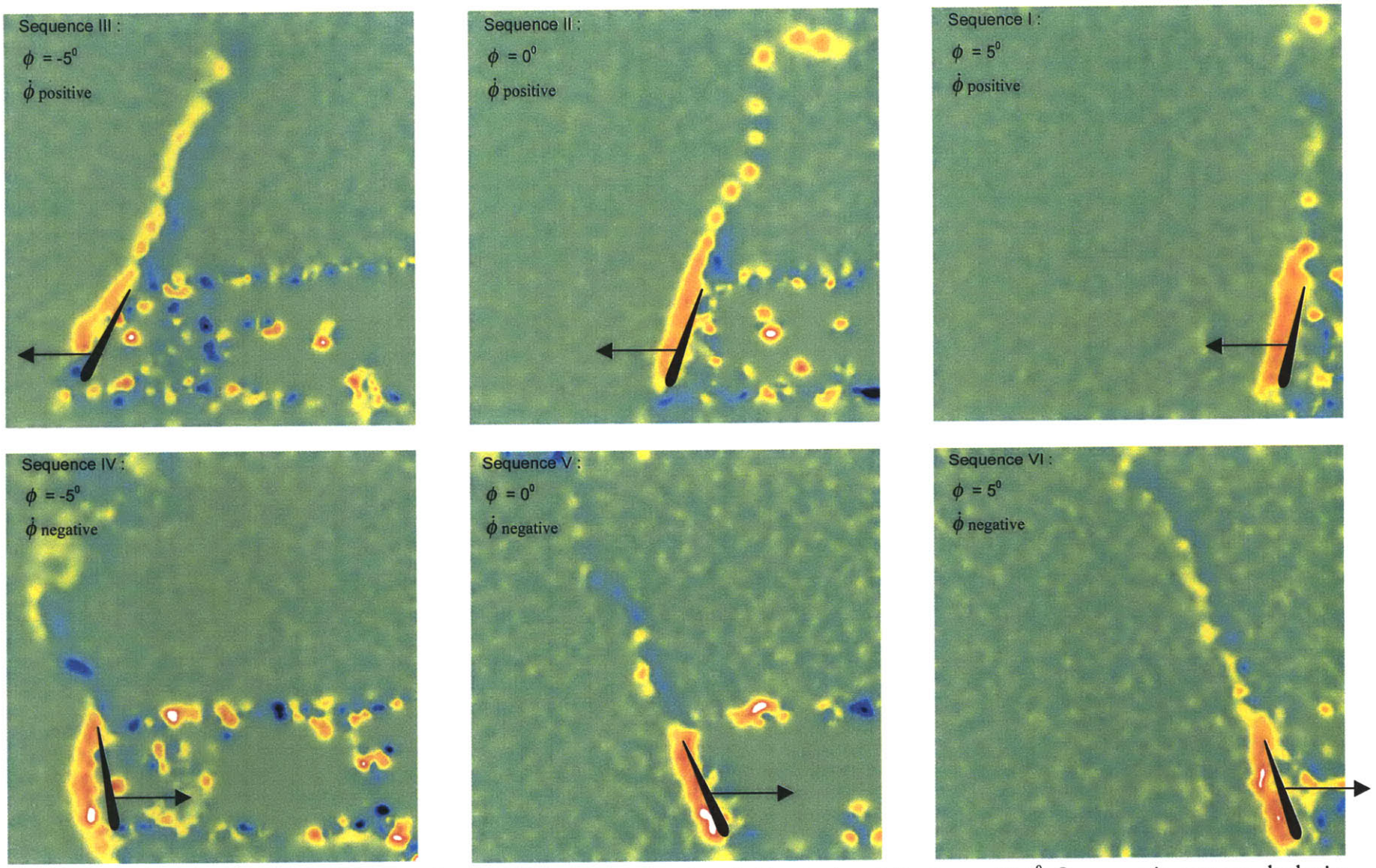

Figure 5-5 : Case 1(a) – Vorticity plots for flapping foil over 1 cycle, St = 0.18, $\mathscr{A}_{0.7} / c$ = 1.5, α_{max} = 12.1°. Sequence is counter-clockwise, starting from top right ending in bottom right. The superimposed foil is only indicative of actual position and size. A positive vortex is denoted as a blue patch (out of page) and conversely, a negative vortex as a red patch (into page).

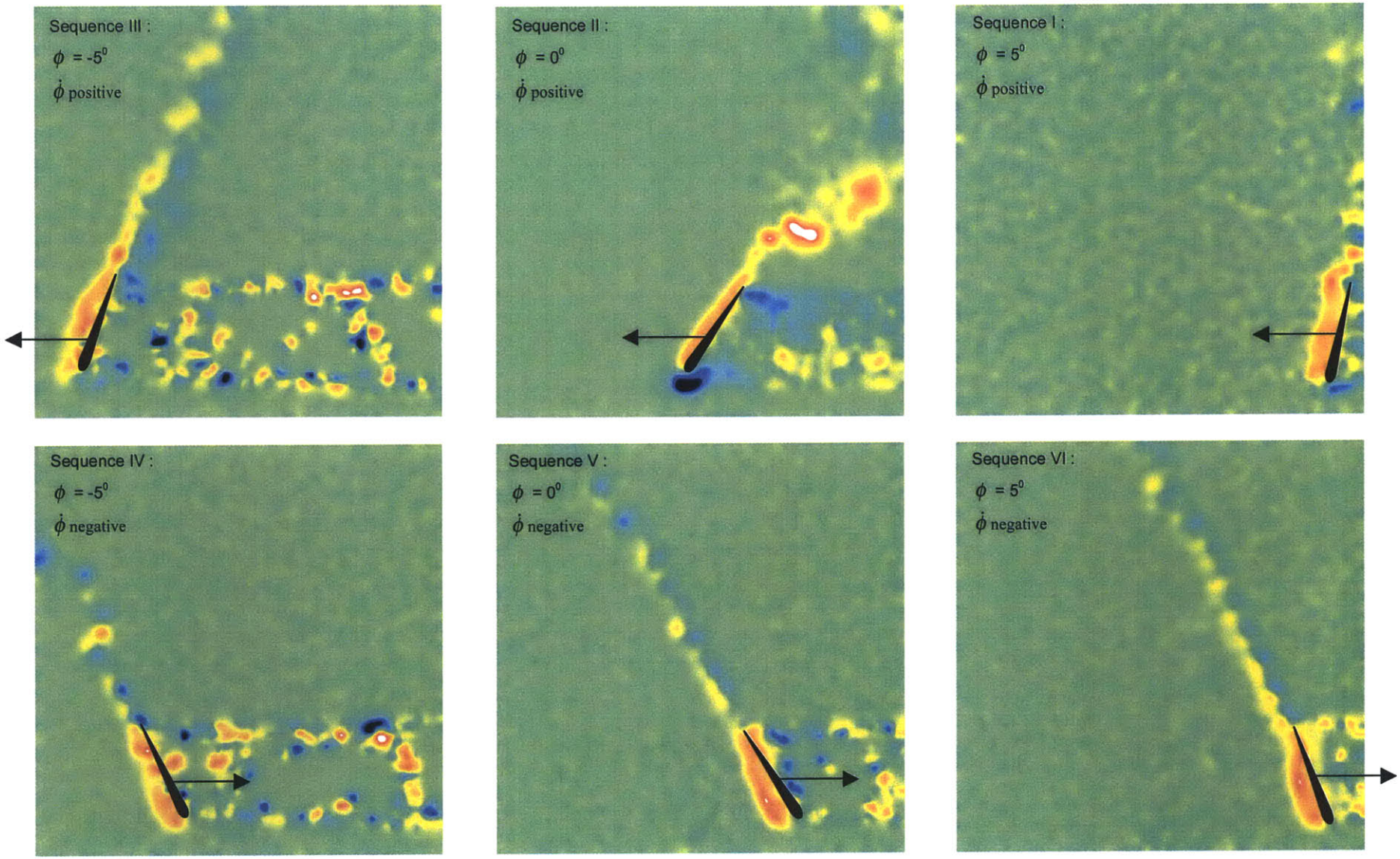

Figure 5-6 : Case 1(b) – Vorticity plots for flapping foil over 1 cycle, St = 0.21, $\mathcal{A}_{0.7} / c$ = 1.5, α_{max} = 16.3°. Sequence is counter-clockwise, starting from top right ending in bottom right.

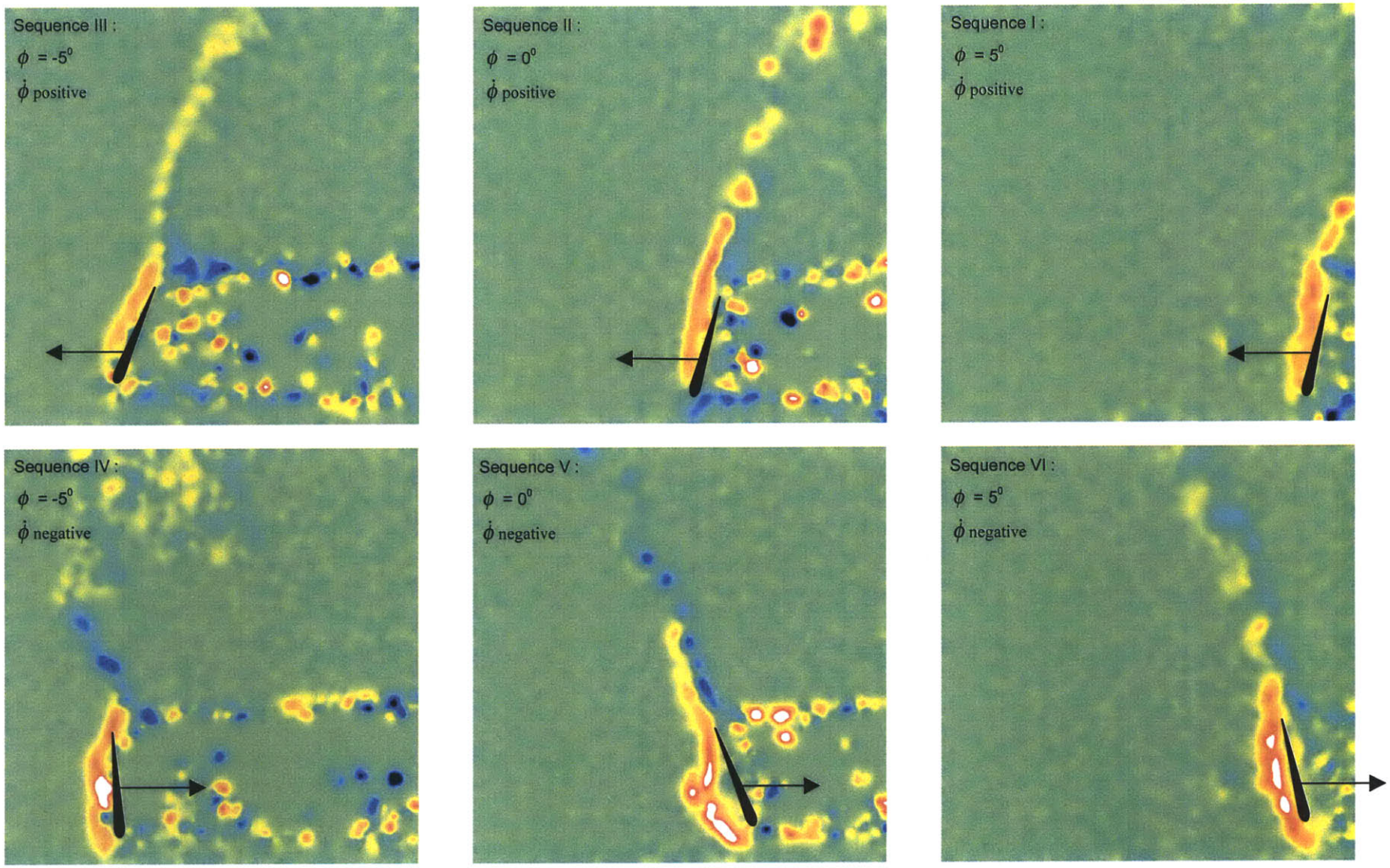

Figure 5-7 : Case 2(a) – Vorticity plots for flapping foil over 1 cycle, St = 0.18, $\mathscr{A}_{0.7} / c$ = 1.5, α_{max} = 22.1°. Sequence is counter-clockwise, starting from top right ending in bottom right.

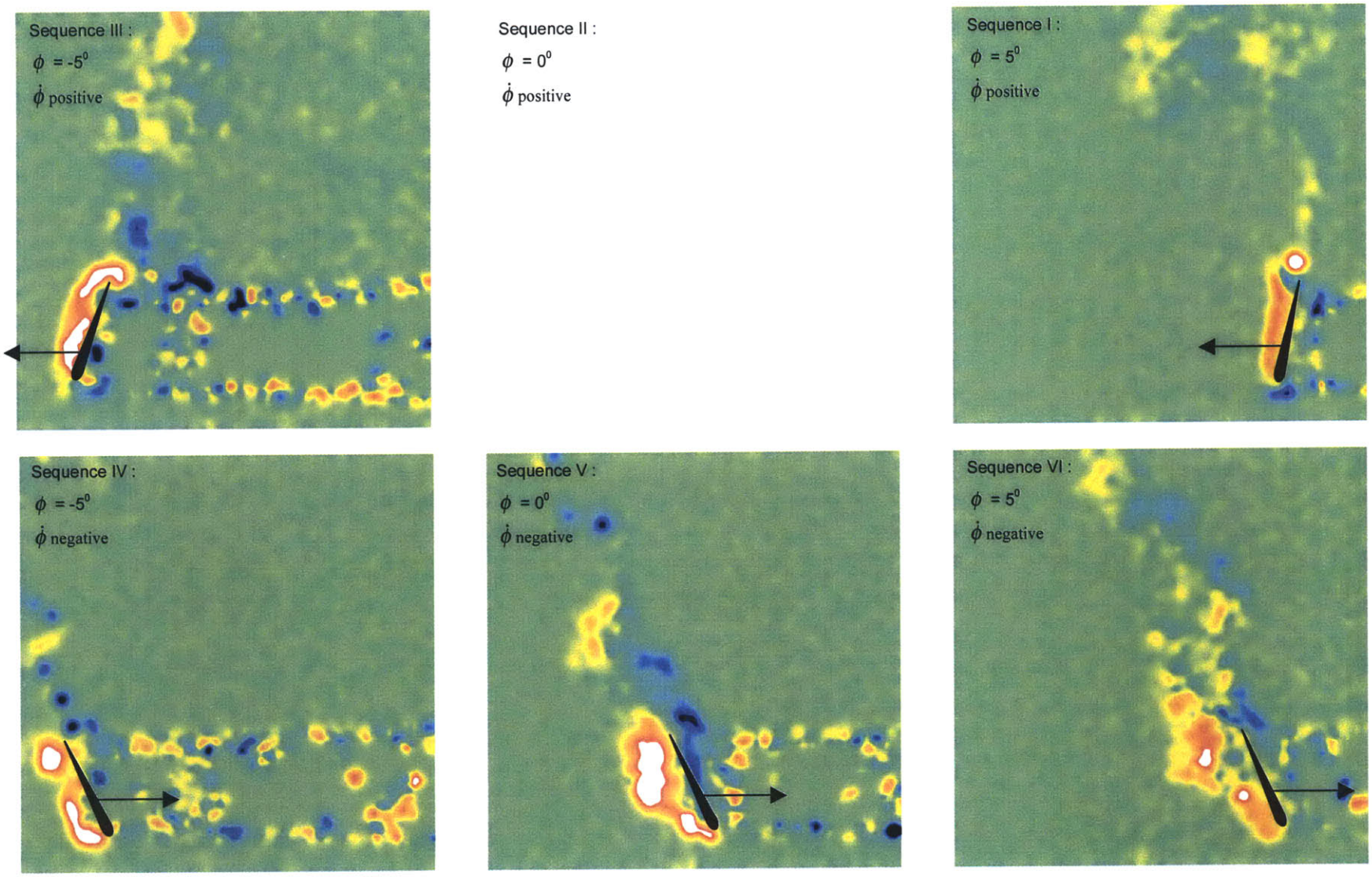

Figure 5-8 : Case 2(b) – Vorticity plots for flapping foil over 1 cycle, St = 0.21, $\mathcal{A}_{0.7} / c = 1.5$, $\alpha_{max} = 26.3^0$. Sequence is counter-clockwise, starting from top right ending in bottom right. The image for Sequence II was not available.

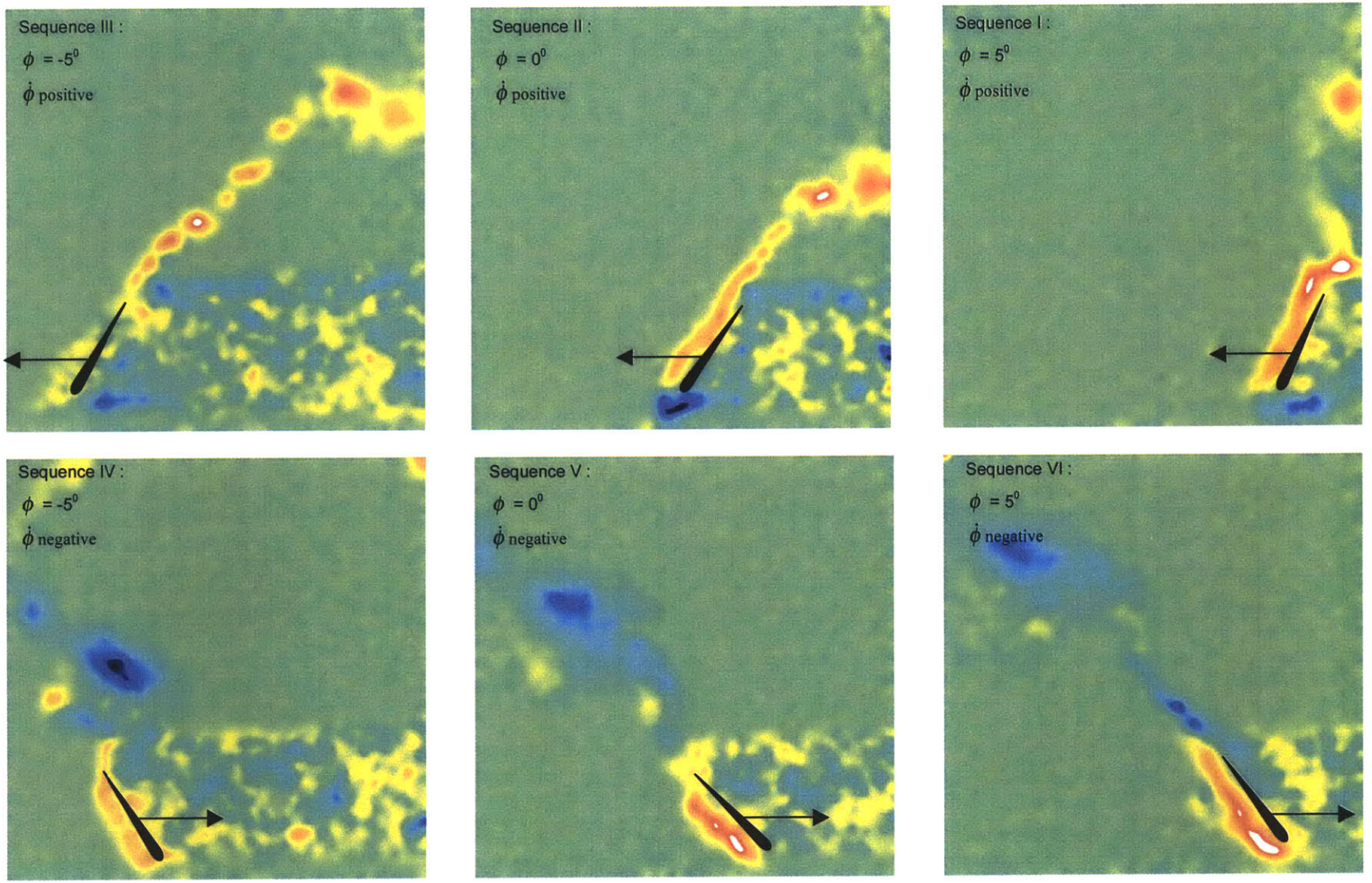

Figure 5-9 : Case 3(a) – Vorticity plots for flapping foil over 1 cycle, St = 0.44, $\mathscr{A}_{0.7} / c = 1.5$, $\alpha_{max} = 21.7^0$. Sequence is counter-clockwise, starting from top right ending in bottom right.

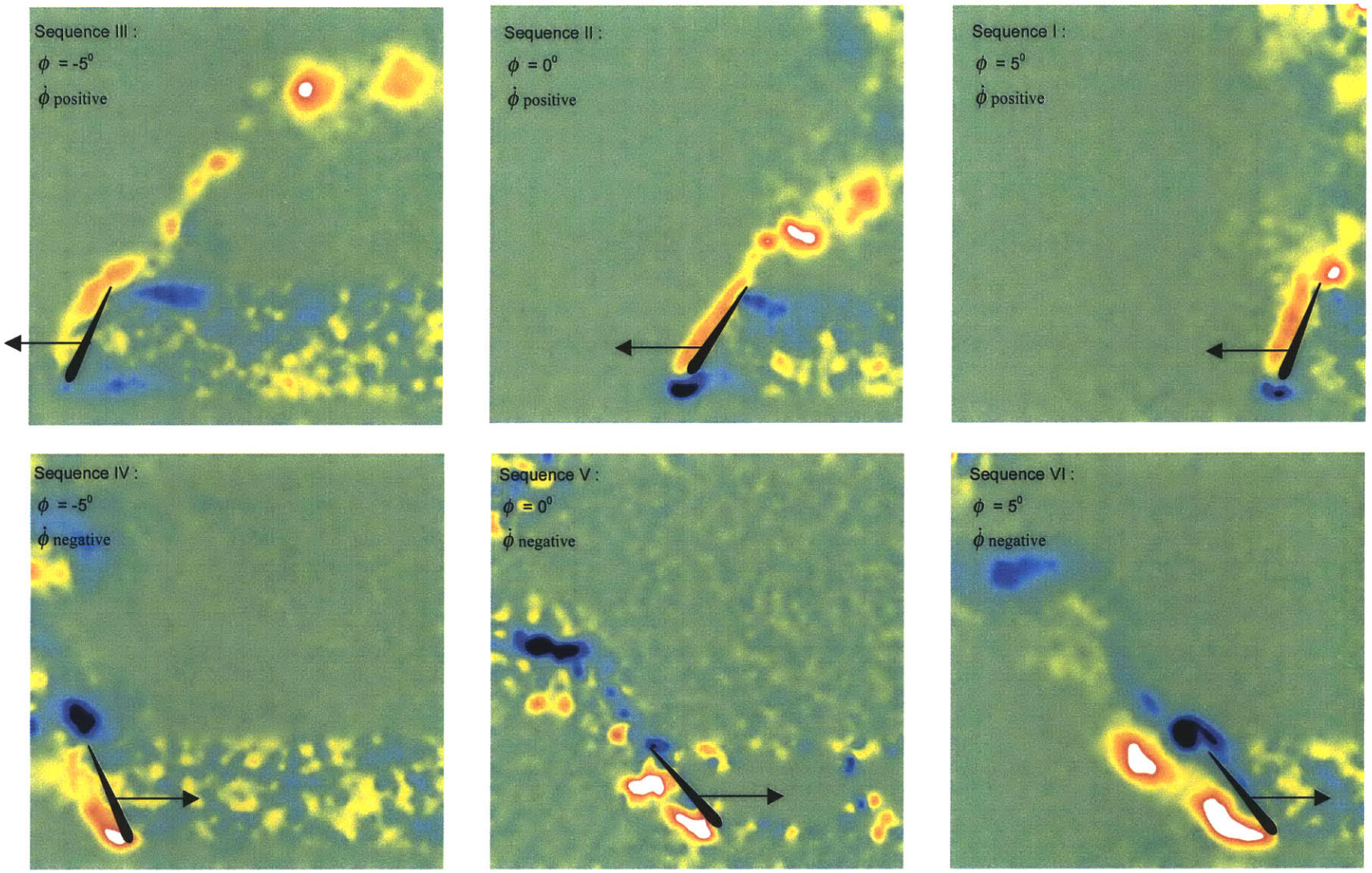

Figure 5-10 : Case 3(b) – Vorticity plots for flapping foil over 1 cycle, St = 0.52, $\mathcal{A}_{0.7} / c = 1.5$, $\alpha_{max} = 26.3^0$. Sequence is counter-clockwise, starting from top right ending in bottom right.

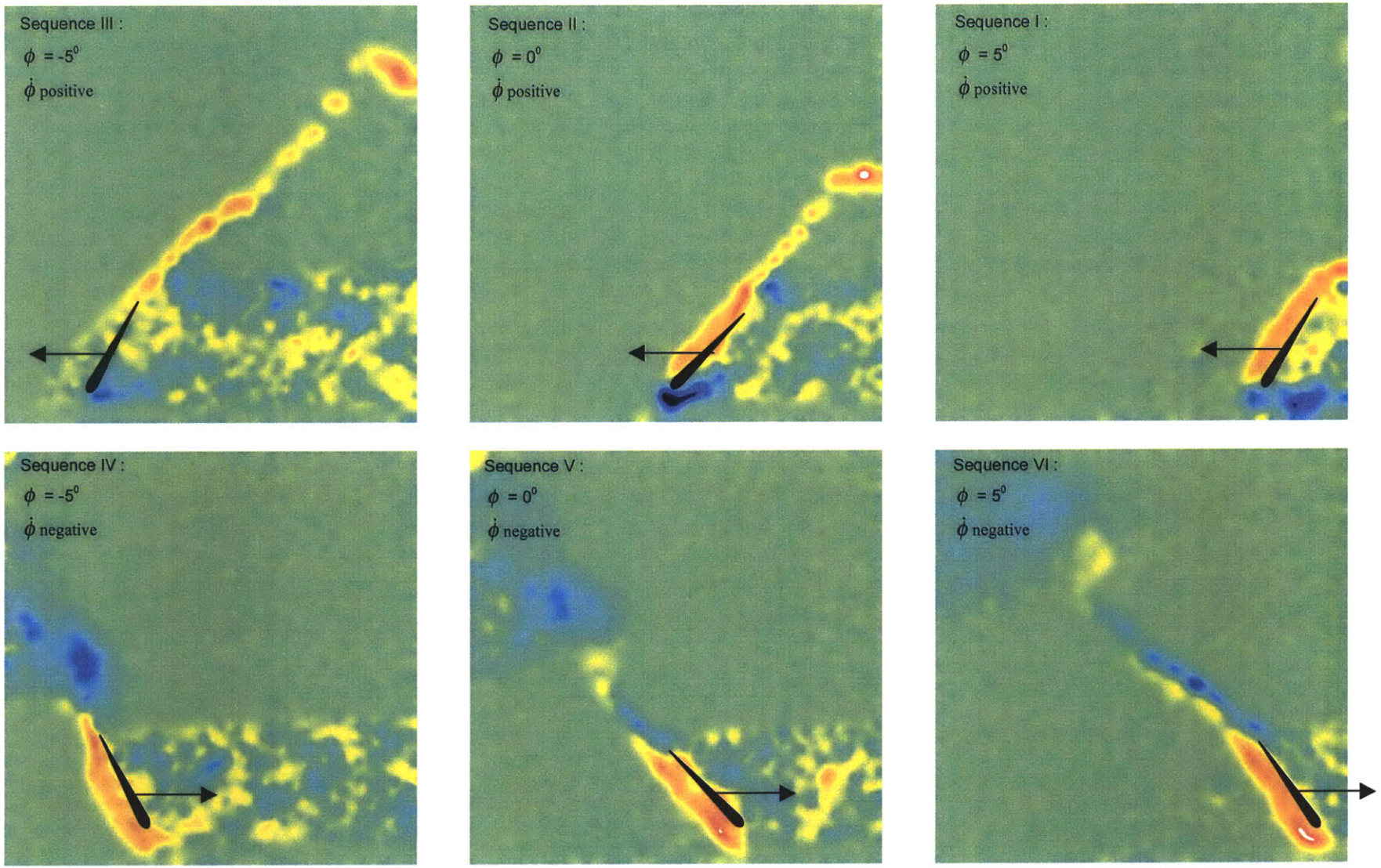

Figure 5-11 : Case 4(a) – Vorticity plots for flapping foil over 1 cycle, St = 0.45, $\hat{A}_{0.7} / c = 2.0$, $\alpha_{max} = 16.8^0$. Sequence is counter-clockwise, starting from top right ending in bottom right.

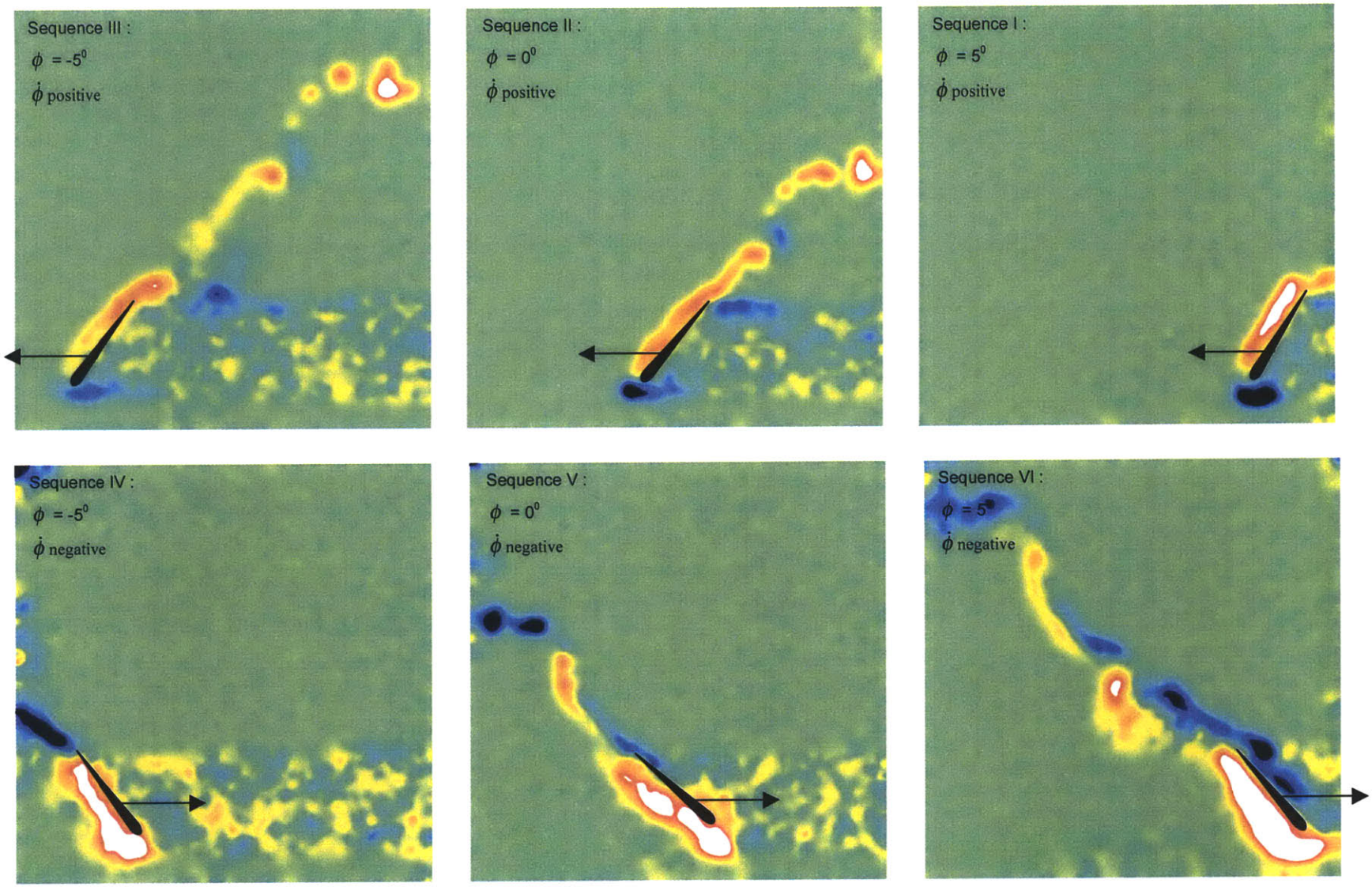

Figure 5-12 : Case 4(b) – Vorticity plots for flapping foil over 1 cycle, St = 0.53, $\ell_{0.7} / c = 2.0$, $\alpha_{max} = 21.5^0$. Sequence is counter-clockwise, starting from top right ending in bottom right.

5.4.1 Shear Layer Vortices

For Cases 1 and 2 where the thrust production is low, only shear layer vortices were visible. The images (as seen in Figures 5-5 to 5-8) showed no evidence of distinct 2P or 2S shedding patterns. The wake pattern is typically characterized by that shown in Figure 5-13 below. The plots show a trail of shear layer vortices, forming a weakly mixed Karman street along the foil path, with strong LE separation. The plots for Case 1(a) show similar patterns. From the wake momentum, it is also not evident that strong thrust is produced.

In Anderson's experiments for the 2D foil, she characterized the wake pattern as one comprising of a Karman street with a sluggishly organized LE vortex (Region B, as shown in Figure 5-3). The vorticity plots show agreement with her observations. Although the flow parameters for the lower half of the foil (0.8S, Cases 1(b) and 2(b)) falls in Region C ("2S" pattern), the vortex pattern seen at 0.5S (Cases 1(a) and 2(a)) dominates along the span instead. It would appear that there is strong continuity in the shear layer vortex shedding over the entire span of the tapered foil with none of the 2P pattern forming at 0.8S and beyond. It is noted that the foil has a low aspect ratio and minimal taper, which seemed to have little effect on inducing two distinct wake patterns.

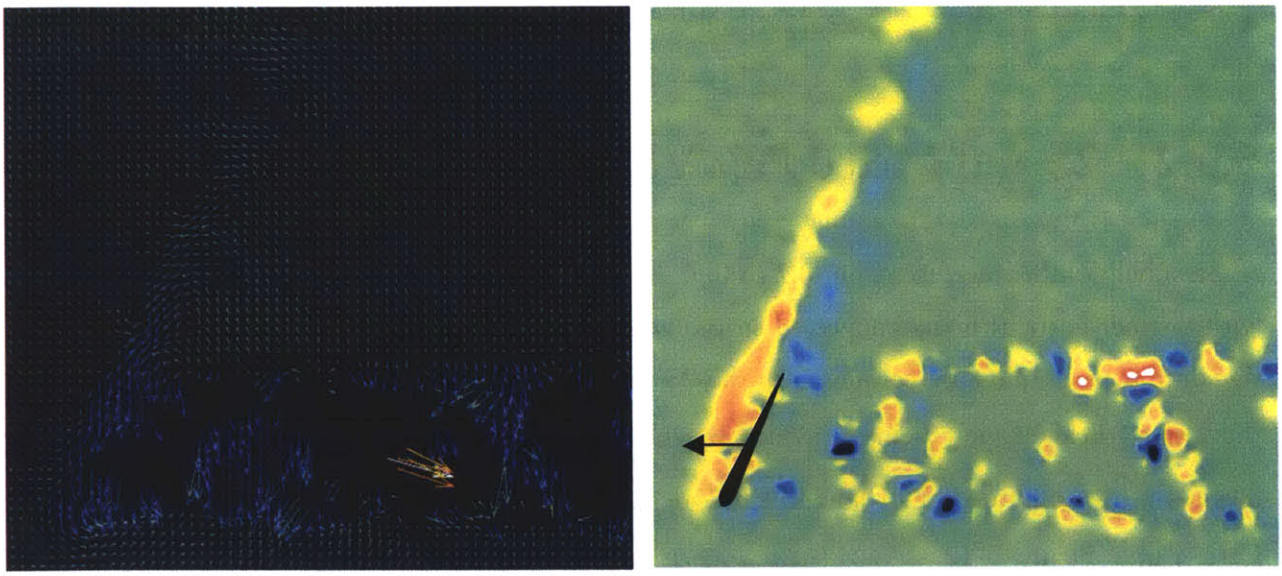

Figure 5-13 : Velocity and vorticity plots at St = 0.21, $h_{0.7} / c$ = 1.5, α_{max} = 16.3^0. Sequence III of Case 1(b). Foil is at -4^0 roll, traversing to the left. Vectors shown are relative to the average flow velocity.

Cases 1 and 2 were compared to see the effect of increasing α_{max} . At the higher angle of attack (Case 2), the LE separation seems to be more pronounced. In Figure 5-14, a LE vortex is seen rolling up along the foil and shedding from the TE just as the foil is about to change direction at zero pitch angle.

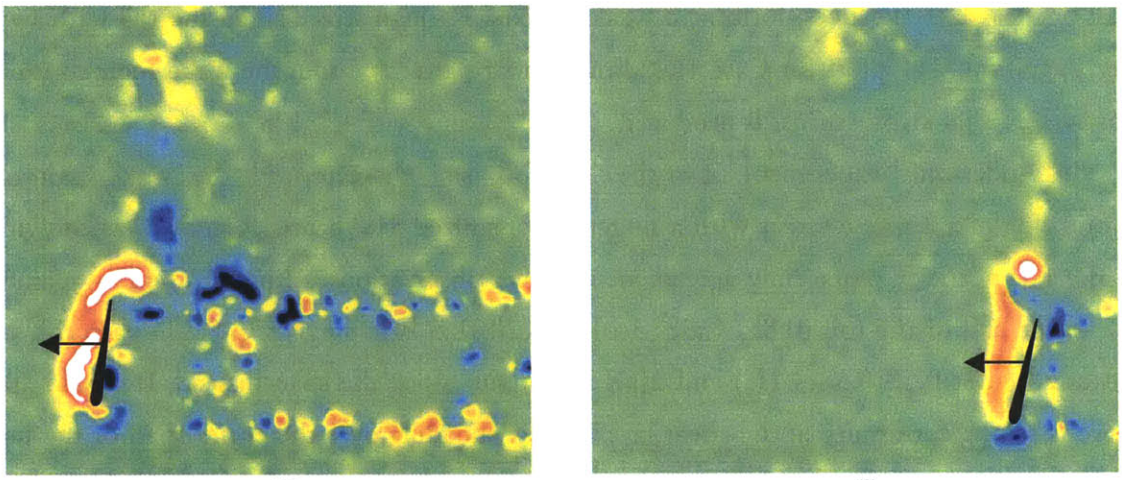

Figure 5-14 : Vorticity plots for flapping foil showing LE separation at St = 0.21, $h_{0.7}/c$ = 1.5, α_{max} = 26.3^0. In (I), the foil is at 5 deg roll, travelling to the left. In (II) the foil is at -5 deg roll, and almost reaching 0 deg pitch.

5.4.2 2S and Mixed Pair Vortex Shedding

As Strouhal number increases from 0.2 to 0.5, the vortex shedding is observed to be more energized with distinct vortices being convected in the wake (as seen in Figures 5-9 to 5-12). The vortical signature is predominantly composed of the 2S pattern, although this is not easily discernible from the limited field of view being provided by the images (view plane of up to ±5 deg roll versus maximum roll amplitude of ±10.3 and ±13.7 deg). Vorticity plots from Case 3(b) : Figure 5-10 and Case 4(b) : Figure 5-12 show little evidence of the 2P pattern as suggested by Region D of Anderson's vortex pattern map. Considering the linear taper of the foil, it is noted that the main upper portion of the foil, by virtue of geometry, falls within Region C, while only the lower quarter (0.7S and beyond) falls in Region D based on its equivalent two-dimensional flow parameters. By

material continuity and slow changes in geometry (as mentioned in the preceding section), the 2S pattern overwhelms the wake region. It is less likely for the vortex formation along the span to have two distinct shedding patterns. The mixed vortex pair observed at the 0.8S might be due to the tip vortex rolling upwards and interacting with the TE vortex. However, the limited field data collected renders it difficult to determine whether this vortex pair is indeed composed of both LE and TE vortices (as defined by the 2P pattern) or a pairing up of the tip vortex with the TE vortex. Nevertheless, the plots seem to suggest highly three-dimensional effects and more detailed investigation of this tip region is necessary to fully understand the wake structure beyond 0.7S .

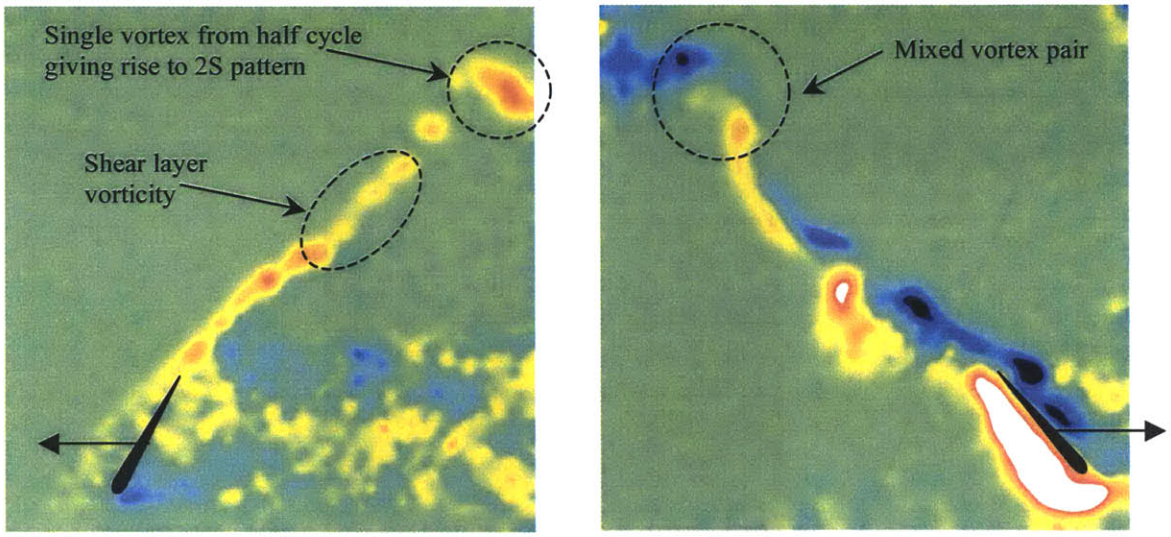

(A) 2S pattern (B) Mixed vortex pair of opposite signs

Figure 5-15 : Vorticity plots showing examples of 2S and mixed vortex shedding patterns. Image (A) is taken from sequence III of Case 4(a) : Figure 5-11 and image (B), from sequence VI of Case 4(b) : Figure 5-12.

A further look at the velocity vector plot of the mixed pair from Case 4(b) : Figure 5-12 shows strong vectors being produced at an oblique angle to the flow direction. It is interesting to note that this case yielded good values of C_T and η. From basic momentum analysis, the existence of this velocity jet in the wake gives rise to thrust. Kinetic energy being imparted to the flow naturally translates to power losses. However, the large thrust force produced by the large roll motion does seem to recover some of the loss with high efficiencies being recorded. Figure 5-16 shows the velocity vector and vorticity plots from Sequence V of this case.

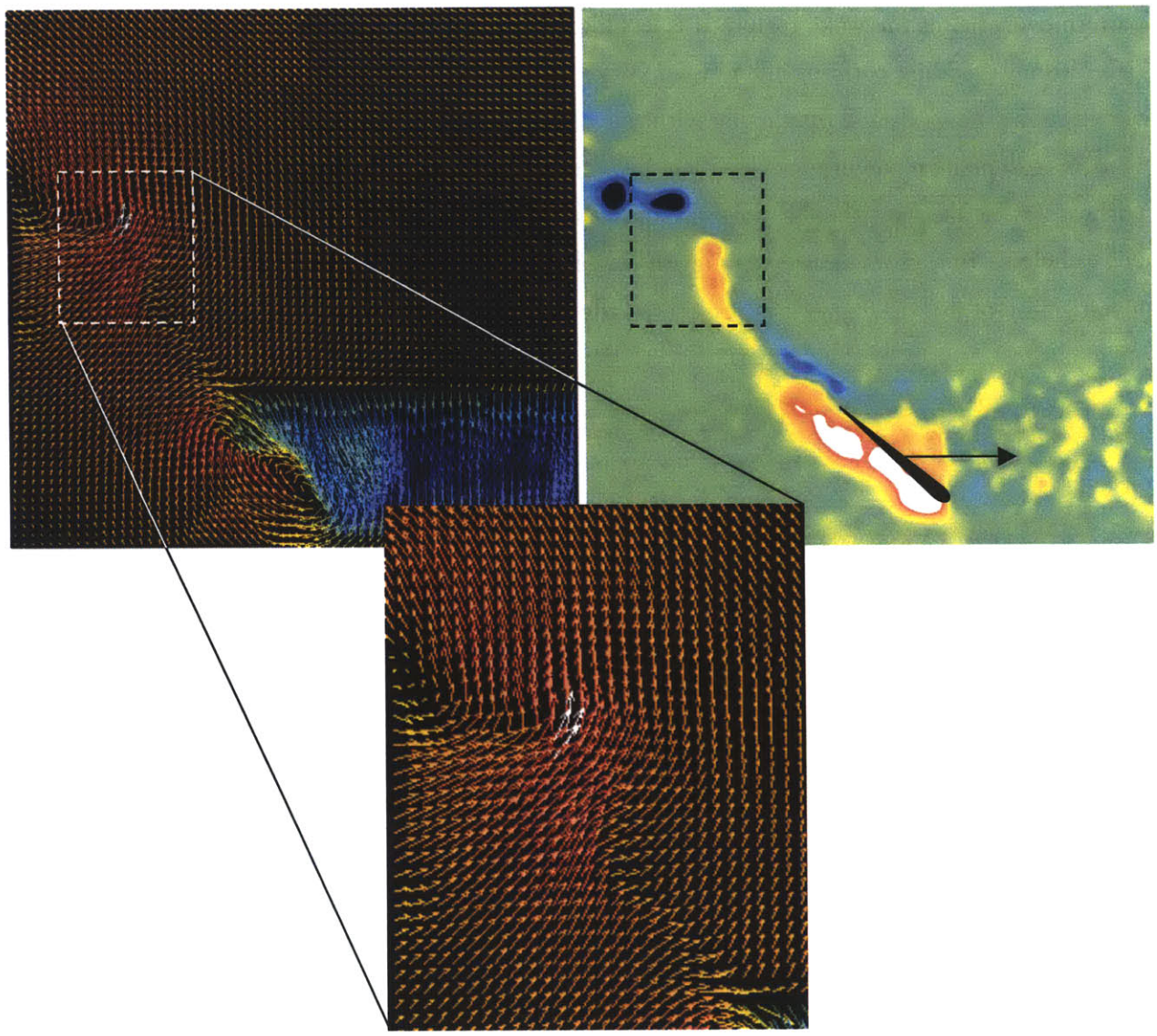

Figure 5-16 : Velocity vector and vorticity plots showing mixed vortex pair imparting momentum into wake. Flow parameters are St = 0.53, $h_{0.7} / c = 2.0$, $\alpha_{max} = 21.5^0$.

The vortex pattern is slightly different from the case presented by Anderson in Region D. Here the jet formed by the vortex pair is angled inwards toward the centreline and aft. In Anderson's case, it was angled outward and aft. A possible reason for the difference is the fact that Anderson used a different motion profile for this case. While pure sinusoids for pitch and roll are used in our case, she employed a double peak square wave motion profile for pitch.

5.5 Summary

Four test cases to study the flow signature over both low and high thrust regimes were conducted over two planes of view; one at 0.8 span location and the other at mid-span. The phased-averaged velocity and vorticity plots at six different foil positions, presented here, showed that vortex shedding patterns over the three-dimensional flapping foil was strongly influenced by the flow parameters and geometry.

At low Strouhal numbers and α_{max}, only shear layer vortices dominate (as seen in Cases 1 and 2). The wake pattern is typically characterized a trail of shear layer vortices, forming a weakly mixed Karman street along the foil path, with some LE separation. The wake momentum shows little evidence of thrust production, which corresponds with the low C_T values obtain from experimental measurements of Case 1 and 2. Since little work is done in increasing the kinetic energy of the flow, the efficiencies recorded are naturally high. The effect of increasing angle of attack leads to a more pronounced LE separation.

At higher Strouhal numbers, vortices are seen being shed into the wake either singly or in pairs. The LE vortex either merges with the TE vortex and convects downstream as a single vortex or in some cases, mixed pairs of opposite sign exist to produce strong thrust. The vortical signature is predominantly composed of the 2S pattern, the reverse Karman street. Although the lower portion of the foil falls in Region D based on its equivalent two-dimensional flow parameters, there is little evidence of the 2P mode of shedding. By virtue of the slow geometrical changes in foil dimensions and material continuity, it is less likely for the vortex formation along the span to have two distinct shedding patterns. Instead, the mixed vortex pair observed at 0.8S could be due to the tip vortex rolling upwards and interacting with the TE vortex. The experimental field data is insufficient to conclude the origin of the mixed pair. More time series data for DPIV would be needed to show the evolution of such vortical patterns more clearly. Nevertheless, the velocity plot from this mixed pair shows strong vectors being produced at an oblique angle to the flow direction. From basic momentum analysis, the existence of this velocity jet in the wake gives rise to thrust (which corresponds with the high C_T values obtained from experimental measurements).

The plots do seem to suggest highly three-dimensional effects at the lower quarter of the foil, with vortex structures possibly evolving orthogonally to the plane of view. A detailed investigation of this tip region is recommended to fully understand the wake structure beyond 0.7S.

Chapter 6

Conclusions

In this thesis, a series of investigative work has been drawn together, ranging from literature survey to design and experimentation, to develop a better understanding for three-dimensional flapping foils and its potential application to water-borne vehicle propulsion. The measurement of the performance of a three-dimensional flapping foil in terms of thrust generation and hydrodynamic efficiency was set as a primary objective of this study. A second-generation foil actuator, equipped with position sensors and a six-axes force sensor was first implemented for use in the MHL water-tunnel facility. Propulsion tests were then completed to measure the mean planform area thrust coefficient and efficiency over a range of frequencies, roll and pitch amplitudes. Next, using DPIV, the vortical signature behind the flapping foil was also recorded and studied to analyse its dependency on foil kinematics. The collective effort and insight gained in this and previous related studies have generated a better understanding of how the vortex shedding patterns are related to the foil kinematics and also thrust generation.

6.1 Force Measurements

Propulsion tests were accomplished for three roll amplitudes, $h_{0.7}/c$ = 1.0, 1.5 and 2.0. The parametric space included Strouhal numbers from 0.2 to 0.6 (at 0.1 increments) and α_{max} values from 15^0 to 45^0 (at 5^0 increments). This parametric space was bounded by the foil kinematics and mechanical limitations of the actuator. Further PID tuning would have to be made if higher oscillation frequencies are required.

Mean thrust, lift and efficiency were evaluated using the data recorded by the MC1 six-axes sensor. Post-processing involved the application of force offsets rotation matrices and averaging the data over 10-15 cycles. The propulsion test results showed a dependency of thrust and efficiency with St, $h_{0.7}/c$, and α_{max} values, similar to that obtained by Read, as well as McLetchie, for the two- and three-dimensional cases respectively. The results show that for a given Strouhal number, there exist a critical α_{max} value beyond which any increase in the angle of attack would not be beneficial to thrust production. Likewise, comparing the peak thrust coefficient obtained at $h_{0.7}/c$ of 1.0, 1.5 and 2.0 shows that an optimal heave to chord ratio can be found for maximal thrust.

The maximum planform area thrust coefficient measured from the experiments was 2.09 was recorded at $h_{0.7}/c$ = 1.5, St = 0.6 and $\alpha_{max} = 30^0$. Hydrodynamic efficiency ranged from 0.14 to 0.8. At $h_{0.7}/c$ of 2.0, a peak efficiency of 0.8 was found to occur at Strouhal number = 0.5. It must be noted that the high thrust coefficients found in some cases are artificially high since planform area was used to normalize the forces. A more useful normalization would be to use the swept area, which in this case, is function of both the roll and pitch amplitudes, and the distance between the foil and the roll axis of rotation.

The contour plots reveal a useful performance trend where at low α_{max}, high thrust and efficiency can be gained at sufficiently high Strouhal numbers. In particular, at higher roll amplitudes, the large oscillations produce large thrust with relatively less power loss. The higher the flapping frequency, the better the energy recovery, leading to better efficiency values being recorded.

6.2 Sensor Accuracy and Repeatability

The accuracy of the MC1 six-axes sensor was verified by comparing its force measurements with those from the tunnel dynamometer. In particular, the X-force load cell output from the dynamometer was compared directly with the thrust computed from the resolved force data of the MC1 sensor. Within the calibrated range of the dynamometer, the force measurements were found to be within 0.8 to 4.7% of the dynamometer output. In-house calibration of the sensitivity matrix also verified the reliability of the factory calibration data. The latter was then applied for all force measurements.

The percentage errors associated with the measurements remain significant at the low thrust regimes. To this end, four sets of five repeated runs were recorded to assess repeatability and

determine the standard deviations. The error range computed from the repeat runs show a sensor precision of about ± 0.044 N on average. Repeatability was next assessed by overlaying the repeat runs over each other and reviewing the quality of the traces. Overall, the drag force oscillated below the zero mean, thereby producing a net thrust. At the same time, its frequency was found to be twice that of the lift as expected, since thrust is produced on both the positive and negative stroke of the roll oscillation. A plot of the lift force time trace and its reflection revealed some asymmetry which can be to the distortions in the pitch and roll motions. While most of the peaks overlap well, there was an additional peak from the negative plot. This meant that more negative force lift was generated during the downstroke, resulting in a small net lift in the negative direction.

Overall, the test runs display good repeatability. The error margins obtained show that the six-axes sensor is able to provide reasonable resolution at the force range measured (0 ~10N). It is noted that the measurement range was up to 10% of the sensor's capacity. To drive percentage errors down, it would be advantageous to operate at higher force ranges. This would mean utilizing higher flow velocities and scaling the flapping frequencies higher to obtain the same flow parameters.

6.3 Flow Visualization Results

To gain an insight to vortex shedding patterns of the flapping foil and its dependency on foil parameters, its wake was captured using DPIV in accompanying experiments. Four test cases, at two planes of view, to study the flow signature over both low and high thrust regimes were conducted. The effect of Strouhal number and roll amplitudes led to varying vortical signatures ranging from weakly mixed Karman streets to thrust-producing 2S and mixed vortex shedding patterns. The effect of increasing the angle of attack is less dramatic, with LE separation becoming more pronounced.

The mixed vortex pair is observed for the case where efficiency and thrust measurements were relatively high. This mixed vortex or 2P pattern is however, significantly different from that observed by Anderson [4] for the two-dimensional flapping foil. In particular, the jet formation observed in the velocity vector plot for the three-dimensional case is angled inwards and aft while in Anderson's case, it was angled outward and aft. It is interesting to note that where the mixed pairing occurred, the case yielded high thrust and efficiency values. The reproduction of such a vortical structure by flapping might be key to optimal propulsor designs.

It was not possible to determine if the vortex pair was indeed composed of both LE and TE vortices (2P pattern) or a pairing up of the tip vortex with the TE vortex. Regardless, the plots showed high three-dimensionality and a more detailed investigation of this region is suggested to fully understand the vortical structure near the tip. By taking more cuts at different span locations, the effect of foil taper and geometry on the vortical signature along the span of the foil can be studied.

6.4 Recommendations for Future Work

With the new flapping foil actuator being configured for the MHL water tunnel, the hydrodynamic performance of different foil shapes can now be explored easily. Further work optimizing the shape, and material flexibility of the foil would be of great benefit towards finding the most effective flapping foil for waterborne vehicles. The fact that the wake pattern was strongly influenced by the geometry of the foil shows that foil geometry could be optimized for better performance.

The wake visualization experiments conducted in this study were not exhaustive and hence only provided a limited picture of the complete vortical signature of the three-dimensional flapping foil. For a more definite construct of the complex wake structure, further DPIV experiments are necessary at different span locations. The tip region is of particular interest in understanding the origination of the mixed vortex. DPIV measurements at an alternative viewing plane (XZ plane) would provide better insight to any three-dimensionality in the vortex structure. Determining the evolution of the mixed pair would be key to comprehending how the vortex structure yields high thrust with reasonable efficiencies. With respects to this, time series data for PIV i.e. a higher data rate (higher frames/sec) or more points along the foil trajectory should be conducted to gain better temporal resolution. These measurement will allow the evolution of vortical patterns to be seen more clearly.

Quantitavely, the vortex strength of the various wake patterns should be ascertained and compared against the measured thrust and efficiency. This would give us a measure of the power loss by the flapping foil through vortex generation. Combining this with a study of motion profiles could reveal an optimal motion profile for vorticity control, and propulsive strategies for maneuvering and propulsion.

Bibliography

[1] Adrian, R.J., 1991, "Particle-imaging techniques for experimental fluid mechanics", *Ann. Rev. Fluid Mech.*, 23, 261-302.

[2] Anderson J. M., 1996, "Vorticity control for efficient propulsion", *PhD thesis*, MIT/Woods Hole Oceanographic Institution.

[3] Anderson, J.M., Streitlien, K., Barrett, D.S., & Triantafyllou, M., 1998, "Oscillating foils of high efficiency", *J. Fluid Mech.*, 360, 41-72.

[4] Flores M.D., 2003, "Flapping motion of a three-dimensional foil for propulsion and maneuvering of underwater vehicles", *Masters thesis*, MIT/Ocean Engineering.

[5] Freymuth P., 1988, "Propulsive vortical signature of plunging and pitching airfoils", *AIAA J.*, 26, 881-883.

[6] Freymuth, P., 1989, "Visualizing the connectivity of vortex systems for pitching wings", *J. of Fluids Engineering*, 111, 217-220.

[7] Haugsdal, O., 2000, "Motion control of oscillating foils for steady propulsion and starting maneuvers", *Masters project*, NTNU/Marine Technology.

[8] Jones, K.D, & Platzer, M.F., 1997, "Numerical computation of flapping wing propulsion and power extraction", AIAA paper no. 97-0826.

[9] Jones, K.D, & Platzer, M.F., 1999, "An experimental and numerical investigation of flapping wing propulsion", AIAA paper no. 99-0995.

[10] Kerwin, J.E, 2001, "Hydrofoils and propellers", 13.04 lecture notes, 3.3, 147.

[11] Koochesfahani M., 1989, "Vortical patterns in the wake of an oscillating foil", *AIAA J.*, 27, 1200-1205.

[12] Lu, X.Y., Yang, J.M., Yin, X.Z., 2003, "Propulsive performance and vortex shedding of a foil in flapping flight", *Acta Mechanic*, 165, 189-206.

[13] Martin, C.B., 2001, "Design and performance evaluation of a biomimetic flapping foil", *Masters Thesis*, MIT/Ocean Engineering.

[14] McCroskey W.J., 1982, "Unsteady airfoils", *Ann. Rev. Fluid Mech.*, 14, 285-311.

[15] McLetchie, K., 2004, "Forces and hydrodynamic efficiency measurements of a three dimensional flapping foil", *Masters Thesis*, MIT/Ocean Engineering.

[16] Michael, J.C.S., Wilkin, P., & Williams, M.H., 1996, "The advantages of an unsteady panel method in modelling the aerodynamic forces on rigid flapping wings", *J. Exp. Biol.*, 199, 1073-1083.

[17] Ohmi, K., Coutanceau, O.D., & Loc, T.P., 1991, "Further experiments on vortex formation around an oscillating and translating airfoil at large incidences", *J. Fluid Mech.*, 225, 607-630.

[18] Oshima, Y., & Oshima, K., 1980, "Vortical flow behind an oscillating foil", *Proceedings of the 15th International Union of Theoretical and Applied Mech*, 357-368.

[19] Panda, J., & Zaman, K.B.M.Q., 1994, "Experimental investigation of the flow field of an oscillating airfoil and estimation of lift from wake surveys", *J. Fluid Mech.*, 265, 65-95.

[20] Polidoro, V., 2003, "Flapping foil propulsion for cruising and hovering autonomous underwater vehicles", *Masters Thesis*, MIT/Ocean Engineering.

[21] Ramamurthi, R., & Sandberg, W., 2001, "Simulation of flow about flapping airfoils using finite element incompressible flow solver", *AIAA J.*, 39, 253-260.

[22] Read D., 2000, "Oscillating foils for propulsion and maneuvering of ships and underwater vehicles", *Masters thesis*, MIT/Ocean Engineering.

[23] Read D.A., Hover F.S., & Triantafyllou M.S., 2003, "Forces on oscillating foils for propulsion and maneuvering", *J. Fluids and Struct.*, 17, 163-183.

[24] Techet, A.H., 1998, "Vortical patterns behind a tapered cylinder", Masters Thesis, MIT/Ocean Engineering & Woods Hole Oceanographic Institution.

[25] Triantafyllou G.S., Triantafyllou M.S., & Grosenbaugh R., 1993, "Optimal thrust development in oscillating foils with application to fish propulsion', *J. Fluids and Struct.*, 7, 205–224.

[26] Vandenberghe, N., Zhang, J., & Childress, S., 2004, "Symmetry breaking leads to forward flapping flight", *J. Fluid Mech.*, 506, 147-155.

[27] von Ellenrieder K.D., Kostas J., & Soria J., 2003, "Flow structures behind a heaving and pitching finite-span wing", *J. Fluid Mech.*, 490, 129-138.

[28] Willert, C.E., & Gharib, M., 1991, "Digital particle image velocimetry", *Exp. Fluids*, 10, 181-193.

[29] Williamson, C.H.K., & Roshko, A., 1988, "Vortex formation in the wake of an oscillating cylinder", *J. Fluids and Struct.*, 4, 355-381.